UNIVERSITAT POLITÈCNICA DE VALÈNCIA

Escuela Técnica Superior de Ingeniería del Diseño

Bachelor's Thesis for the Degree of Aerospace Engineering

FINITE-ELEMENT MODELING AND ANALYTICAL STUDY OF 2D QUANTUM CONFINEMENT EFFECT ON THE THERMOELECTRIC PROPERTIES

Author

Nataliya Sevryugina

Supervisor

José Luis Pérez Aparicio

Co-Supervisor

Pablo Moreno Navarro

Universitat Politècnica de València

Escuela Técnica Superior de Ingeniería del Diseño

Valencia - December of 2021

Finite-element modeling and analytical study of 2D quantum confinement effect on the thermoelectric properties

Nataliya Sevryugina

Universitat Politècnica de València
Escuela Técnica Superior de Ingeniería del Diseño

December of 2021

Abstract

In this work, physical properties of thermoelectric materials are investigated. For the performance enhancement of these materials, state-of-the-art techniques are reviewed.

An accurate estimation of the properties of thin films is important for the correct material selection for further applications. Methods such as Direct and Alternate Current applied to the Hall bars and Van der Pauw geometries are investigated for measurements of electrical conductivity and Hall coefficient. These methods were simulated with the finite element method software $FEAP$. The analysis of the most common errors and the influence of the magnetic field on thermoelectric properties are provided. Finally, an experiment from recent research technique for Seebeck and Hall coefficients estimation was repeated with $FEAP$ simulation. It is important to mention that prior to the study of the material characterization, validation of the galvanomagnetic effect is carried out by comparing the analytical and the $FEAP$ results.

Throughout the work the graphical post-processing and figures are done with $GNUPlot$ and *Adobe Illustrator*®. All the calculations are done with $Mathematica$® and $Matlab$®.

Contents

List of Figures

List of Tables

List of Symbols

Upper case letters

A	—	Area [m^2].
A_c	—	Cross-section area [m^2].
A_s	—	Surface area [m^2].
B	—	Magnetic field [T].
C	—	Constant number [-].
E_h	—	Hall's electric field [V/m].
$\dot{E}$	—	Rate of energy change [W/s].
$\dot{E}_g$	—	Rate of generated energy [W/s].
$\dot{E}_{in}$	—	Rate of added energy [W/s].
$\dot{E}_{out}$	—	Rate of removed energy [W/s].
I	—	Electric current [A].
K	—	Constant number [-].
L	—	Length [m].
M	—	Righi-Leduc coefficient [m^2 /V ·s].
N	—	Nernst coefficient [m^2 /K ·s].
P	—	Perimeter [m].
Q	—	Heat flux [W].
Q_g	—	Generated heat flux [W].
R	—	Hall coefficient [m^3 /A ·s].
T	—	Temperature [K].
$\dot{T}$	—	Transient temperature [K/s].
ΔT	—	Temperature difference [K].
V	—	Voltage [V].
V_e	—	Ettinghausen voltage [V].
V_{hl}	—	Hall voltage [V].
V_m	—	Misalignment voltage [V].
V_{ME}	—	Measured voltage with a single reading [V].
V_n	—	Nernst voltage [V].
V_r	—	Righi-Leduc voltage [V].
V_s	—	Thermoelectric voltage [V].
ΔV	—	Voltage difference [V].
ZT	—	Figure of merit [-].

Lower case letters

c_p	—	Heat capacity [J/kg·K].
d	—	Mass density [kg / m^3].
e	—	Carrier charge [C].
f	—	Bessel function [-].
f_a	—	Geometry dependent factor for Van der Pauw method [-].
f_d	—	Geometry dependent factor for Direct Current method [-].
f_h	—	Hall force [kg·m / s^2].
$f_{_L}$	—	Lorentz force [kg·m / s^2].
f_m	—	Magnetic force [kg·m / s^2].
h	—	Convective heat transfer coefficient [W/m^2· K].
h_p	—	Plank constant [J·m].
i	—	Imaginary number [-].
j	—	Electric flux [A/m^2].
k_b	—	Boltzmann constant [J/K].
l	—	Side length [m].
m	—	Contacts misalignment [m].
m_i	—	Effective mass of the charge carrier [kg].
n	—	Charge career concentration [1/m^3].
n_i	—	Order of the Bessel function [-].
r	—	Radius [m].
q	—	Conductive heat flux [W/m^2].
q_c	—	Convective heat flux [W/m^2].
s	—	Height [m].
t	—	Thickness [m].
t_s	—	Thickness of the substrate [m].
v	—	Velocity [m/s].
v_g	—	Phonon group velocity [m/s].
w	—	Width [m].
w_t	—	Twiddle factor of the discrete Fourier transform [-].
x, y, z	—	Spacial axes directions [-].

Greek letters

α	—	Seebeck coefficient [V/K].
β	—	Inductance [H].
Γ	—	Lorenz number [W·Ω/K^2].
γ	—	Electrical conductivity [1/ Ω·m].
κ	—	Thermal conductivity [W/m·K].
κ_e	—	Electron thermal conductivity [W/m·K].
κ_l	—	Lattice thermal conductivity [W/m·K].
ξ	—	Non-dimensional length [-].
μ	—	Career mobility [m^2/V·s].
ρ	—	Electrical resistivity [Ω·m].
τ	—	Time [s].
τ_p	—	Phonon relaxation time [s].
ω	—	Angular velocity [rad/s].

Superscript letters

$+$	—	Positive direction.
$-$	—	Negative directions.

Subscript letters

r	—	Radius.
s	—	Surface.
x, y, z	—	Spacial axes directions.
JS	—	Joule-Seebeck.

Vectors and tensors

$\boldsymbol{j}$	—	Electric flux vector [A/m^2].
$\boldsymbol{q}$	—	Thermal flux vector [W/m^2].
$\boldsymbol{\alpha}$	—	Seebeck coefficient tensor [V/K].
$\boldsymbol{\rho}$	—	Electrical resistivity tensor [Ω·m].
$\boldsymbol{\gamma}$	—	Electrical conductivity tensor [1/Ω·m].
$\boldsymbol{\kappa}$	—	Thermal conductivity tensor [W/m·K].

Mathematical symbols

∇	—	Gradient of a scalar-balued differentiable function [-].
$\nabla\cdot$	—	Divergence [-].
∂	—	Partial derivative [-].
d	—	Total derivative [-].
I	—	Modified Bessel function of the first kind [-].
K	—	Modified Bessel function of the second kind [-].

Acronyms

AC	—	Alternate Current.
ASN	—	Autonomous low-power wireless Sensor Nodes.
ASTM	—	American Society for Testing and Materials.
BC	—	Boundary Condition.
D	—	Dimension.
DC	—	Direct Current.
DOS	—	Density Of States.

FDM	—	Finite Difference Method.
FEM	—	Finite Element Method.
GM	—	Galvanomagnetic.
MBE	—	Molecular Beam Epitaxy.
MMRTG	—	Multi-Mission Radioisotope Thermoelectric Generator.
MEMS	—	Micro-Electro-Mechanical Systems.
NASA	—	National Aeronautics and Space Administration.
ODE	—	Ordinary Differential Equation.
PDE	—	Partial Differential Equation.
PGEC	—	Phonon Glass Electron Crystal.
PLD	—	Pulsed Laser Deposition.
RTG	—	Radioisotope Thermoelectric Generator.
SHM	—	Structural Health Monitoring.
SNAP	—	System for Nuclear Auxiliary Power.
TE	—	Thermoelectric.
TEG	—	Thermoelectric Generator.
U.S.	—	Unites States.
VdP	—	Van der Pauw.
WSN	—	Wireless Sensor Network.

1

Introduction

1.1 Introduction

1.1.1 Motivation

Since the beginning of Second Industrial Revolution, the number of manufacturing industries, the amount of transportation, etc. have increased and as a consequence, the consumption of non-renewable energy has exploded. The power generation stations required to fulfill most of the demand are the cause of long-term toxin's emissions and environmental deterioration.

In view of the foregoing, renewable energy production seems to be a solution to curb the uncontrolled expenditure of natural resources and ecosystem destruction. However, forms of electricity generation from solar, wind or hydropower sources are not completely feasible because of some adverse effects such as noise or energy losses.

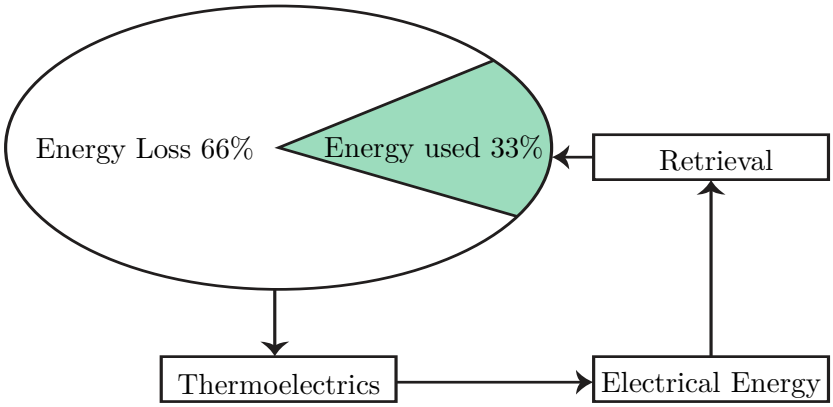

Figure 1.1: The method to recapture waste energy [7].

Therefore, an alternative approach to curb the destruction of nature is directed to research methods of improving the overall energy utilization rate and efficiency. It has been estimated that only 33% of the primary energy is used effectively and 66% is wasted in form of exhaust or residual heat (Figure 1.1). Therefore, an innovative technology of recovering waste heat and transforming it into electricity using the thermoelectric (TE) phenomenon was proposed. Until now, this is one of the most promising ways of saving energy and achieving environmental

protection. For instance, it has been demonstrated that the implementation of TE Generators (TEGs) in the automotive sector could reduce fuel consumption by 10% through recovering the combustion energy released into the atmosphere as gas exhaust [8].

The TE effect has raised a high scientific interest as an alternative low–energy source. The advantage of using TE devices is that electricity can be obtained directly from a heat gradient, without any intermediate processes. Despite their low performance, these power systems are maintenance-free and offer long service life, high stability and reliability. The latter makes TEGs an interesting electric supply for systems located in remote areas with difficult access for maintenance. For that reason, TE technology is extensively used in navigation beacons, weather stations, offshore platforms, or pipelines.

Deep outer space is also considered an extreme environment, where conventional power supply is not feasible and the TE phenomenon is applied. The particular class of Radioisotope Thermoelectric Generators (RTGs) especially developed for applications in the aerospace sector; RTGs are the source of power supply for spacecrafts during interstellar missions to Moon and outer Solar System planets and are extensively implemented in NASA's projects. The most recent one is in the Perseverance rover sent to Mars and equipped with a modern Multi-Mission Radioisotope Thermoelectric Generator (MMRTG, Figure 1.2a).

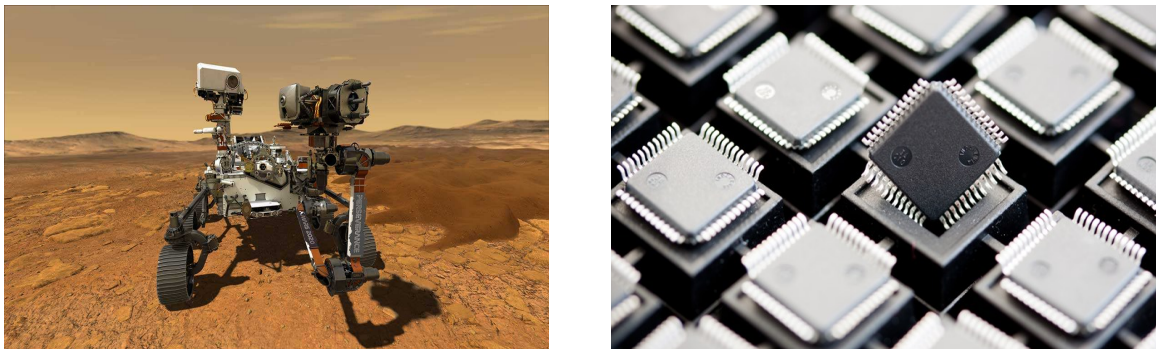

(a) (b)

Figure 1.2: Applications of the TE phenomenon: (a) NASA's Mars 2020 Perseverance rover [49]; (b) MEMS [48].

As previously mentioned, TE systems are limited by a low-efficiency rate. In the past twenty years, many investigations have been focused on improving this parameter. Until now, two different methods have been studied: crystal structure materials and nanomaterials. The latter has attracted great attention as more than 10% of efficiency can be gained from changes in the material dimension combined with the possibility of integration into nano or microdevices.

Nowadays, nanomaterials are highly demanded in the area of micro-harvesting and micro-cooling. The first technique is key for making sensors completely wireless or manufacturing power autonomous Micro-Electro-Mechanical Systems (MEMS, Figure 1.2b). The second technique is essential for medical laboratory equipment or electronic devices.

To sum up, the TE studies can make significant contributions to technological development. As stated before, TE materials have been applied for cooling, heating or power generation in many fields such as medicine, transport, the automotive and aviation industry, aerospace and electronics. The ability of these materials to work in tandem with other technologies and their application into reversible energy conversion, allows this technology to be one of the most promising at the moment.

1.2 The historical background of thermoelectricity

Thermoelectricity is the phenomenon of direct conversion of a heat gradient into electricity for solid or liquid semiconductors. This physical effect is based on three interrelated ones: the Seebeck TE effect and, the Peltier plus the Thomson electrothermal effects.

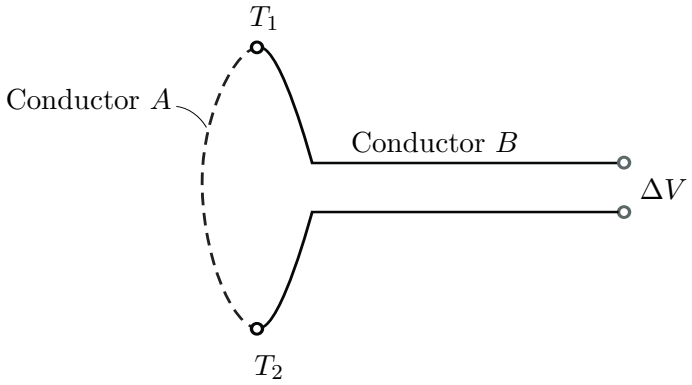

Figure 1.3: The measurement of ΔV.

In 1821, T. Seebeck observed the existence of a voltage difference ΔV in an open circuit, when two thermocouples (joints of dissimilar conductors A, B) were maintained at different temperatures T_1, T_2 as seen in Figure 1.3. T. Seebeck initially believed that this was a purely magnetic effect, but later it became clear that the appearance of the electric flux was caused by the T gradient. Some years later, in the course of experimental studies of the conductivity of Sb and Bi, J. Peltier noticed T changes in a thermocouple, with a prescribed electric flux. In the case of a closed circuit with two thermocouples, heat is absorbed at one end of the thermocouple

and released at the other (Figure 1.4).

It is apparent that the Peltier effect is the opposite of the Seebeck effect. J. Peltier also made additional research on the influence of a flux direction applied through the thermocouple. He defended that the direction is the decisive parameter that determines if heating or the contrary cooling effect can be obtained.

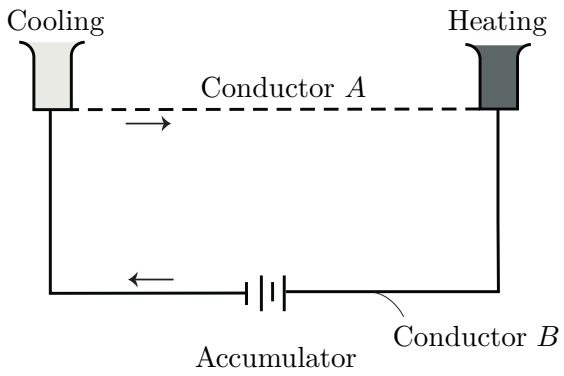

Figure 1.4: The Peltier's effect of cooling and heating.

The next breakthrough was achieved by W. Thomson, who studied TE effects in an uniform conductor. As illustrated in Figure 1.5, in the metal with dissimilar T at its extremes heat is generated (positive Thomson effect) when the flux is directed from the heated to the cooled extremes. For the opposite flux direction, heat is absorbed (negative Thomson effect).

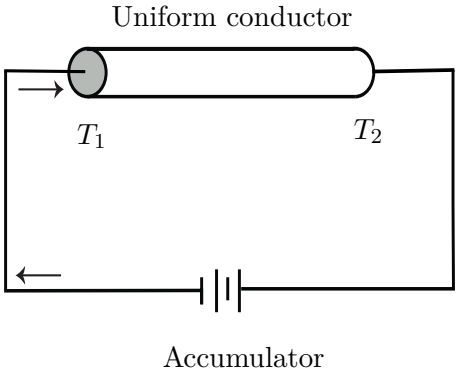

Figure 1.5: A scheme of the Thomson's experiment.

From the physical statements described above, emerged three TE parameters: the Seebeck,

the Peltier and the Thomson coefficients useful for TE materials characterization.

1.3 TE applications

The TE generation modules have become extensively demanded due to high reliability, resistance to mechanical loads and to vibrations. The scope of TE applications is extremely diverse and are discussed in the following subsections.

1.3.1 TE Generators (TEGs)

As stated before, TEGs are the simplest TE devices that convert a T gradient into a useful power source. A TEG basic element (Figure 1.6) is a thermocouple, made up of p-type and n-type semiconductors interconnected through a Cu conductor. In n-type semiconductors, charge carriers are electrons, whereas in p-type charge carriers are holes. When extremes of the thermocouple are exposed to different temperatures, charge carriers diffuse from the hot side and accrue at the opposite. This disposition of charge carriers creates ΔV along the semiconductor.

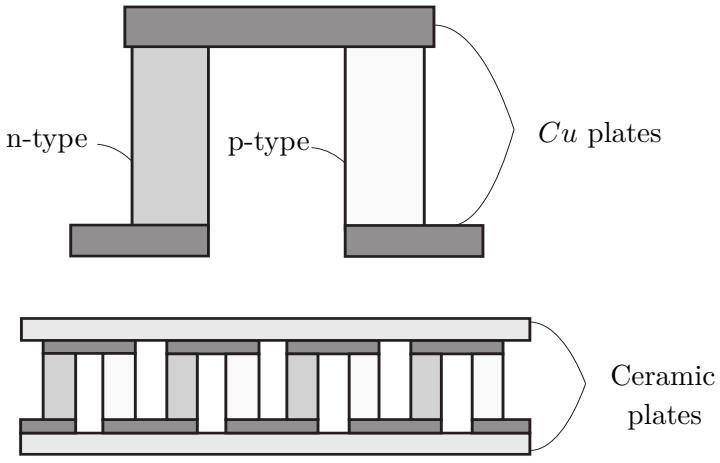

Figure 1.6: A scheme of the TE module.

To construct TEG's, thermocouples are connected electrically in series and thermally in parallel. These thermocouples are placed between two ceramic plates, that provide an appropriate structural rigidity and a flat surface for application in more complex devices. The structure described in this subsection can be used for the Seebeck and the Peltier effects.

1.3.2 Radioisotope TE Generators (RTGs)

The space explorations take place at large distances beyond the Earth's atmosphere and require safe and long-term power generation. In deep space, a conventional power supply with burning fuels is impractical due to the heaviness of the fuel amount the probe needs to carry.

In that context, nuclear power systems such as RTGs have been popular since 1960 and are a source of heat and onboard power supply for spacecraft and scientific instruments. The working principle of these generators is to convert through thermocouples heat generated from the natural decay of a radioisotope fuel *Pu-238* into electricity; the selection of materials for thermocouples depends on mission requirements. The first RTG used for space missions was SNAP-3 (System for Nuclear Auxiliary Power), a 3 [W] generator mounted in the navigational satellite (*U.S. Navy Transit 4A*) launched in 1961 (Figure 1.7), [3].

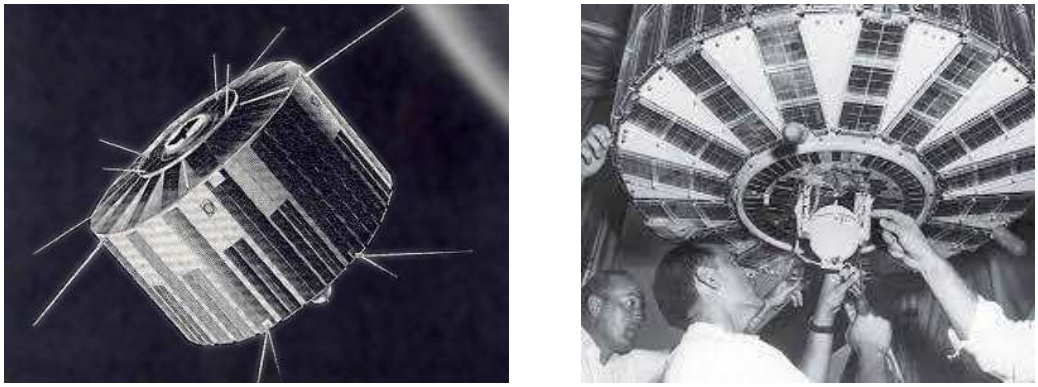

(a) (b)

Figure 1.7: The first space mission with the RTG power supply: (a) *Navy's Transit 4A* navigational satellite [47]; (b) Installation of the SNAP-3B to the Navy's navigational satellite [50].

Some years later, RTGs were used on Earth, Moon, and other solar system spacecrafts and were capable to provide the total electrical power supply. World-known missions such as the *Pioneer, Voyager, Galileo, Ulysses* and *Cassini* also utilized RTGs. The last three, consisted of 572 thermocouples wired in an electric circuit, capable to generate a total of 300 [W] with the initial fuel loading [3], [9].

In view of the foregoing, RTGs are highly demanded in space explorations due to:

- **Durability:** capable to operate at extreme environmental conditions such as high radiation or extreme temperatures making their application appropriate for deep space missions.

- **Autonomy:** no special requirements to start working. Once the radioisotope fuel source is loaded into a converter, electricity generation starts.

1.3.3 Aircraft-specific TE Generator modules

Commercial aircrafts are typically equipped with a large number of sensors for data processing, measuring, and communication tasks. Today, the development of sensors with an autonomous power supply, named Wireless Sensor Networks (WSN), allows to reduce weight, cabling effort and maintenance costs, which normally represent the third-highest airline expense [2], [10].

Energy supply with batteries was unsuccessful due to critical drawbacks such as replacement and risk of ignition at high temperatures. Another alternative was the implementation of solar cells, however, they were rapidly damaged due to structural vibrations during the journey. In that context, TEGs were an attainable solution for the WSN energy supply.

In aircrafts, there are two main methods to obtain a T gradient required for TEGs functioning: from passenger's cabin inside/outside T difference, or from exterior T variations with altitude during take-off and landing. The second method supposed a huge technical effort through the TEG installation and it was considered more suitable to take advantage of the first [6]. With TEGs implementation, sensors such as those of Structural Health Monitoring (SHM) and Autonomous low-power wireless Sensor Nodes (ASN) became fully self-powered.

The application of TEGs is not only restricted to the aeronautical sector. Automotive manufacturing companies also have been investigating their implementation in models such as *BMW X6, Ford Fusion* and *Chevy Suburban*. This application can provide a nominal 5% improvement in fuel economy as waste heat is converted into electricity [4].

1.4 Recent progress in TE materials

TE materials can be characterized by a quantity named figure of merit ZT, which defines the conversion efficiency of the material. For enhancing ZT, three strongly correlated parameters such as Seebeck coefficient α, electrical conductivity γ and thermal conductivity κ need to be taken into account. The latter is subdivided into lattice thermal conductivity κ_l and electron thermal conductivity κ_e:

$$ZT = \frac{\alpha^2 \gamma\, T}{\kappa}\ ; \qquad \kappa = \kappa_l + \kappa_e \tag{1.1}$$

where $\alpha^2\gamma$ is the power factor and T the temperature of working.

Through the last 20 years, the TE properties α, γ, κ of metals, semiconductors and insulators have been investigated. Efficient TE materials should have a high $\alpha^2\gamma$ combined with a low κ. It has been demonstrated that semiconductors are the most suitable for TE applications due to their relatively low κ and optimal value of $\alpha^2\gamma$ in comparison with metals and insulators as seen in the graphics:

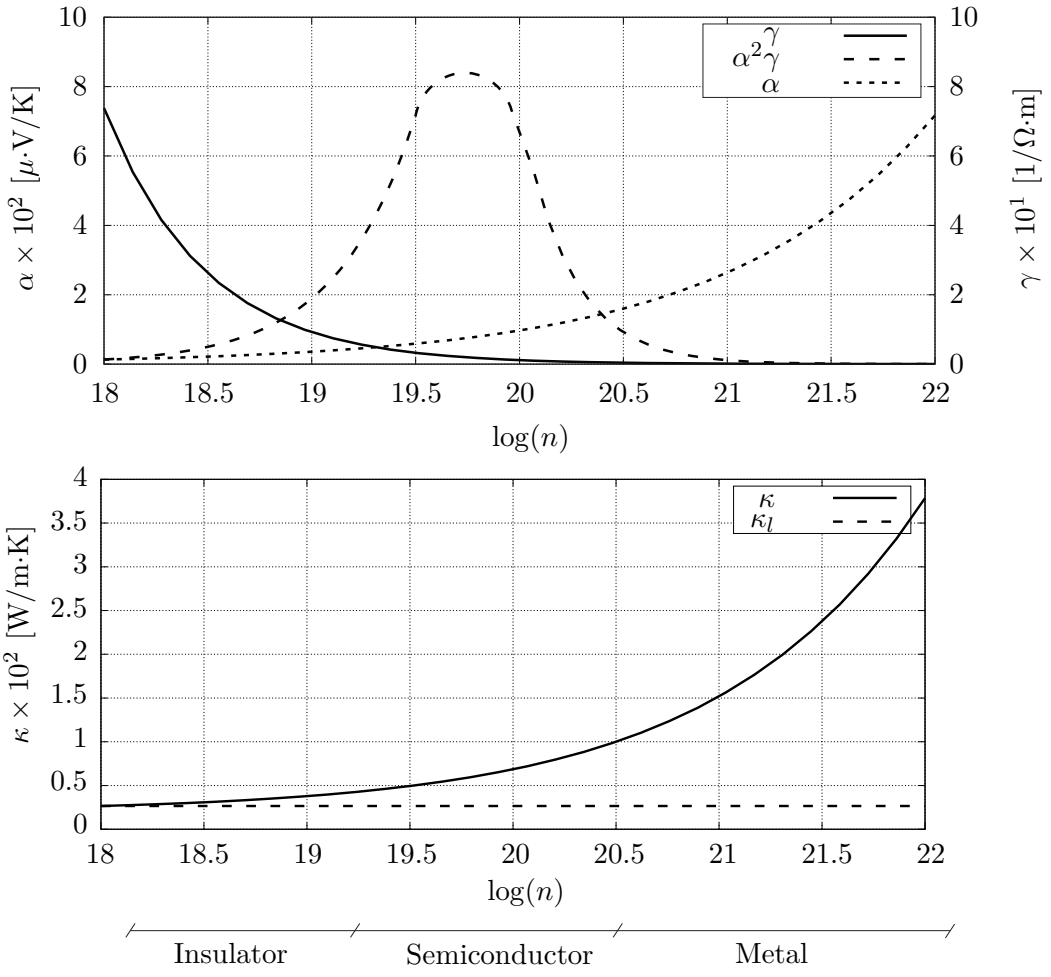

Figure 1.8: Relationship between TE properties and free charge carrier concentration for different materials [12].

Several mathematical models have been developed for a better understanding of the TE parameters performance. According to the Wiedman-Franz Law, $\alpha^2\gamma$ and κ_e are correlated by the charge carrier concentration n. Consequently, changing n to obtain high $\alpha^2\gamma$ and low κ_e is

not possible as κ_e, γ, n are linearly dependent. In that way, κ_l is the unique parameter that can contribute to enhance ZT since it is independent of n:

$$\begin{aligned} \alpha &= \frac{8\pi^2\gamma\, k_b^2}{3e\, h_p^2}\, m_i\, T \left(\frac{\pi}{3n}\right)^{2/3} \; ; & \gamma &= n\, e\, \mu \; ; \\ \kappa_e &= \Gamma\, T\, \gamma \; ; & \kappa_l &= \frac{1}{3} c_p\, v_g^2\, \tau_p \end{aligned} \tag{1.2}$$

where Γ is the Lorenz number, c_p the heat capacity, e the carrier charge, h_p the Plank constant, k_b the Boltzmann constant, m_i the effective mass of the charge carrier, v_g the phonon group velocity, μ the charge carrier mobility and τ_p the phonon relaxation time.

The first TE materials presented $ZT \approx 1$ and efficiencies of about 5%. Recent investigations reported maximum improvements of $ZT = 2.6$, [13]. However, no material has yet achieved $ZT \geq 3$ required to make TE commercial devices competitive with conventional systems. Until now, two approaches to improve ZT are used:

- **TE materials with renewed crystal structure:** also named Phonon Glass Electron Crystal (PGEC), was introduced by Slack in 1995 and consisted in creating TE with glass behavior regarding their thermal properties and crystal behavior regarding their electrical properties. The purpose of this method is to reduce κ_l significantly; it is used in skutterudites, zintl phases and clathrates with $1 \leq ZT \leq 2$, [13].
- **Nanostructured TE materials:** size effect in TE materials and the later approach of nanostructuring has efficiently enhanced TE properties and both are reviewed in Subsection 1.4.2 and 1.4.1.

1.4.1 Bulk nanostructured TE materials (Nanocomposites)

Nanocomposites are bulk TE materials embedded with nanoparticles. These materials play an important role in commercial applications as they can be synthesized in large quantities and are compatible with electronic devices [13]. The idea of nanostructured TE materials is focused on the reduction of κ_l. According to Boltzmann law Eq. (1.2), a reduced κ_l can be achieved with a short τ_p, a slow v_g and a low c_p. The last parameter is difficult to decrease since at the high T at which TE materials work, c_p is defined by the Dulong-Petit limit. Therefore v_g and τ_p reduction techniques play an important role in TE structure design. In this subsection, the method of the τ_p diminution is detailed as is commonly used in nanocomposites [15].

Lattice vibration is the oscillation experienced by atoms in solid materials about the equilibrium position. This vibrational energy is quantized by particles named phonons, the propagation of which originates κ_l and contributes to the heat transport phenomenon in TE besides the charge carriers.

This vibrations also can be classified in harmonic and anharmonic. In harmonic lattice vibrations, the restoring force (force to bring the particle to equilibrium) is a linear function of atomic displacement from its equilibrium position. In this configuration, the phonon's movement does not cause any energy exchange. However, even in perfect crystals, the lattice vibrations are anharmonic, characteristic that results in intrinsic scattering of phonons. This phenomenon causes a τ_p reduction and therefore lowers κ_l. Moreover, any imperfection or defect strengthens the lattice anharmonicity and intensifies the scattering rate of phonons creating an additional thermal resistance (shortened τ_p and low κ_l). For that purpose nanocomposites are designed with point defects, dislocations and interfaces.

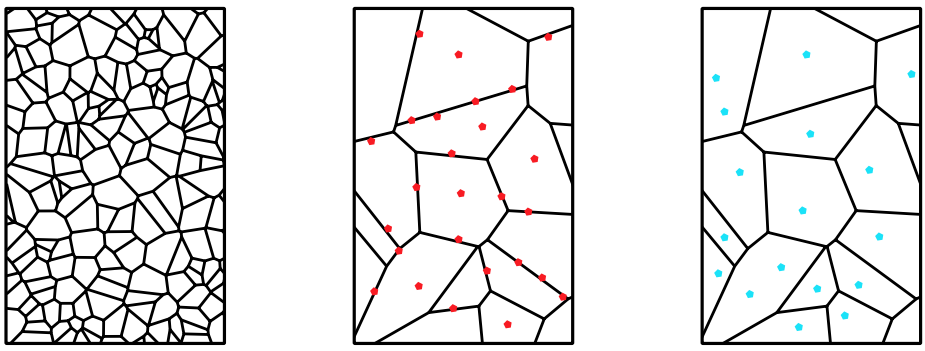

(a) (b) (c)

Figure 1.9: Illustration of structure design of nanocomposites: (a) nanograined composite; (b) nanoinclusion composite with an incoherent interface; (c) nanoinclusion composite with a coherent interface.

- **Point defects:** substitutions, interstitials and vacancies, are imperfections that intensify the scattering of high-frequency phonons with short wavelengths.
- **Dislocations:** maximize the scattering of mid-frequency phonons, and can be introduced into the material through clustering of vacancies and interstitials in single phased material or through coherent/incoherent second-phase precipitations that originate boundary dislocations. The coherent dislocations (Figure 1.9(c)) leads to good lattice matching with bulk material while incoherent ones (Figure 1.9(b)) define a boundary between matrix and precipitation.

- **Interfaces:** can be created by reducing the grain size or through precipitations (Figure 1.9(a)). As a consequence this interfaces lead to the scattering of low-frequency phonons.

1.4.2 Low dimensional TE materials

Great ZT improvements were reported in 1993 with the first models of low dimensional TE materials. The quantum confinement allowed to vary γ, α, κ independently, leading to the possibility of reaching $ZT = 2$, [14]. The origin of improved TE properties comes from enhanced electronic Density of States (DOS), the term that refers to the number of quantized energy levels that electrons can occupy. The magnitude DOS can be expressed in mass terms as m_i; a high m_i implies high α, Eq. (1.2). The quantum confinement also contributes to v_g reduction and increase of phonon interface scattering; both effects result in reduced κ_l.

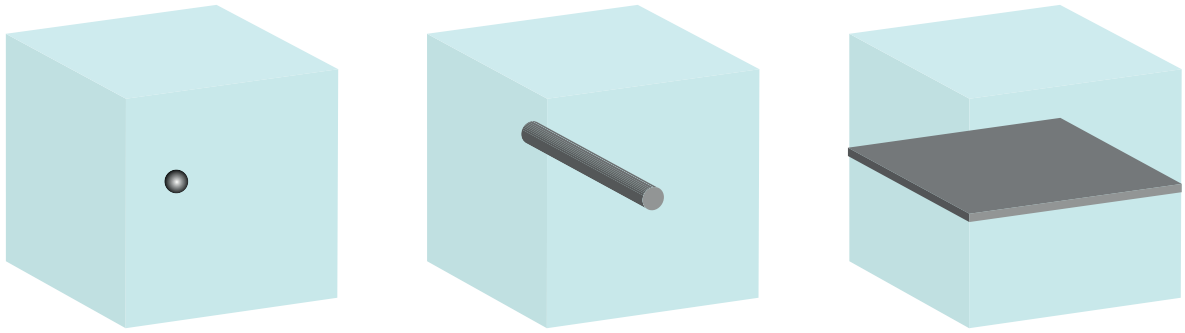

(a) (b) (c)

Figure 1.10: Dimensional comparison of bulk TE (light blue) to quantum confinement structures (grey): (a) Quantum dot; (b) Quantum wire; (c) Quantum well.

This method has been experimentally applied to quantum dots (0D structures, Figure 1.10(a)), quantum wires (1D structures, Figure 1.10(b)) and quantum wells (2D structures, Figure 1.10(c)).

- **Quantum wires**

The high surface to volume ratio of 1D quantum wires results in reduced κ_l accompanied by strong quantum confinement, both effects destined to large ZT improvement. However, in experimental works, wires demonstrate a ZT lower than predicted theoretically, reaching only $ZT = 0.25$. A reason for this drastic reduction is under investigation and probably it is caused by impurities [11].

- **Quantum well superlattices**

Superlattices are periodic structures of two or more quantum wells (thin-film layers) with confined 2D electrons movement. In this kind of structure, α can increase three orders of magnitude while κ_l is reduced in the perpendicular direction due to phonon scattering. For fabrication of the thin film, techniques such as Pulsed Laser Deposition (PLD) and Molecular Beam Epitaxy (MBE) were developed.

Nowadays, Bi_2Te_3 and Sb_2Te_3 superlattices can reach $ZT = 2.4$ [13]. Although with high ZT, these structures do not have any practical application for large-area devices due to the difficult fabrication process and lack of scientific investigations on stability.

1.5 Thesis organization

This academic work is subdivided into the following chapters:

- **Chapter 2: Validation of simulation results**
  Stationary convection, thermoelectric and galvanomagnetic cases were analytically solved and compared with the $FEAP$ results. The purpose of this section is to validate the user's elements that are later used for experiments' simulations.

- **Chapter 3: Measurement techniques of the Hall effect in the thin-film semiconductors**
  Measurements are performed applying Direct (DC) and Alternate (AC) current techniques on two types of geometries: Hall bar and Van der Pauw shapes. The influence of spin Hall effect and erroneous voltage contribution due to contacts misalignment are discussed. Finally, two parametric studies are developed. The first one is focused on the magnitude of the magnetic field from which thermoelectric properties become both magnetic and temperature functions. The second one studies the influence of film's thickness on measurement results.

- **Chapter 4: Lithography-free resistance thermometry**
  Recent research technique for Seebeck and Hall coefficients estimation is simulated with $FEAP$. The laboratory results are compared with those of $FEAP$.

- **Chapter 5: Conclusions**
  Concludes all the previous results, provides future directions and a total budget for this work.

2

Validation of simulation results

The Finite Element Method (FEM) is a numerical technique developed to solve Partial Differential Equations (PDEs) by imposing Boundary Conditions (BCs). As most physical phenomena are defined with PDEs, it is considered appropriate to model heat conduction, TE or galvanomagnetic (GM) problems with FEM.

Among many FEM softwares, the $FEAP$ code developed by Robert L. Taylor at the University of California (Berkeley) was chosen. $FEAP$ contains a general element library for modeling 1D, 2D or 3D meshes to solve linear heat conduction, linear/non-linear structural and solid mechanics problems. One of the benefits of the program is that offers the possibility to create new elements that incorporate the formulation defined by the user [16]. In this chapter, two elements previously developed are used:

(**i**) $elmt11.f$: a 3D solid element with coupled thermal and electrical conduction formulation.

(**ii**) $elmt12.f$: a 2D GM thin film layer coupled with an optional convection condition.

The main goal of the present chapter is to validate the $elmt11.f$ and the $elmt12.f$ by comparing $FEAP$ modeling results with analytical solutions for stationary and transient problems. Results will be displayed on 2D graphics and $FEAP$ meshes. Once the accuracy of these elements has been validated, more complex simulations of cases without analytical solution can be carried out.

2.1 Stationary validation of *elmt11.f* and *elmt12.f*

First, cases of heat conduction/convection are simulated for stationary problems. Once these cases are validated, the subsequent simulations will be focused on the TE and the GM processes. The simulations will be run with three different TE material.

For convection and Joule-Seebeck cases, the cuprous delafossite $CuAlO_2$ is used, the TE properties of which are assumed as constant with T. The subsequent Seebeck effect is run for TE material with properties variable with T; for this simulation the delafossite transition oxide, in particular $Cu_{0.99}Pt_{0.01}FeO_2$ is chosen. This material was selected as its TE properties can be approximated with linear functions of T with low error. Finally, GM simulations will be run

for indium antimonide $InSb$ material.

2.1.1 Formulation of conduction/convection heat transfer in extended surfaces

In this subsection, various fin geometries with a variable cross-sectional area and different BCs are simulated. For a better understanding of the T–evolution along fins, a general formulation of heat transfer is introduced.

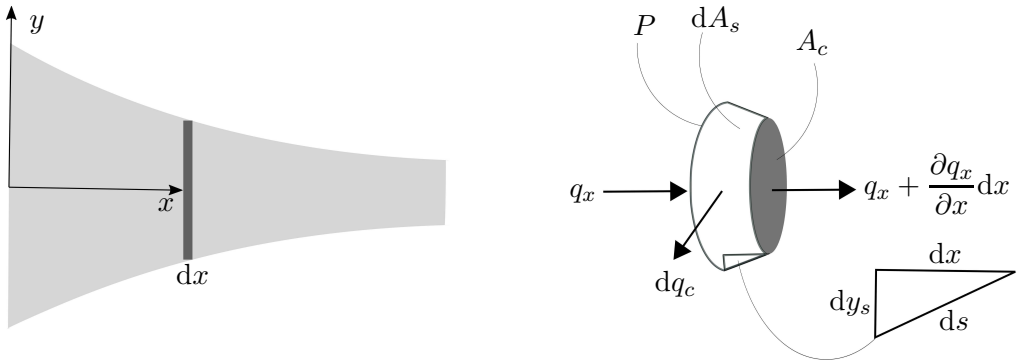

Figure 2.1: Representation of conduction q_x and convection $\mathrm{d}q_c$ for selected $\mathrm{d}x$ slice of the fin.

The base of the fin is maintained at constant T_L, while its lateral surface is exposed to a fluid with known heat transfer coefficient h. T is removed along this surface due to convection and conducted through the fin in axial direction (Figure 2.1).

Since the T–gradient in the y–direction can be considered negligible, it is assumed as a function of x–direction. This simplification transforms a 2D heat transfer problem into 1D and makes it possible to obtain an analytical solution for fins with non–regular cross-sections area.

To obtain the T–distribution, it is necessary to formulate the principle of energy conservation:

$$\dot{E}_{in} \; + \; \dot{E}_g \; - \; \dot{E}_{out} = \dot{E} \tag{2.1}$$

where $\dot{E}_{in}$ is the rate of energy added to $\mathrm{d}x$, $\dot{E}_g$ the rate of energy generation per unit volume of $\mathrm{d}x$, $\dot{E}_{out}$ the rate of energy removed and $\dot{E}$ the rate of energy change within $\mathrm{d}x$.

It is assumed that the energy entering $\mathrm{d}x$ by conduction, leaves by both convection and conduc-

tion. All the terms of the Eq. (2.1) can be expanded as:

$$\begin{aligned} &\dot{E}_{in} = q_x \; ; && \dot{E}_g = Q_g \, A_c \, \mathrm{d}x \; ; && \dot{E}_{out} = q_x \, + \, \frac{\partial q_x}{\partial x} \, + \, \mathrm{d}q_c \; ; \\ &\dot{E} = d \, c_p A_c \, \dot{T} \, \mathrm{d}x \; ; && q_x = -\kappa \, A_c \, \frac{\partial T}{\partial x} \; ; && q_c = h \, (T - T_\infty) \; \mathrm{d}A_s \end{aligned} \tag{2.2}$$

where q_x is the conductive heat flux, q_c the convective heat flux, Q_g the generated heat flux, $T = T(x)$ the variable temperature, T_∞ the temperature and h the heat transfer coefficient (both of the convective fluid), $\mathrm{d}A_s$ the surface area of the fin where heat is exchanged by convection and $A_c = A_c \, (x)$ the cross-section area through which heat is conducted.

Substituting Eqs. (2.2) into Eq. (2.1), a general equation that describes the T–variation along the fin is obtained:

$$\frac{\partial^2 T}{\partial x^2} \, + \, \frac{1}{A_c} \frac{\mathrm{d}A_c}{\mathrm{d}x} \frac{\partial T}{\partial x} \, - \, \frac{h}{\kappa \, A_c} \frac{\mathrm{d}A_s}{\mathrm{d}x} \, (T - T_\infty) \, + \, \frac{Q_g}{\kappa} \, = \, \frac{d \, c_p}{\kappa} \, \dot{T} \tag{2.3}$$

From the previous expression can be concluded that the T–distribution is mostly determined by the fin geometry. In case of stationary problems without heat generation, the Eq. (2.3) can be simplified to:

$$\frac{\partial^2 T}{\partial x^2} \, + \, \frac{1}{A_c} \frac{\mathrm{d}A_c}{\mathrm{d}x} \frac{\partial T}{\partial x} \, - \, \frac{h}{\kappa \, A_c} \frac{\mathrm{d}A_s}{\mathrm{d}x} \, (T - T_\infty) \, = \, 0 \tag{2.4}$$

The $\mathrm{d}A_s$ can be defined as:

$$\left. \begin{array}{l} \mathrm{d}A_s = P \, \mathrm{d}s \\ \\ \mathrm{d}s = \sqrt{\mathrm{d}x^2 + \mathrm{d}{y_s}^2} \end{array} \right\} \quad \rightarrow \quad \frac{\mathrm{d}A_s}{\mathrm{d}x} = P \left[1 + \left(\frac{\mathrm{d}y_s}{\mathrm{d}x} \right)^2 \right]^{1/2} \tag{2.5}$$

where $P \equiv P(x)$ is the circumference perimeter in contact with fluid, represented in the Figure 2.1.

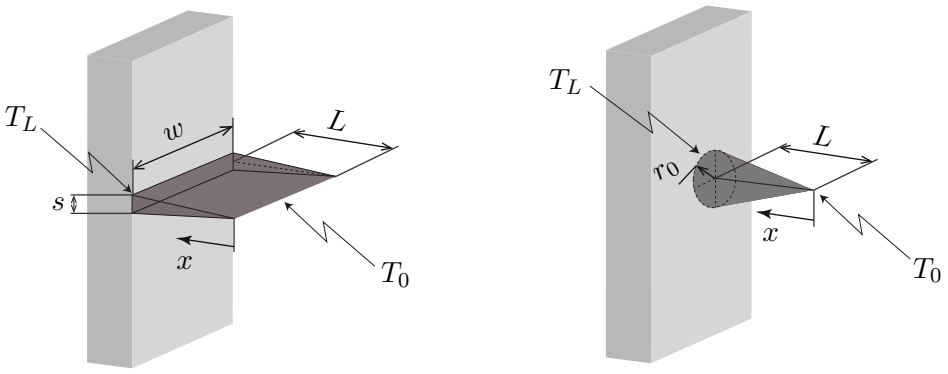

Figure 2.2: Representation of triangular and conical fins with dimensions and boundary conditions.

To solve a differential equation of second derivative, two BCs are required. In general, the first condition is imposed at the base and the second at the end of the fin. Two BCs used in Subsection 2.1.2 for solving the Eq. (2.4) are:

(**i**) Specified T at the base:

$$T(x = 0) := T_0$$

(**ii**) Specified T at the tip:

$$T(x = L) := T_L$$

2.1.2 Steady-state conduction/convection in variable cross-section fins for uncoupled problems

The cases represented in the Figure 2.2 are simulated. Air is chosen as a convective fluid. The BCs taken into account are **(i)** and **(ii)** the values of which, besides the fins dimensions, are summarized in the Table 2.1.

Parameter	Value	Units
L	0.4	[m]
w	0.6	[m]
s	0.2	[m]
r_0	0.2	[m]

Parameter	Value	Units
T_0	300	[K]
T_L	600	[K]
T_∞	293	[K]
h	5	[W/K·m^2]

Table 2.1: Dimensions and boundary conditions for cases represented in the Figure 2.2.

As stated before for convection and Joule-Seebeck cases $CuAlO_2$ material is used, the values of κ_m particularized for 400 [K] is taken from Table 2.2:

Properties	$CuAlO_2$	**Units**
α_m	3.20×10^{-4}	[V/K]
γ_m	1.85	[1/Ω·m]
κ_m	2.64	[W/m·K]

Table 2.2: Physical properties of the cuprous delafossite $CuAlO_2$ material at temperature $T_m =$ 400 [K], [17].

- **Triangular fin**

For the fin with area of variable cross-section, the Eq. (2.4) cannot be simplified. The conductive and the convective areas are:

$$\begin{cases} A_c = w\, y_s(x)\ ; \qquad y_s(x) = \dfrac{x\, s}{2L} \qquad \rightarrow \qquad \dfrac{\mathrm{d}A_c}{\mathrm{d}x} = \dfrac{w\, s}{L} \\ \dfrac{\mathrm{d}A_s}{\mathrm{d}x} = 2w \left[1 + \left(\dfrac{\mathrm{d}y_s}{\mathrm{d}x}\right)^2\right]^{1/2} = 2w \left[1 + \left(\dfrac{s}{2L}\right)^2\right]^{1/2} \end{cases} \tag{2.6}$$

$$x^2\, \frac{\partial^2 T}{\partial x^2} \ + \ x\, \frac{\partial T}{\partial x} \ - \ x\, \frac{2\, h\, L}{\kappa_m\, s} \sqrt{1 + \left(\frac{s}{2\, L}\right)^2}\, (T - T_\infty) \ = \ 0 \tag{2.7}$$

The Eq. (2.7) is a linear, second order, Ordinary Differential Equation (ODE). Its solution can be obtained with Bessel functions, the general differential equation to solve the Eq. (2.7) is:

$$x^2 \frac{\mathrm{d}^2 f}{\mathrm{d}x^2} + \left[(1-2A)\, x - 2\, B\, x^2\right] \frac{\mathrm{d}f}{\mathrm{d}x} + \left[C^2\, D^2\, x^{2C} + B^2\, x^2 - B\,(1-2\,A)\, x + A^2 - C^2\, n_i^2\right] f \ = \ 0 \tag{2.8}$$

In order to identify terms between the two previous equations, $A = B = n_i = 0$ and D must be an imaginary number and $T \equiv f$. The solution of the Eq. (2.8) is from [19]:

$$f(x) = x^A\, e^{B\, x} \left[\, C_1 \mathrm{I}_{n_i}\, (p\, x^C) \ + \ C_2 \mathrm{K}_{n_i}\, (p\, x^C) \,\right]$$

where C_1 and C_2 are the constants of integration, $\mathrm{I}_{n_i}\, (p\, x^C)$ the modified Bessel function of order n_i of the first kind and $\mathrm{K}_{n_i}\, (p\, x^C)$ of the second kind; in addition $p = D/i$, where i is the imaginary number.

It can be demonstrated that for this case the previous expression results in:

$$T = T_\infty + C_1\,\mathrm{I}_0\left[\frac{2\sqrt{h}\left(4\,L^2+s^2\right)^{1/4}\sqrt{x}}{\sqrt{\kappa_m\,s}}\right] + 2\,C_2\,\mathrm{K}_0\left[\frac{2\sqrt{h}\left(4\,L^2+s^2\right)^{1/4}\sqrt{x}}{\sqrt{\kappa_m\,s}}\right] \tag{2.9}$$

where the expressions inside brackets represent the argument of the Bessel functions.

Applying the BCs, the solution of C_1 and C_2 can be obtained. Since $\mathrm{K}_0(x=0)=\infty$ at the tip of the fin we would obtain $T_0=\infty$, an impossible solution; then $C_2=0$ must be assumed, see [19]. The Eq. (2.9) solution for the T–distribution is obtained with *Mathematica*®:

$$T = T_\infty + \frac{(T_L - T_\infty)\,\mathrm{I}_0\left[\dfrac{2\sqrt{h}\left(4L^2+s^2\right)^{1/4}\sqrt{x}}{\sqrt{\kappa_m\,s}}\right]}{\mathrm{I}_0\left[\dfrac{2\sqrt{h\,L}\left(4L^2+s^2\right)^{1/4}}{\sqrt{\kappa_m\,s}}\right]} \tag{2.10}$$

The Eq. (2.10) and the *FEAP* simulation results are displayed graphically. The triangular fin is discretized into $8\times8\times8$ rectangular elements of $elmt11.f$, with a total of 729 nodes; in addition convection is introduced with four thin layers of $elmt12.f$ (one for each external side), discretized into 8×8 elements. As the $elmt11.f$ and the $elmt12.f$ are defined only for rectangular elements, the mesh of the triangular fin has a fictitious height of $s_0=10^{-4}$ [m] at the tip. The *FEAP* and the analytical results fit perfectly in most of the length but diverge about 3.5% at the tip due to the simplification $C_2=0$ assumed in the Eq. (2.10); this simplification eliminates the contribution of the modified Bessel function of the second kind K_0 from the T–distribution.

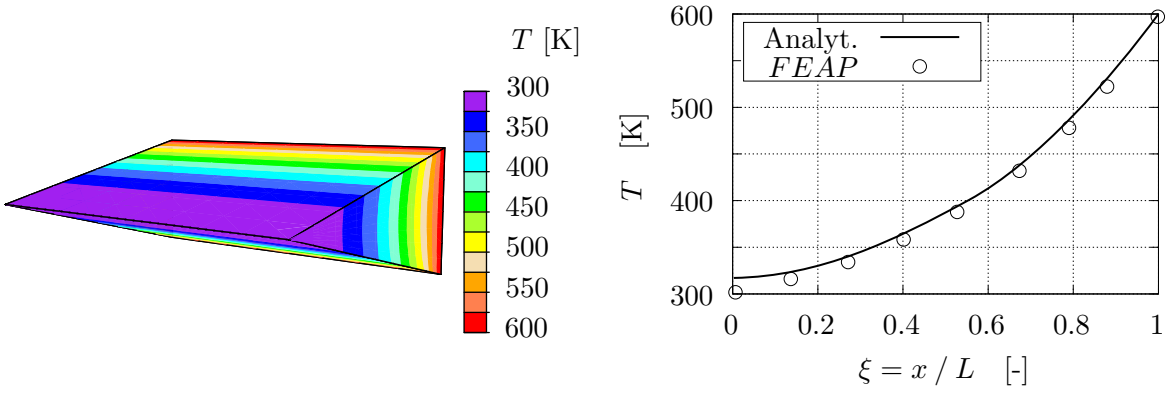

Figure 2.3: Analytical and numerical results of the T–distribution for the triangular fin with specified temperatures T at the base and at the tip. Results compared along $y=0$.

- **Conical fin**

In this case, circular conductive A_c and conical convective A_s areas are defined and substituted into the Eq. (2.4):

$$\begin{cases} A_c = \pi\, y_s(x)^2\ ; \qquad y_s(x) = \dfrac{r_0\, x}{L} \qquad \rightarrow \qquad \dfrac{\mathrm{d}A_c}{\mathrm{d}x} = 2\pi \left(\dfrac{r_0}{L}\right)^2 x \\ \dfrac{\mathrm{d}A_s}{\mathrm{d}x} = P\left[1+\left(\dfrac{\mathrm{d}y_s}{\mathrm{d}x}\right)^2\right]^{1/2} = 2\pi\,\dfrac{r_0}{L}\left[1+\left(\dfrac{r_0}{L}\right)^2\right]^{1/2} \end{cases} \tag{2.11}$$

$$\frac{\partial^2 T}{\partial x^2} \;+\; \frac{2}{x}\frac{\partial T}{\partial x} \;-\; \frac{h\,L}{\kappa_m\, r_0\, x}\left[1+\left(\frac{r_0}{L}\right)^2\right]^{1/2}(T-T_\infty) \;=\; 0 \tag{2.12}$$

The previous expression is approximated with a Bessel general differential equation as [19]:

$$x^2\,\frac{\partial^2 T}{\partial x^2} \;+\; 2\,x\,\frac{\partial T}{\partial x} \;-\; \eta^2\,x\,(T-T_\infty) \;=\; 0\ ; \qquad \eta^2 := \frac{h\,L}{\kappa_m\, r_0}\left[1+\left(\frac{r_0}{L}\right)^2\right]^{1/2} \tag{2.13}$$

Comparing Eq. (2.13) with Eq. (2.8), D must be taken imaginary and $n_i = 1$. Then, the solution for Eq. (2.13) is defined with modified Bessel functions of the first I_1 and the second kind K_1:

$$T = T_\infty + \frac{\mathrm{I}_1\left(2\,\eta\,\sqrt{x}\right)C_1}{\eta\,\sqrt{x}} \;+\; \frac{2\mathrm{K}_1\left(2\,\eta\sqrt{x}\right)C_2}{\eta\,\sqrt{x}} \tag{2.14}$$

The same simplification $C_2 = 0$ as for the triangular fin is applied, since $\mathrm{K}_1(x=0) = \infty$ and at the tip $T_0 = \infty$ is obtained [19]. After applying BCs, the solution of the Eq. (2.14) is again obtained with *Mathematica*®:

$$T = T_\infty - \frac{\sqrt{L}\,(T_\infty - T_L)\,\mathrm{I}_1\left(2\,\eta\,\sqrt{x}\right)}{\sqrt{x}\,\mathrm{I}_1\left(2\,\eta\,\sqrt{L}\right)} \tag{2.15}$$

Each 90° sector of the mesh is discretized into $8\times 8\times 8$ parallelepiped elements of *elmt*11.*f* and the external surfaces into 8×8 elements of convective thin layer of *elmt*12.*f*. The mesh contains a total of 1458 nodes. The Eq. (2.15) and the *FEAP* results fit at most of the length but diverge at the tip due to the removal of the modified Bessel function K_1 in the Eq. (2.14). The error introduced into the analytical solution near the tip is about of 16.7%, bigger than in the previous case; this larger error is due to the order of K: $\mathrm{K}_0(x) = \infty$ already at $x \lessapprox 0.05$, while $\mathrm{K}_1(x) = \infty$ at $x \lessapprox 0.15$. The x domain for ∞ in the first order is larger than that for the zero order of K and as a consequence, the divergence at the conical tip is more pronounced.

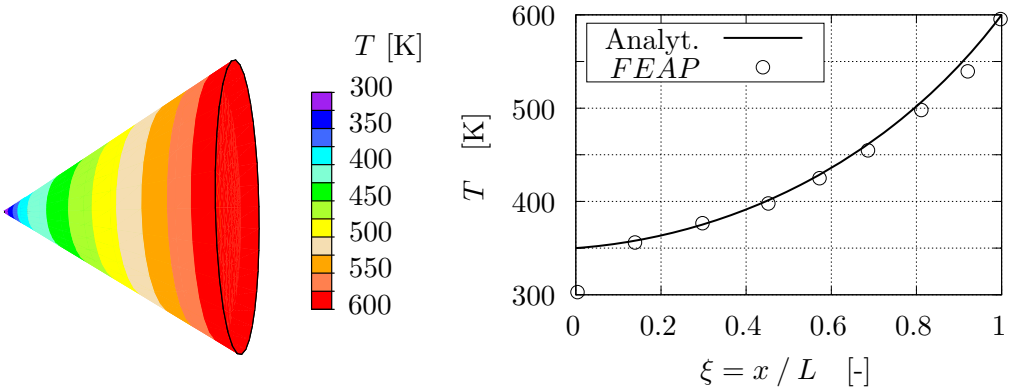

Figure 2.4: Analytical and numerical results of the T–distribution for the conical fin with specified temperatures T at the base and at the tip. Results compared along the cone height.

2.1.3 Steady-state conduction in variable cross-section for TE problems

In this subsection, simulations are performed for the fins represented in Figure 2.5. The dimensions of the triangular fin are the same as those of the Figure 2.2. A new geometry describing an annular fin is introduced, the dimensions of which, besides the prescribed BCs are summarized in Table 2.3. The first BC represented by T_L, V_L at the base is common for Joule-Seebeck and Seebeck effects. The second BC is T_0, V_0 for the Joule-Seebeck effect and only T_0 for the Seebeck effect. As mentioned before, simulations of Joule-Seebeck effect are run with constant TE properties, particularized for 400 [K] as in the Table 2.2. Once the validity of this mesh is checked, the Seebeck effect is studied with variable properties.

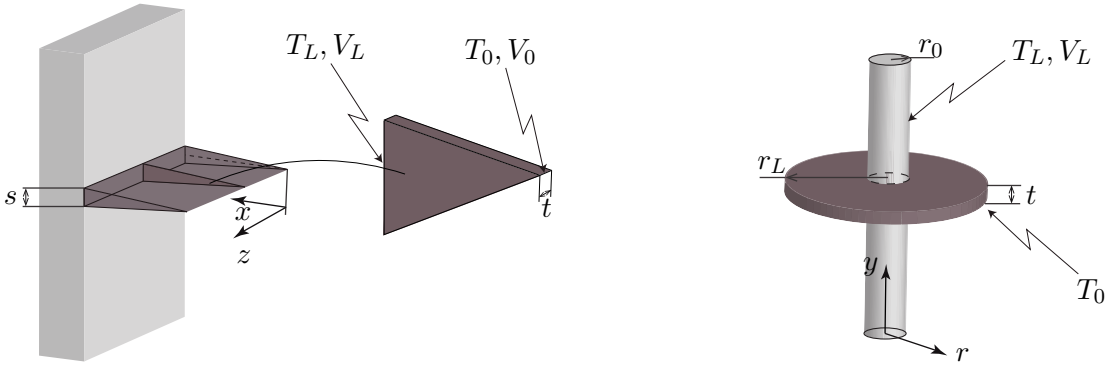

Figure 2.5: Representation of triangular and annular fins with dimensions and boundary conditions.

Since in the rest of this work only 2D TE parts will be studied, the fins of this subsection will also be 2D; the thickness of the TE layers will be very thin as seen in the Table 2.3. The current cases have electro-thermal coupling and therefore the governing equations have to be

reestablished.

Parameter	Value	Units
r_L	1	[m]
r_0	0.2	[m]
s	0.2	[m]
t	10^{-5}	[m]

Parameter	Value	Units
T_0	300	[K]
T_L	600	[K]
V_0	3	[V]
V_L	0	[V]

Table 2.3: Dimensions and boundary conditions for cases represented in the Figure 2.5.

2.1.4 Simulations of the Joule-Seebeck effect

To study the Joule-Seebeck effect, T and V gradients are applied along the x–direction. A general formulation for the Joule-Seebeck effect is:

$$\begin{cases} j_x = -\gamma_m \, A_c \, \dfrac{\mathrm{d}V}{\mathrm{d}x} \; - \; \alpha_m \, A_c \, \gamma_m \, \dfrac{\mathrm{d}T}{\mathrm{d}x} \\ q_x = -\kappa_m \, A_c \, \dfrac{\mathrm{d}T}{\mathrm{d}x} \; + \; \alpha_m \, A_c \, T \, j_x \\ \dfrac{\mathrm{d}j_x}{\mathrm{d}x} = 0 \\ -\dfrac{\mathrm{d}q_x}{\mathrm{d}x} \; - j_x \dfrac{\mathrm{d}V}{\mathrm{d}x} = 0 \end{cases} \tag{2.16}$$

where the first two are the balance equations and define electric j_x and heat q_x fluxes along the x–direction, and the last two are the equilibrium equations [18]. To be able to find an analytical solution, the variable area A_c is not included in the third equation.

The Eqs. (2.16) are non-linear and non-homogeneous ODEs. Due to the complexity of this type of equations, the V and T distributions are also solved using $Mathematica^{®}$. The command `DSolve` can find solutions for ODE, partial or algebraic differential equations. The program's algorithm firstly classifies type, order, degree and linearity of the differential equation introduced by the user. Later, the solution is obtained applying a programmed method for the classified equation or in case of complex systems, by reducing the equations to a simpler one [51].

- **Seebeck effect in triangular fin with low j_x**

Since the fluxes are going to be independent of the z–coordinate (Figure 2.5 left), the triangular fin is analyzed with the 2D element $elmt12.f$. To simplify the following equations we consider that the tip is not located at $x = 0$ but at a very small $x = L_0 = 0.001$ [m]. This

approximation is chosen as the results of T, V distributions will be functions of logarithms, and $\log(0)$ is undefined. In that way, the height s_0 at the tip is not completely null. Then, the variable area A_c is the thickness t multiplied by $s(x)$ along $L_0 < x < L$.

$$A_c = t\, s(x) = t\, \frac{s\, x}{L} \qquad \rightarrow \qquad \frac{\mathrm{d}A_c}{\mathrm{d}x} = t\, \frac{s}{L} \tag{2.17}$$

As mentioned before, the BCs are:

$$\begin{aligned} &V(x=0) := V_0\ ; && V(x=L) := V_L\ ; \\ &T(x=0) := T_0\ ; && T(x=L) := T_L \end{aligned} \tag{2.18}$$

First, to obtain the j_x and V distributions, the first and the third equations from Eqs. (2.16) are considered. Applying the four BCs and solving with $Mathematica^{®}$, the distributions of j_x and V are:

$$j_x = \frac{\gamma_m\, s\, [\, \alpha_m\, (T_0 - T_L)\, + V_0\, -\, V_L\,]}{L\, [\log(L)\, -\, \log(L_0)]}$$

$$\begin{aligned} V \quad &= \frac{(\alpha_m T_0\, +\, V_0)\, \log(L)\, -\, (\alpha_m T_L\, +\, V_L)\, \log(L_0)}{\log(L)\, -\, \log(L_0)}\, + \\ &\frac{[\, \alpha_m\, (T_L\, - T_0)\, + V_L\, -\, V_0\,]\, L\, \log(x)\, +\, \alpha_m\, [\, \log(L_0)\, -\, \log(L)\,]\, T}{\log(L)\, -\, \log(L_0)} \end{aligned} \tag{2.19}$$

Next, the second and the fourth equations from Eqs. (2.16) are solved. The solution is difficult to obtain and therefore some simplifications are considered. Taking into account that α_m is four orders of magnitude lower than κ_m, and j_x obtained in the Eqs. (2.19) is practically null, the term $\alpha_m\, A_c T\, j_x$ can be neglected from q_x equation. In order to verify this hypothesis, the orders of magnitude of $\kappa_m\, \mathrm{d}T/\mathrm{d}x$ and $\alpha_m\, T\, j_x$ are compared. The T and j_x values are taken from $FEAP$, while $\mathrm{d}T/\mathrm{d}x$ is obtained approximating T to the fifth order polynomial with the command $Matlab^{®}$ *polyfit* and analytically deriving T with respect to x. In the same way, $j_x\, \mathrm{d}V/\mathrm{d}x$ and $\kappa_m\, \mathrm{d}^2T/\mathrm{d}x^2$ are compared.

$\xi = x\ /\ L$	$\xi = 0$	$\xi = 0.25$	$\xi = 0.5$	$\xi = 0.75$	$\xi = 1$
$\alpha_m\, T\, j_x$	-0.057	-0.042	-0.025	-0.017	-0.003
$\kappa_m\, \mathrm{d}T/\mathrm{d}x$	9.59 $\times 10^3$	2.25 $\times 10^3$	826.3	996.4	692.81
$j_x\, \mathrm{d}V/\mathrm{d}x$	-0.087	-0.065	-0.041	-0.029	-0.0051
$\kappa_m\, \mathrm{d}^2T/\mathrm{d}x^2$	-1.14 $\times 10^5$	-0.38 $\times 10^5$	-0.14 $\times 10^5$	-0.14 $\times 10^5$	-0.37 $\times 10^5$

Table 2.4: Numerical comparison between Fourier, Peltier and Joule terms.

As verified, $\alpha_m\, T\, j_x$ and $j_x\, \mathrm{d}V/\mathrm{d}x$ can be neglected. In that way, the second and the fourth expression from the Eqs. (2.16) are simplified to:

$$q_x = -\kappa_m\, A_c\, \frac{\mathrm{d}T}{\mathrm{d}x} + \underbrace{\cancel{\alpha_m\, A_c\, T\, j_x}}_{Peltier}; \qquad \kappa_m \frac{\mathrm{d}^2T}{\mathrm{d}x^2} = \underbrace{j_x \frac{\cancel{\mathrm{d}V}}{\cancel{\mathrm{d}x}}}_{Joule} \tag{2.20}$$

It should be noted that Peltier and Joule effects can be neglected from the T–distribution if j_x is low enough but not from the V–distribution.

Applying the temperature BCs expressed in the Eqs. (2.18) to the previous expression, the final q_x and T–distribution are obtained with $Mathematica^{®}$:

$$q_x = \frac{\kappa_m\, s\, (T_0 - T_L)}{L[\log(L) - \log(L_0)]}\ ; \qquad T = \frac{T_0 \log(L)\ -\ T_L \log(L_0)\ +\ (T_L - T_0)\log(x)}{\log(L) - \log(L_0)} \tag{2.21}$$

For the final V–distribution, the previous T–solution is substituted into the last expression from Eqs. (2.19):

$$V = \frac{V_0 \log(L)\ -\ V_L \log(L_0)\ +\ (V_L - V_0)\log(x)}{\log(L) - \log(L_0)} \tag{2.22}$$

The triangular thin film is discretized into 8×8 rectangular elements of $elmt12.f$ with a total of 81 nodes. As quadrilateral elements must be used, an imaginary height $s_0 = 10^{-4}$ [m] coherent with the value of L_0 is again introduced at the tip. The analytical and the $FEAP$ solutions diverge only 10% at $0 < \xi < 0.5$. This little incoherence can be caused by both simplifications of the Joule and the Peltier effects. These simplifications can be only applied to the case of Seebeck effect with low j_x or if the dimensions of the mesh are large; both cases result in a very low j_x.

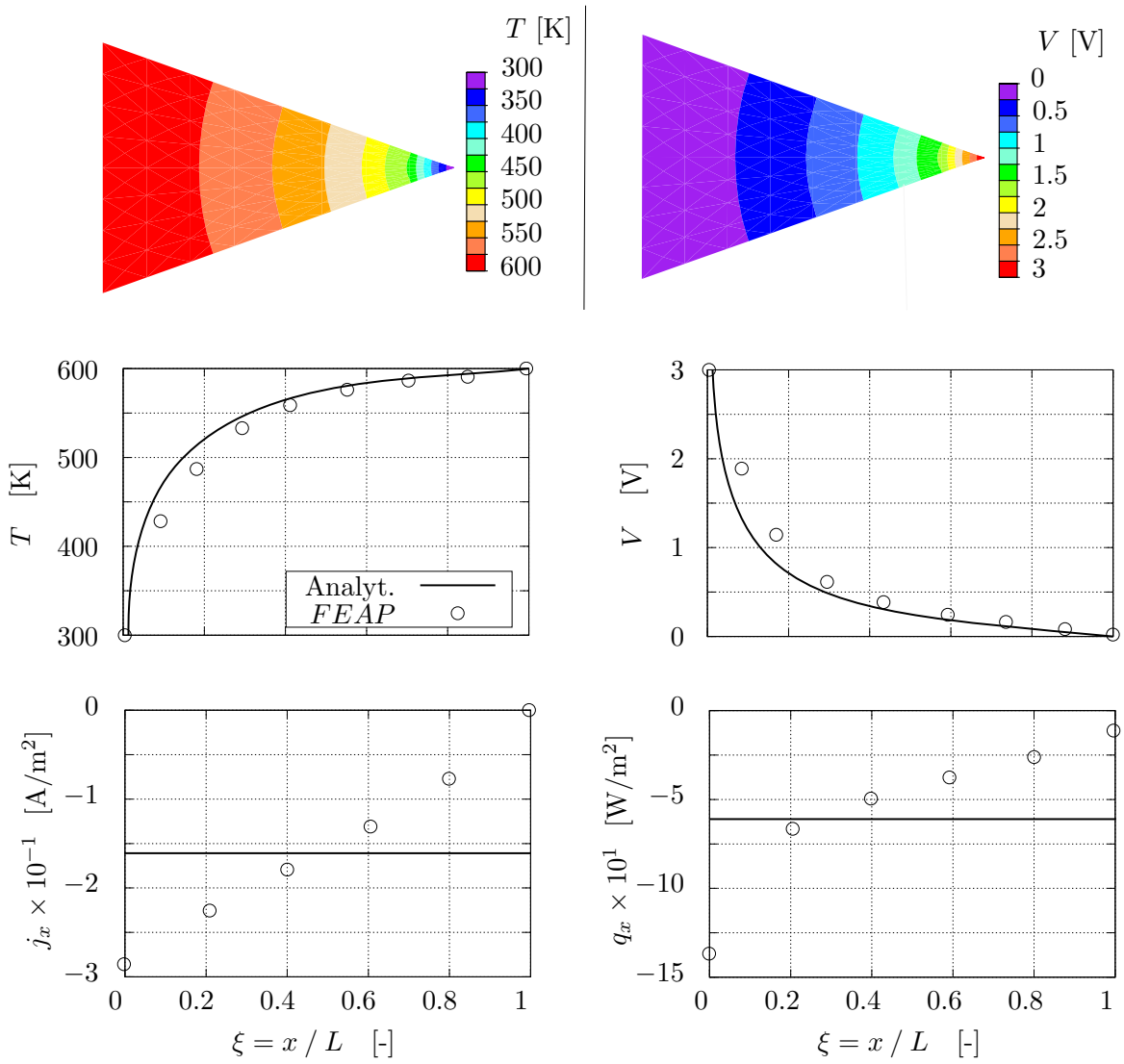

Figure 2.6: Analytical and numerical results of temperature and voltage distributions besides the electric and thermal fluxes for the triangular fin. Results compared along $y = 0$.

Analyzing j_x and q_x, it seems that analytical results give the arithmetic mean value of that of *FEAP*. These mean values is reasonable, as the conductive area was not considered in the equilibrium equations Eqs. (2.16) due to the complexity of solving the complete expressions.

- **Joule-Seebeck effect in triangular fin**

In order to observe Joule and Peltier effects in the T–distribution, the previous voltage BCs are increased by more than ten times:

$$V(x=0) := V_0 \; ; \qquad\qquad V(x=L) := 13.3 \times V_L \tag{2.23}$$

The same j_x and V–distribution (although with different values) as in the Eqs. (2.19) is obtained. The difference with the previous case appears when T and q_x are analyzed. First, q_x is obtained by integrating the fourth expression from the Eqs. (2.16):

$$q_x \quad = C_1 + \frac{\gamma_m \, s \, [\alpha_m(T_0 - T_L) + V_0 - V_L] \Big\{ [\alpha_m(T_0 - T_L) + V_0 - V_L] \log(x) + \alpha_m [\log(L) - \log(L_0)] T \Big\}}{L [\log(L) - \log(L_0)]^2} \tag{2.24}$$

The previous equation is substituted into the second one from the Eqs. (2.16); applying the two temperature BCs the two constants are solved and q_x and T–distribution are obtained. The T–solution is expressed with incomplete Gamma functions, that are integrals of the factorial extension to complex numbers with variable integration limits. Generalized hypergeometric series also appear, that are power series with successive coefficients. Due to the complexity of the T–solution the final formulae results for T and q_x are not provided, but the numerical results are displayed on graphics.

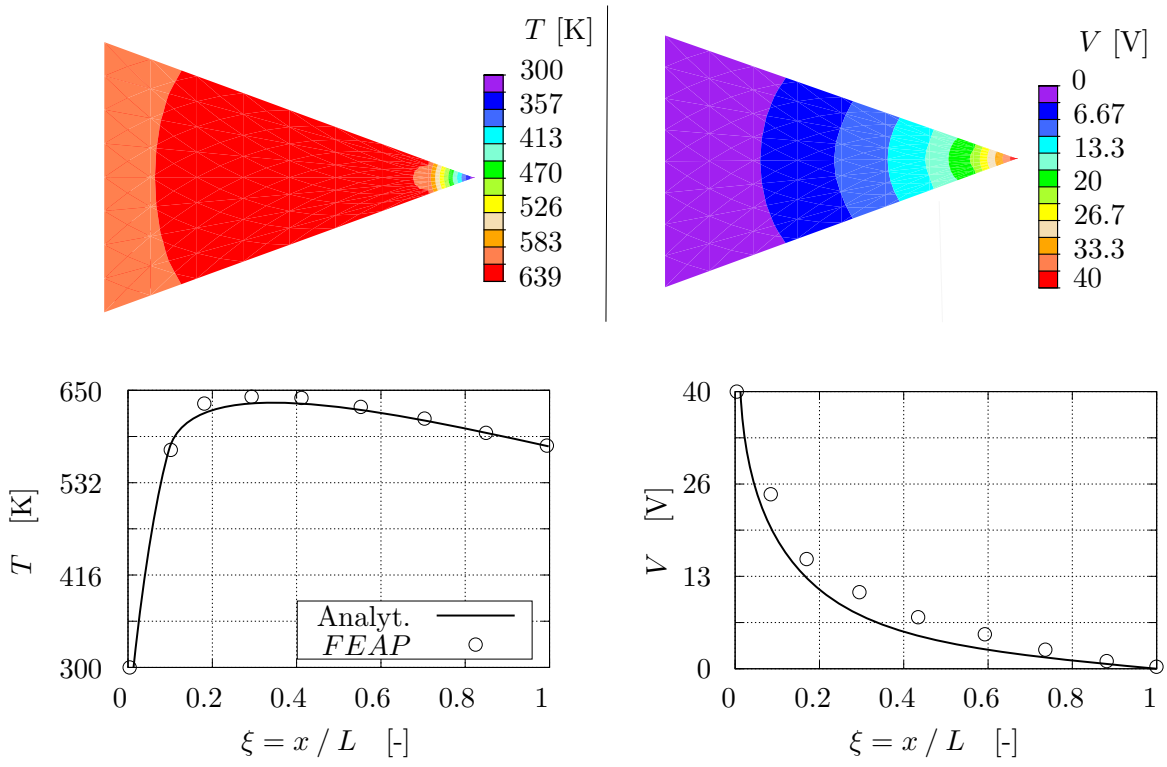

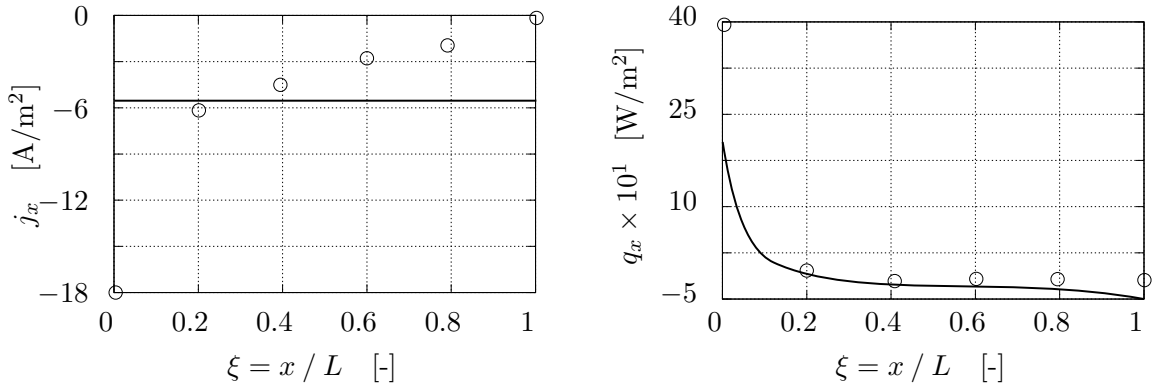

Figure 2.7: Analytical and numerical results of temperature and voltage distributions and electric and thermal fluxes for the triangular fin. Results compared along $y = 0$.

The *FEAP* mesh is equal to that of the previous case. It can be concluded that with new voltage BCs the Joule effect can be perfectly observed, although the closed-form is too cumbersome; the T–distribution is incremented 50 [K] above T_L. These *FEAP* and analytical results fit perfectly along all the length. In the same way, q_x results also fits almost perfectly, but at the tip a substantial difference is observed that can be caused by 2D interactions between T and V. The analytical j_x results are again the average of those of *FEAP* due to the fact that the conductive area in the third Eqs. (2.16) has been considered constant.

2.1.5 Simulation of the Seebeck effect with variable TE properties

Usually, the TE properties of any material are variable with T, in particular $\kappa(T)$, $\gamma(T)$, $\alpha(T)$. As mentioned at the beginning of Section 2, the properties of $Cu_{0.99}Pt_{0.01}FeO_2$ can be approximated with low error to linear T functions.

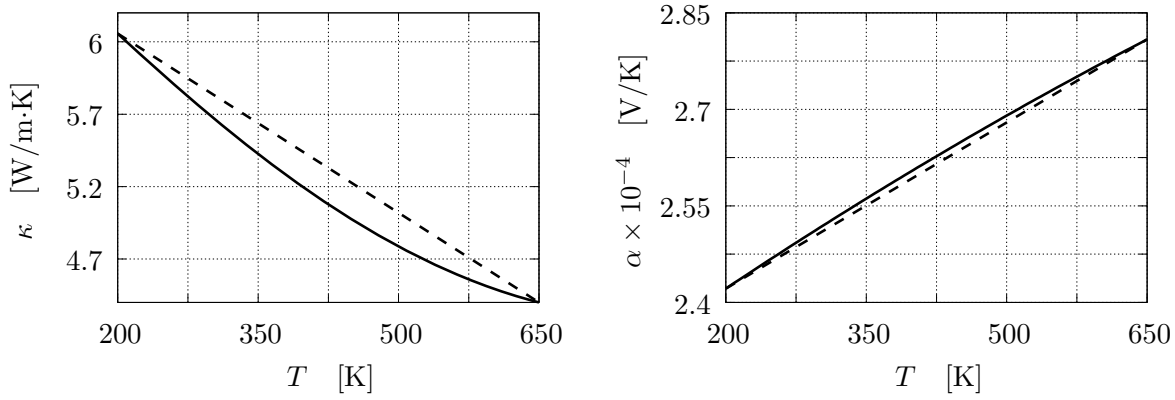

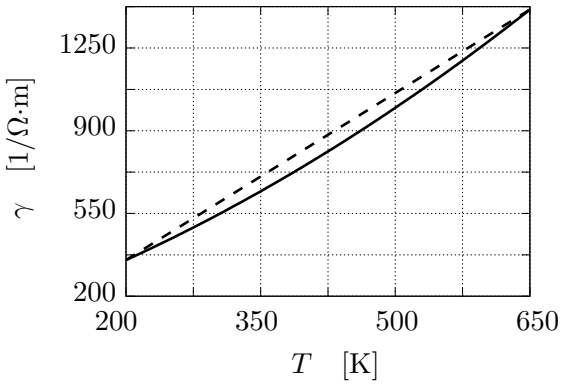

Figure 2.8: Evolution of thermoelectric properties with temperature for $Cu_{0.99}Pt_{0.01}FeO_2$ [21]. Continuous line: real properties; dashed line: linear function approximation

As seen in Figure 2.8 for both types of polynomials, the error introduced by approximating the TE properties from the quadratic to linear polynomial order is negligible in the range of study:

$$\begin{aligned}
\kappa(T) &= \kappa_0 + \kappa_1 T + \cancel{\kappa_2 T^2} \quad &\equiv \quad & 7.296 - 7.02 \times 10^{-3}\ T + \cancel{4.11 \times 10^{-6}\ T^2} \\
\alpha(T) &= \alpha_0 + \alpha_1 T + \cancel{\alpha_2 T^2} \quad &\equiv \quad & 2.23 \times 10^{-4} + 1.04 \times 10^{-7}\ T - \cancel{1.78 \times 10^{-10}\ T^2} \\
\gamma(T) &= \gamma_0 + \gamma_1 T + \cancel{\gamma_2 T^2} \quad &\equiv \quad & 114.30 + 1.13\ T + \cancel{8.93 \times 10^{-4}\ T^2}
\end{aligned} \tag{2.25}$$

Simulations of the Seebeck effect are performed prescribing a T–gradient along the x–direction and fixing only $V_L = 0$. The main difference between this Seebeck and the previous Joule-Seebeck effects is the electric current $j_x = 0$ [18]. The balance and the equilibrium equations particularized for this case are:

$$\begin{cases}
0 = -\gamma(T)\ A_c\ \dfrac{\mathrm{d}V}{\mathrm{d}r}\ -\ \alpha(T)\ A_c\ \gamma(T) \dfrac{\mathrm{d}T}{\mathrm{d}r} \\
q_r = -\kappa(T)\ A_c\ \dfrac{\mathrm{d}T}{\mathrm{d}r} \\
\dfrac{\mathrm{d}q_r}{\mathrm{d}r} = 0
\end{cases} \tag{2.26}$$

- **Annular fin**

For this case, the heat and electrical conductive area is defined as the thickness t multiplied

by the circumference perimeter: $A_c = 2\pi rt$. The three BCs that need to be taken into account are:

$$V(r = r_0) := V_L \; ; \qquad T(r = r_0) := T_L \; ; \qquad T(r = r_L) := T_0 \tag{2.27}$$

Solving the first equation from the Eqs. (2.26) and prescribing the first and second BCs, the V–distribution is obtained with $Mathematica^{®}$:

$$V = C_3 - \frac{1}{2}T\,(2\alpha_0 + \alpha_1 T) \qquad \rightarrow \qquad V = \alpha_0 T_L \; + \; \frac{\alpha_1 {T_L}^2}{2} + V_L - \frac{1}{2}\,T\;(2\alpha_0 + \alpha_1 T) \tag{2.28}$$

The thermal field is solved with a system composed of the second and third equations and the second and third BCs including q_r and T variables:

$$q_r = C_1 \; ; \qquad T = \frac{-\kappa_0}{\kappa_1} + \frac{\kappa_1 \sqrt{{\kappa_0}^2\,\pi + 2\kappa_1\,\pi\,C_2 - \kappa_1\,C_1\,\log(r)}}{\sqrt{\pi}} \tag{2.29}$$

Applying the second and third temperature BCs, the T–distribution and q_r is obtained with $Mathematica^{®}$:

$$q_r = \frac{\pi\,[2\kappa_0(T_0 - T_L) + 2\kappa_1\,(T_0^2 - T_L^2)]}{\log(r_L) - \log(r_0)}$$

$$\begin{aligned} T = \frac{-\kappa_0}{\kappa_1} + \kappa_1 \sqrt{\frac{(\kappa_0 - \kappa_1 T_0)^2 \log(r_L) - (\kappa_0 - \kappa_1 T_L)^2 \log(r_0)}{\log(r_L) - \log(r_0)}} + \\ + \; \kappa_1 \sqrt{\frac{\kappa_1 (T_L - T_0)[2\kappa_0 + \kappa_1 (T_0 + T_L)]\log(r)}{\log(r_L) - \log(r_0)}} \end{aligned} \tag{2.30}$$

Due to the symmetry only 1/4 of the fin is analyzed and discretized into 16×16 rectangular elements of $elmt12.f$; this mesh contains a total of 289 nodes. The $FEAP$ and the analytical solutions fit perfectly. It should be noted that even if there is no electric current, a V–distribution appears due to the Seebeck effect.

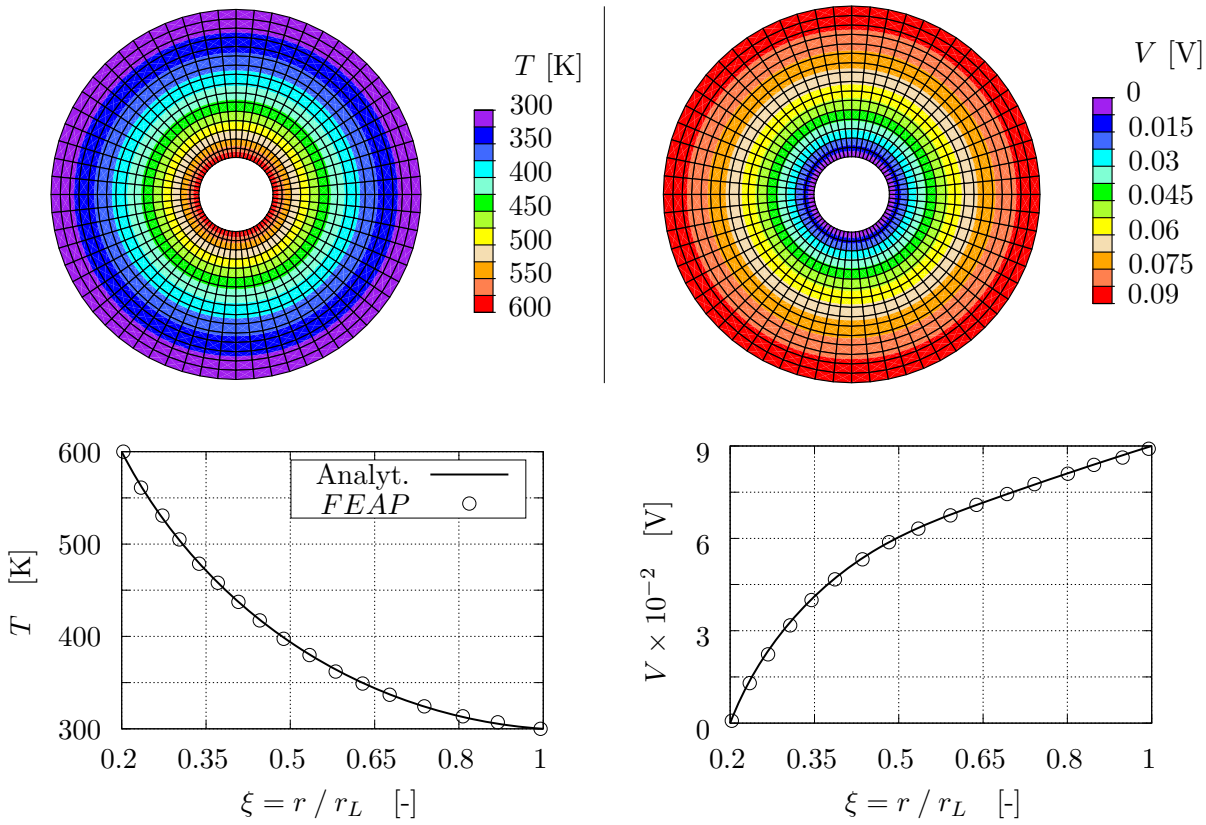

Figure 2.9: Analytical and numerical results of temperature and voltage distributions for the annular fin.

2.1.6 Formulation of thermo–galvano–magnetic phenomena

The presence of a magnetic field affects the coefficients κ, γ, α of semiconductors. As a consequence, thermo–magnetic, galvano–magnetic and thermo–galvano–magnetic effects can be observed. The four phenomena that are analyzed in this subsection are:

- **Righi-Leduc** (thermo–magnetic, also named thermal Hall effect): with the prescription of $\nabla_y T$ and also a perpendicular (to the plane) magnetic field B_z, see Figure 2.10a), not only vertical heat flux q_y appears but also $\nabla_x T$:

$$\nabla_x T = M B_z q_y \tag{2.31}$$

  where M is the Righi-Leduc coefficient.

- **Hall** (galvano–magnetic effect): with the prescription of $\nabla_y V$ and also a perpendicular (to the plane) magnetic field B_z, see Figure 2.10b), not only vertical electrical flux j_y appears

but also $\nabla_x V$:

$$\nabla_x V = R B_z j_y \tag{2.32}$$

where R is the Hall coefficient.

- **Ettinghausen** (thermo–galvano–magnetic effect): with the prescription of $\nabla_y V$ and also a perpendicular (to the plane) magnetic field B_z, see Figure 2.10c), not only vertical electrical flux q_y appears but also $\nabla_x T$:

$$\nabla_x T = N B_z j_y \tag{2.33}$$

where N is the Nernst-Ettinghausen coefficient.

- **Nernst** (thermo–galvano–magnetic effect): with the prescription of $\nabla_y T$ and also a perpendicular (to the plane) magnetic field B_z, see Figure 2.10d), not only vertical heat flux q_y appears but also $\nabla_x V$:

$$\nabla_x V = N B_z q_y \tag{2.34}$$

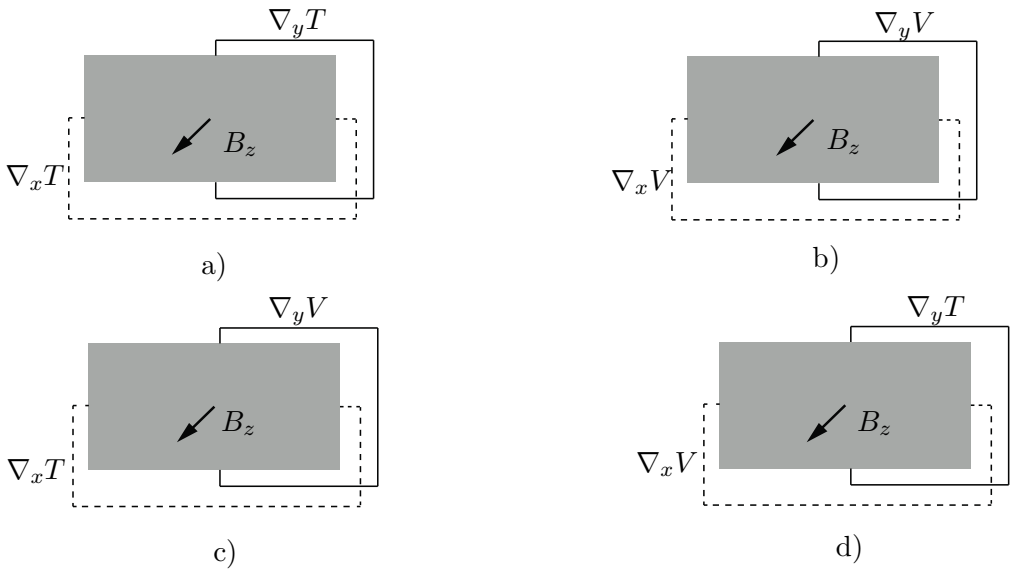

Figure 2.10: Representation of the four thermo–galvano–magnetic phenomena. Continuous line: prescribed temperature or voltage gradient; dashed line: the consequence of a particular phenomenon. a) Righi-Leduc; b) Hall; c) Ettinghausen; d) Nernst.

The balance equations for describing these phenomena are similar to those of the TE formulation, with the difference that now electric $\boldsymbol{j}$ and thermal $\boldsymbol{q}$ fluxes are vectors and $\boldsymbol{\alpha}$, $\boldsymbol{\kappa}$, $\boldsymbol{\gamma}$ tensors, according to Landau formulation [22]:

$$\begin{cases} \boldsymbol{j} = -\boldsymbol{\gamma}\nabla V \ - \boldsymbol{\gamma}\boldsymbol{\alpha}\nabla T \\ \\ \boldsymbol{q} = -\boldsymbol{\kappa}\nabla T + \boldsymbol{\alpha}\boldsymbol{j}T \end{cases} \tag{2.35}$$

$$\boldsymbol{\alpha} = \begin{bmatrix} \alpha & -NB_z \\ NB_z & \alpha \end{bmatrix} ; \qquad \boldsymbol{\rho} = \begin{bmatrix} \rho & -RB_z \\ RB_z & \rho \end{bmatrix} ; \qquad \boldsymbol{\kappa} = \begin{bmatrix} \kappa & -MB_z \\ MB_z & \kappa \end{bmatrix}$$

where $\rho = 1/\gamma$.

Expanding the Eqs. (2.35) all phenomena can be observed:

$$\begin{aligned} \boldsymbol{j} &= -\overbrace{\gamma\nabla V}^{Ohm} - \overbrace{\gamma\alpha\nabla T}^{Seebeck} + \gamma\left(\overbrace{NB_z \times \nabla T}^{Nernst} + \overbrace{RB_z \times \boldsymbol{j}}^{Hall}\right) \\ \boldsymbol{q} &= \underbrace{-\kappa\nabla T}_{Fourier} - \underbrace{\alpha\boldsymbol{j}T}_{Peltier} + \underbrace{NB_zT \times \nabla j}_{Ettinghausen} + \underbrace{MB_z \times \nabla T}_{Righi-Leduc} \end{aligned} \tag{2.36}$$

The equilibrium equations for steady-state and thermo–galvano–magnetic effects are:

$$\begin{cases} \nabla \cdot \boldsymbol{j} = 0 \\ \\ -\nabla \cdot \boldsymbol{q} + \boldsymbol{j}E = 0 \end{cases} \tag{2.37}$$

Substituting the second of Eqs. (2.36) into the second equation of Eqs. (2.37):

$$\underbrace{\nabla(\kappa\nabla T)}_{Conduction} + \underbrace{\frac{j^2}{\gamma}}_{Joule} \underbrace{- T\,\boldsymbol{j}\,\frac{\partial\alpha}{\partial T}\nabla T}_{Thomson} + \underbrace{\frac{1}{\gamma T}\,\frac{\partial(\gamma NT^2)}{\partial T}\,(\boldsymbol{j} \times B_z)\,\nabla T}_{Thomson+B_z} = 0 \tag{2.38}$$

From the previous expression it should be noted that the third term corresponds to the Thomson effect and the fourth term to the changes in the Thomson effect resulting from the presence of B_z; these two terms appear if α, γ or N are function of temperature. In this section these terms will be null since the coefficients will be considered constants.

2.1.7 Simulations of steady-state thermo–galvano–magnetic phenomena

In this subsection Righi-Leduc, Hall and Ettinghausen-Nernst effects are studied for a square thin film simulated with *elmt*12.*f* as seen in Figure 2.11.

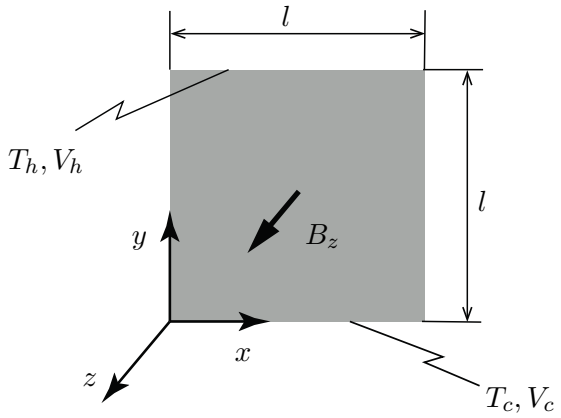

Figure 2.11: Dimensions and boundary conditions of the mesh used in steady-state thermo–galvano–magnetic phenomena simulations.

The length of the square is $l = 1.14 \times 10^{-3}$ [m] and the BCs prescribed for each phenomena are listed in Table 2.5. The B_z chosen for the Righi-Leduc effect is one order of magnitude greater than for the rest since this phenomenon is difficult to appreciate at low B_z.

Interaction	T_h [°C]	T_c [°C]	V_h [V]	V_c [V]	B_z [T]
Righi-Leduc	50	25	-	-	5
Hall	-	-	0	0.1	0.5
Ettinghausen-Nernst	50	0	0	0.1	0.5

Table 2.5: The boundary conditions for Righi-Leduc, Hall and Nernst effects.

All cases will be run for $InSb$ material, the properties of which are considered invariable with T. For simplicity and as for all further simulations in this subsection $\alpha_m, \gamma_m, \kappa_m$ are taken at a given temperature; these properties are from now denoted as α, γ, κ.

Parameter	**Value**	**Units**
α	-2.825×10^{-4}	[V/K]
γ	2.45×10^{4}	[1/Ω· m]
κ	10.81	[W/m·K]

Parameter	**Value**	**Units**
N	-6.4×10^{-5}	[m^2/K·s]
R	-2.465×10^{-4}	[m^3/A·s]
M	5×10^{-2}	[m^2/V·s]

Table 2.6: Properties of $InSb$ material for constant temperature $T = 37.5$°C.

- **The Righi-Leduc effect**

For this case, the second balance expression from the Eqs. (2.36) considering only the Fourier

and Righi-Leduc effects, and the second equilibrium expression from the Eqs. (2.37) with $\boldsymbol{j} = 0$ are taken into account:

$$\begin{Bmatrix} q_x \\ \\ q_y \end{Bmatrix} = \begin{bmatrix} \kappa & -MB_z \\ \\ MB_z & \kappa \end{bmatrix} \begin{Bmatrix} \nabla_x T \\ \\ \nabla_y T \end{Bmatrix} ; \qquad \kappa \left(\nabla_x^2 T + \nabla_y^2 T \right) = 0 \tag{2.39}$$

The expression at the right can be classified as a Laplace equation, a second order PDE, that can be numerically solved with the finite-difference-method (FDM). The idea of FDM is to replace partial derivatives with finite differences and as a consequence the PDE is converted into a set of linear equations. From this point, the further formulation described for this case is taken from [24], [25].

A general Laplace equation and its solution have the form:

$$\begin{aligned} & K_x \nabla_x^2 x + K_y \nabla_y^2 y = 0 \qquad \rightarrow \\ & K_x \frac{1}{\Delta x^2}(u_{i-1,j} - 2u_{i,j} + u_{i+1,j}) + K_y \frac{1}{\Delta y^2}(u_{i-1,j} - 2u_{i,j} + u_{i+1,j}) = 0 \end{aligned} \tag{2.40}$$

where K_x, K_y are constant numbers and u is the unknown quantity. The previous expression can be expressed as follows:

$$u_{i,j} = \frac{K_y \Delta y^2 (u_{i+1,j} + u_{i-1,j}) + K_x \Delta x^2 (u_{i,j+1} + u_{i,j-1})}{2(K_x \Delta x^2 + K_y \Delta y^2)} \tag{2.41}$$

For a square finite-differences, it should be considered that $\Delta x = \Delta y$ and since both derivatives from the right expression of the Eqs. (2.39) are multiplied by the same constant, then $K_x = K_y$.

In the Figure 2.12 left, the grid points considered in the Eq. (2.41) are represented. As it is pointed out in the Figure 2.12 right, only the internal grid points of the mesh can be calculated with the Eq. (2.41), while the top $u_{1,m}$ and the bottom $u_{17,m}$ quantities of the boundary grid points (represented in blue color) are prescribed (Derichlet condition).

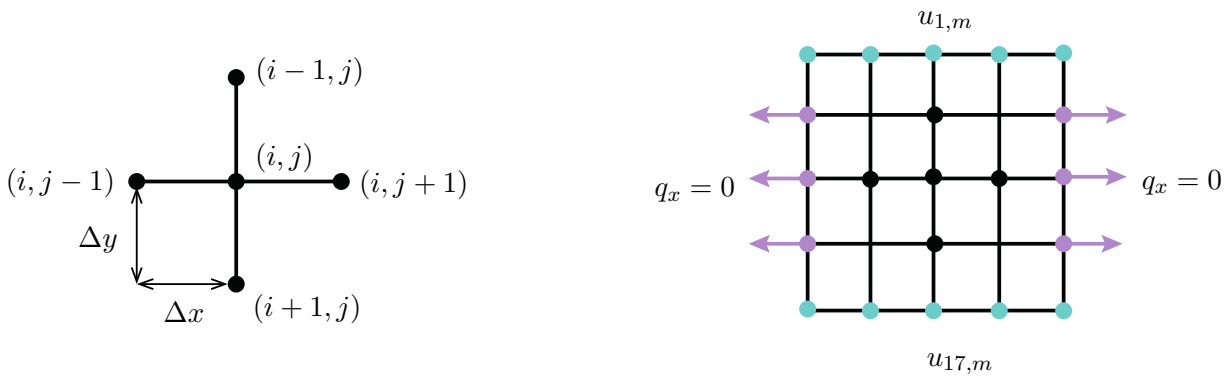

Figure 2.12: Representation of the finite-difference-method mesh. In blue color prescribed boundary conditions; in purple color adiabatic boundary condition.

In this case, the square is discretized into a 17×17 matrix and as a consequence 289 nodal T–values can be obtained. As said before $u_{i,j}$ are the unknowns quantities that for the right expression of Eqs. (2.39) are T–values. The algorithm solved with $Matlab^{®}$ is:

$$u_{1,m} = T_h \; ; \qquad u_{17,m} = T_c \; ; \qquad u_{i,j} = \frac{u_{i+1,j} + u_{i-1,j} + u_{i,j+1} + u_{i,j-1}}{4} \tag{2.42}$$

where $m = 1 : 17$.

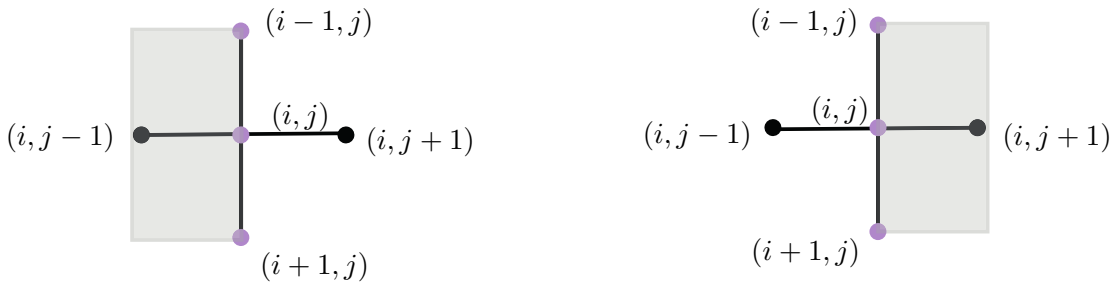

Figure 2.13: Representation of the finite-difference-method for the Neumann conditions. In purple the boundary grid points for $x = 0$ at the left and $x = l$ at the right.

It should be noted that only BCs at the horizontal sides are prescribed. In order to complete the missing BCs for the vertical sides, normal derivatives to these boundaries should be introduced (Neumann condition).

In the Figure 2.13 left, the external side $x = 0$ is represented: the point $u_{i,j-1}$ is outside

of the mesh. In order to calculate the value of $u_{i,j}$ at the external side, the fictitious $u_{i,j-1}$ is obtained from the normal derivative to the boundary and substituted into the Eq. (2.41):

$$\nabla_x u = \frac{u_{i,j+1} - u_{i,j-1}}{2\Delta x} \qquad \rightarrow \qquad u_{i,j-1} = -2\Delta x\, \nabla_x u + u_{i,j+1} \tag{2.43}$$

$$u_{i,j} = \frac{u_{i-1,j} + u_{i+1,j} + 2u_{i,j+1} - 2\Delta x\, \nabla_x u}{4}$$

The same procedure is followed for the $x = l$ side; as seen in the Figure 2.13 right, $u_{i,j+1}$ is outside the mesh and it is defined with the normal derivative to the boundary:

$$\nabla_x u = \frac{u_{i,j+1} - u_{i,j-1}}{2\Delta x} \qquad \rightarrow \qquad u_{i,j+1} = 2\Delta x\, \nabla_x u + u_{i,j-1} \tag{2.44}$$

$$u_{i,j} = \frac{u_{i-1,j} + u_{i+1,j} + 2u_{i,j-1} + 2\Delta x\, \nabla_x u}{4}$$

The real known BC is the absence of electric $j_x = 0$ or thermal $q_x = 0$ flux transfer through the boundary represented in the Figure 2.12 right with purple color. From the second condition, $\nabla_x T$ is obtained from the first row of the left Eqs. (2.39) equating $q_x = 0$.

$$q_x = 0\ ; \qquad \rightarrow \qquad \nabla_x T = \frac{MB_z}{\kappa} \nabla_y T \tag{2.45}$$

Substituting the Eq. (2.45) into the final expression $u_{i,j}$ from Eqs. (2.43) and Eqs. (2.44), the T–values for $x = 0$ and $x = l$ are obtained.

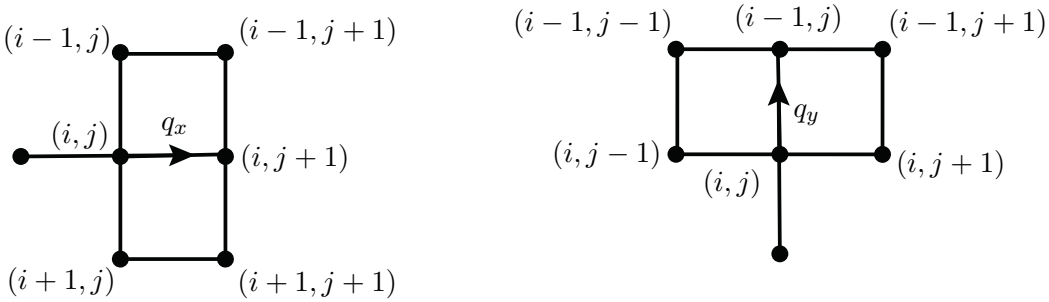

Figure 2.14: Representation of the finite-difference-method mesh for obtaining thermal fluxes for x and y directions.

When all the values of $u_{i,j}$ are known, q_x and q_y can be calculated along the line segment that connects two points: $u_{i,j}$, $u_{i,j+1}$ for q_x as seen in Figure 2.14 right and $u_{i,j}$, $u_{i-1,j}$ for q_y as seen in Figure 2.14 left. For q_x, the potential derivatives can be approximated as:

$$\nabla_x V = \frac{-u_{i,j} + u_{i,j+1}}{\Delta x} \; ; \qquad \nabla_y V = \frac{-u_{i-1,j-1} - u_{i-1,j+1} + u_{i+1,j-1} + u_{i+1,j+1}}{2\Delta y} \tag{2.46}$$

For q_y defined in the Eqs. (2.39), the potential derivatives are:

$$\nabla_y V = \frac{-u_{i,j} + u_{i+1,j}}{\Delta y} \; ; \qquad \nabla_x V = \frac{-u_{i-1,j-1} - u_{i+1,j-1} + u_{i-1,j+1} + u_{i+1,j+1}}{2\Delta x} \tag{2.47}$$

For the boundary grid points of the mesh at $x = 0$ and at $x = l$, as mentioned before $q_x = 0$ and q_y from the Eqs. (2.39) left is obtained substituting the right expression of the Eq. (2.45) into the q_y definition:

$$q_x = 0 \; ; \qquad q_y = \nabla_y T \left[\frac{(MB_z)^2}{\kappa} + \kappa \right] \tag{2.48}$$

The *FEAP* mesh is discretized into the same number of nodes as that of the FDM matrix. q_x, q_y obtained by both methods fit well along the x–coordinate as seen in the middle and bottom of the Figures 2.15 (notice that the range in the bottom is very small); the T–distribution also fits very well along the y–coordinate. This coherence of results is reached since Neumann and Derichlet conditions are combined in the FDM method. Another aspect that can be taken into account is that both FEM and FDM methods are an approximation to the real solution. In fact, FDM is an approximation of derivative terms of a PDE to discrete algebraic relationship (Taylor series), while FEM is an integral scheme over the element [52].

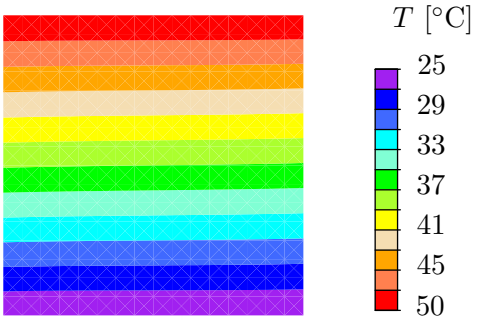

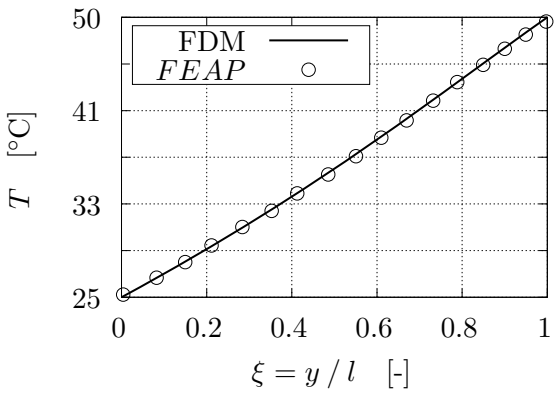

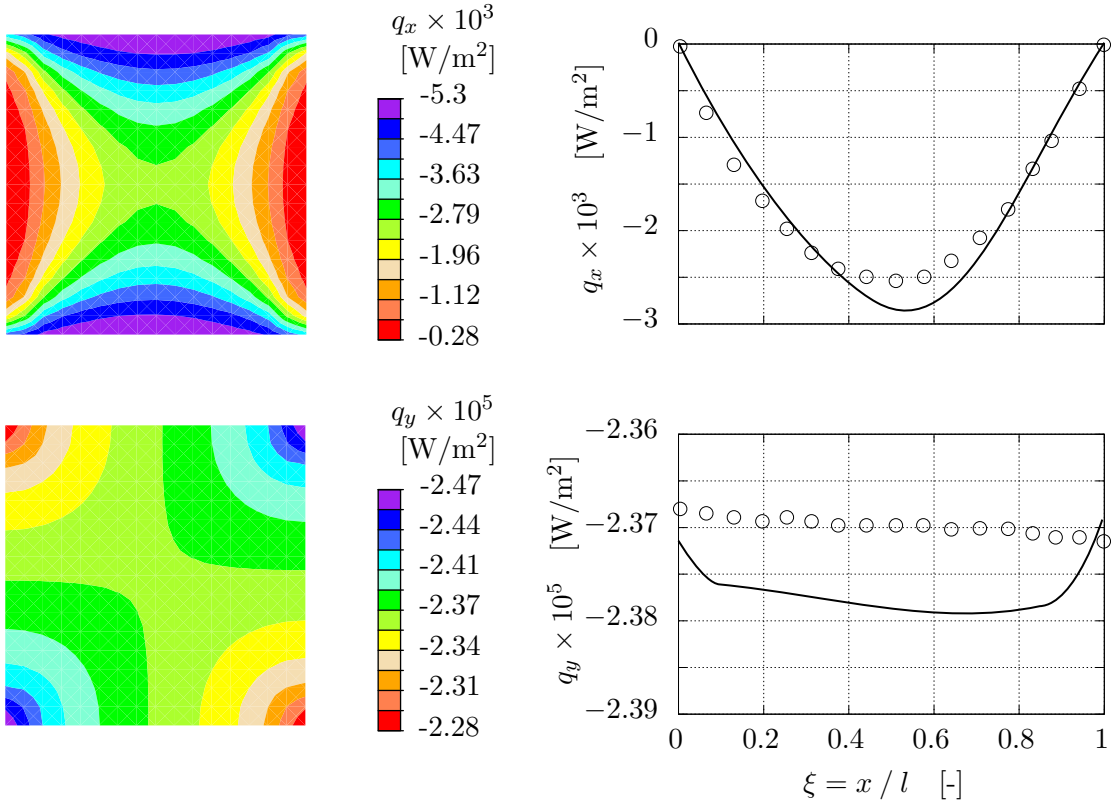

Figure 2.15: Analytical, numerical results of temperature and thermal flux distributions for square mesh under Righi-Leduc effect. Top figure along $x = l/2$, others along $y = l/2$.

It should be pointed out that if the simulation would be run without B_z, only the Fourier effect would be observed. To make the contribution of the Righi-Leduc phenomenon visible, in the Table 2.7 the Fourier and the Righi-Leduc thermal fluxes are compared. As seen, with Righi-Leduc q_x is not null and q_y is slightly incremented; the appearance of q_x is the basis of the Righi-Leduc phenomenon.

$\xi = x\ /\ l$	$\xi = 0$	$\xi = 0.25$	$\xi = 0.5$	$\xi = 0.75$	$\xi = 1$
$q_{x_{Fourier}}$	0	0	0	0	0
q_x	-281	-1.79 $\times 10^3$	-2.73 $\times 10^3$	-1.35 $\times 10^3$	-288.9
$q_{y_{Fourier}}$	-2.3706 $\times 10^5$	-2.3706 $\times 10^5$	-2.3706 $\times 10^5$	-2.3706 $\times 10^5$	-2.3706 $\times 10^5$
q_y	-2.368 $\times 10^5$	-2.369 $\times 10^5$	-2.373 $\times 10^5$	-2.374 $\times 10^5$	-2.374 $\times 10^5$

Table 2.7: Numerical comparison between Fourier and Righi-Leduc thermal fluxes along $y = l/2$.

- **The Hall effect**

For this effect, the first balance equation from the Eqs. (2.36) considering only Ohm and Hall effects and the first equilibrium equation from the Eqs. (2.37) are:

$$\begin{Bmatrix} j_x \\ \\ j_y \end{Bmatrix} = \frac{1}{\rho^2 + (RB_z)^2} \begin{bmatrix} \rho & RB_z \\ \\ -RB_z & \rho \end{bmatrix} \begin{Bmatrix} \nabla_x V \\ \\ \nabla_y V \end{Bmatrix} ; \qquad \frac{\rho}{\rho^2 + (RB_z)^2} \left(\nabla_x^2 V + \nabla_y^2 V \right) = 0 \tag{2.49}$$

The previous system contains three equations with three unknown quantities, but this system is difficult to solve analytically. In order to obtain an approximate solution, some simplifications will be assumed.

Firstly, from the Eq. (2.49) left it should be noted that the diagonal and off-diagonal terms of $\boldsymbol{\gamma}$ are of the same order of magnitude; as a consequence $\partial V/\partial x$ has the same influence as $\partial V/\partial y$ on both electric fluxes and it cannot be neglected. The V–distribution in the Hall effect is completely 2D and it cannot be simplified to 1D.

The Hall voltage V_{hl} along the x–direction is obtained from the balance of forces related to moving electrons, formulation extracted from [26]. When an electric current j_y is prescribed in presence of B_z, a magnetic force f_m appears; this force deflects the charge carriers to one of the semiconductor sides. The accumulation of these charges results in a transversal Hall's electric field E_h and an opposite to f_m named Hall's force f_h appears. Equilibrium is reached when f_m is offset with f_h.

$$\left.\begin{aligned} f_m &= -e\, E_h \\ f_h &= eR(j_y \times B_z) \end{aligned}\right\} \qquad f_m = f_h \quad \rightarrow \quad E_h = -R(j_y \times B_z) \tag{2.50}$$

where e is the charge of electrons.

From the E_h at which the equilibrium occurs and the Eq. (2.49), the voltage perpendicular to j_y and to B_z can be obtained.

$$\frac{V_{hl}}{l} = E_h = -RB_z \frac{\rho}{\rho^2 + R^2 B_z^2} \frac{V_c - V_h}{l} \tag{2.51}$$

Solving the previous expression, the V prescribed at the four sides of the square can be defined:

$$V(x=0) = 0\,; \qquad V(x=l) = V_{hl}\,; \qquad V(y=0) = V_c\,; \qquad V(y=l) = V_h \tag{2.52}$$

Next, to obtain the final V–evolution along the semiconductor the right equation from the Eqs. (2.49) is considered. This expression is again a second-order PDE that can be solved with FDM. For this situation Derichlet conditions are directly applied. The square is discretized into 289 nodes as previously and a 17×17 matrix of V–values is calculated. The algorithm expressed in the Eq. (2.41) is introduced into $Matlab^{®}$ with four voltage BCs:

$$u_{m,1} = 0 \; ; \qquad u_{m,17} = V_{hl} \; ; \qquad u_{17,m} = V_c \; ; \qquad u_{1,m} = V_h \tag{2.53}$$

where $m = 1 : 17$.

Now, j_x and j_y can be calculated along a line connecting two V points as for the Righi-Leduc's fluxes; j_x is obtained substituting derivatives from Eqs. (2.46) into the first left expression of the Eqs. (2.49) and j_y substituting derivatives from the Eqs. (2.47) into the second left expression of the Eqs. (2.49).

$\xi = x \,/\, l$	$\xi = 0$	$\xi = 0.25$	$\xi = 0.5$	$\xi = 0.75$	$\xi = 1$
$j_{x_{Ohm}}$	0	0	0	0	0
j_x	9.93 $\times 10^4$	-3.29 $\times 10^5$	-4.39 $\times 10^5$	-2.63 $\times 10^5$	-1.16 $\times 10^5$
$j_{y_{Ohm}}$	2.14 $\times 10^6$	2.14 $\times 10^6$	2.14 $\times 10^6$	2.14 $\times 10^6$	2.14 $\times 10^6$
j_y	6.77 $\times 10^5$	7.39 $\times 10^5$	6.07 $\times 10^5$	6.85 $\times 10^5$	6.88 $\times 10^5$

Table 2.8: Numerical comparison between Ohm and Hall electric fluxes along $y = l/2$.

The $FEAP$ mesh is discretized into the same number of nodes as that of the FDM. The analytical and the $FEAP$ results fit with small error at most of the length and diverge at the extremes as seen in the Figure 2.16. This incoherence appears as the V–value at $x = l$ was estimated with the force equilibrium equations and V at $x = 0$ was considered null.

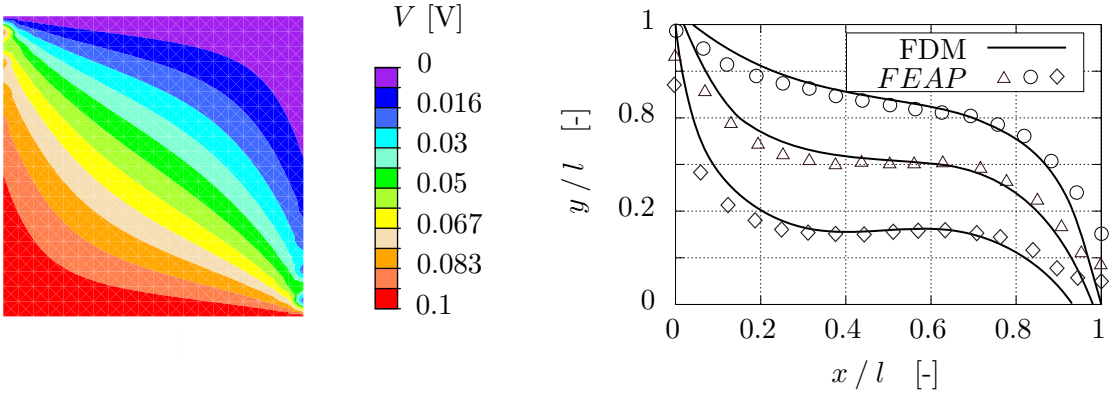

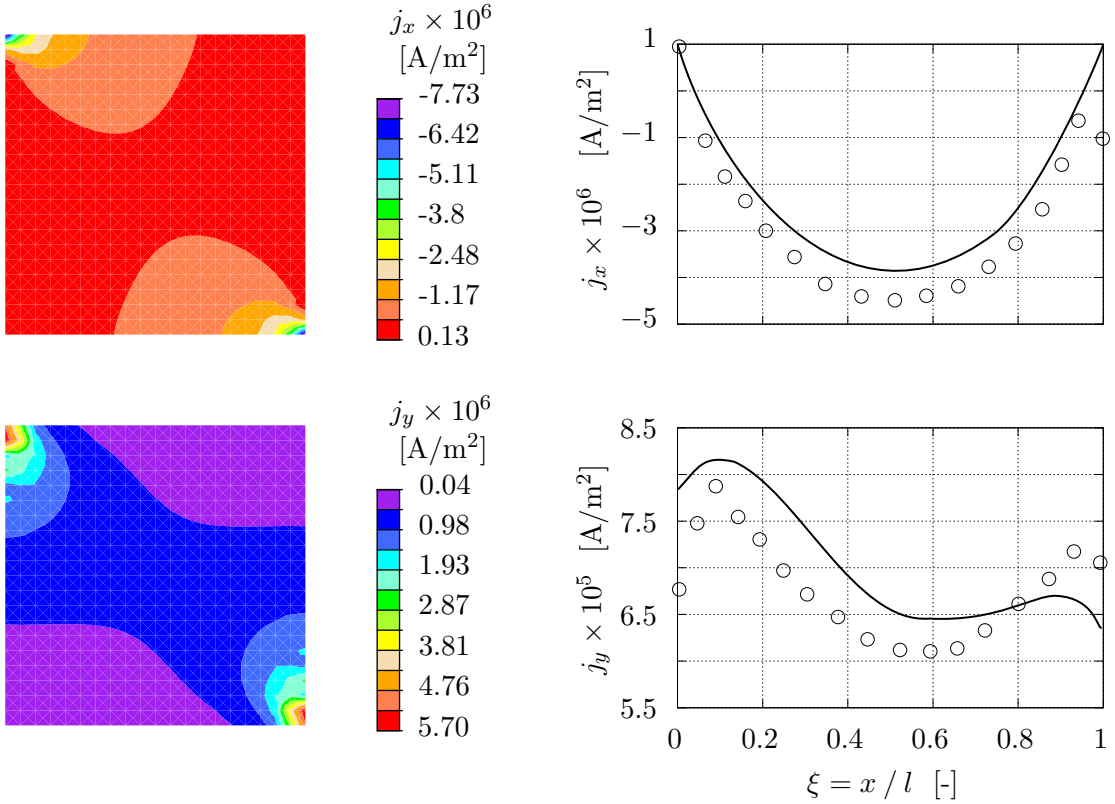

Figure 2.16: Analytical, numerical results of voltage and electric flux distributions for square mesh under Hall effect. Top figure right, isoline map for $V = 0.03$ [V] (circles), $V = 0.05$ [V] (triangles), $V = 0.08$ [V] (squares); middle, bottom figures results along $y = l/2$.

Once again, to make evidence of the magnetic phenomenon, the Hall effect is compared with the Ohm effect when no B_z is applied. According to Ohm's law, the V–distribution is linear, $j_{x_{Ohm}}$ is null and $j_{y_{Ohm}}$ constant and equal to 2.149×10^6 [A/m^2] as seen in the Table 2.8. The appearance of the j_x is the result of the Hall effect, while j_y is diminished due to the negative contribution of $-RB_z \mathrm{d}V/\mathrm{d}x$, see the Eqs. (2.49).

- **The Ettinghausen-Nernst effect**

For this case, the described formulation is again extracted from [24], [25], although in these articles only the final results are presented. From the Eqs. (2.36) all the terms should be considered:

$$\begin{Bmatrix} j_x \\ j_y \end{Bmatrix} = \frac{1}{\rho^2 + (RB_z)^2} \left(- \begin{bmatrix} \rho & RB_z \\ -RB_z & \rho \end{bmatrix} \begin{Bmatrix} \nabla_x V \\ \nabla_y V \end{Bmatrix} - \begin{bmatrix} \rho & RB_z \\ -RB_z & \rho \end{bmatrix} \begin{bmatrix} \alpha & NB_z \\ -NB_z & \alpha \end{bmatrix} \begin{Bmatrix} \nabla_x T \\ \nabla_y T \end{Bmatrix} \right)$$

$$\begin{Bmatrix} q_x \\ q_y \end{Bmatrix} = - \begin{bmatrix} \kappa & -MB_z \\ MB_z & \kappa \end{bmatrix} \begin{Bmatrix} \nabla_x T \\ \nabla_y T \end{Bmatrix} + \begin{bmatrix} \alpha & NB_z \\ -NB_z & \alpha \end{bmatrix} \begin{Bmatrix} j_x \\ j_y \end{Bmatrix} T \tag{2.54}$$

The Eqs. (2.54) is substituted into the Eqs. (2.37) without considering Joule and Thomson effects. Calculating the divergence of $\boldsymbol{q}$, $\boldsymbol{j}$ some terms are simplified and the T and V at internal grid points will be calculated with the equations:

$$\begin{aligned} \nabla \cdot \boldsymbol{q} = 0 \; ; \qquad & \rightarrow \qquad \left(\kappa - \frac{N^2 \, T \, B^2}{\rho} \right) \nabla^2 T = -\rho \, j^2 \\ \nabla \cdot \boldsymbol{j} = 0 \; ; \qquad & \rightarrow \qquad \frac{\rho}{\rho^2 + (RB_z)^2} \, \nabla^2 V = - \frac{B_z^2 \, N \, R}{\rho^2 + (RB_z)^2} \, \nabla^2 T \end{aligned} \tag{2.55}$$

It should be noted that both expressions at the Eqs. (2.55) right are not homogeneous like the Eq. (2.40). In that way, the Laplace formulation changes from that of the Eq. (2.42) to:

$$u_{i,j} = \frac{u_{i+1,j} + u_{i-1,j} + u_{i,j+1} + u_{i,j-1}}{4} - \frac{h^2}{4} F \tag{2.56}$$

where $F := \nabla^2 T$ when T values are calculated, and $F = \nabla^2 V$ when V values are calculated. The term $h^2 F/4$ is now appended to the boundary of $u_{i,j}$ expressed in Eqs. (2.43) and (2.44).

Firstly, T–distributions for the vertical sides at $x = 0$ and $x = l$ are calculated:

$$\begin{aligned} T_{i,1} &= \frac{T_{i-1,1} + T_{i+1,1} + 2T_{i,2} - 2\Delta x \, \nabla_x T}{4} - \frac{h^2}{4} F \\ T_{i,17} &= \frac{T_{i-1,17} + T_{i+1,17} + 2T_{i,16} + 2\Delta x \, \nabla_x T}{4} - \frac{h^2}{4} F \end{aligned} \tag{2.57}$$

where $\nabla_x T$ can be obtained from the Eqs. (2.54) and the known BCs $q_x = j_x = 0$:

$$\nabla_x T = \frac{-B_z j_y \, N \, T - B_z M \nabla_y T}{\kappa} \tag{2.58}$$

As seen from the previous expression $\nabla_x T$, depends on j_y of the vertical sides.

The general j_y defined in the Eqs. (2.54) is a linear function of $\nabla_x T,\ \nabla_y T,\ \nabla_x V$ and $\nabla_y V$; in order to obtain j_y along the vertical boundary sides, $\nabla_x V$ is obtained again from the known adiabatic BCs $q_x = j_x = 0$. In that way, $\nabla_x V$ is obtained from $j_x = 0$:

$$\nabla_x V = \frac{(-B_z\, N\, R\ -\ \alpha\, \rho)\, \nabla_x T\ +\ (-\alpha\, B_z R\ +\ B_z N\, \rho)\, \nabla_y T - B_z R\, \nabla_y V}{\rho} \tag{2.59}$$

The expressions of $\nabla_x V$ and $\nabla_x T$ defined previously are substituted into j_y from the Eqs. (2.54):

$$\begin{aligned} j_y &= \frac{B_z^2 N\ (j_y N\, T\ +\ M \nabla_y T)\ -\ \kappa\, (\alpha \nabla_y T\ +\ \nabla_y V)}{\kappa\, \rho}\ ; \qquad \rightarrow \\ j_y &= \frac{\alpha\, \kappa\, \nabla_y T\ -\ B_z^2 M\, N\, \nabla_y T\ +\ \kappa\, \nabla_y V}{-\kappa\, \rho\ +\ B_z^2 N^2 T} \end{aligned} \tag{2.60}$$

The last expression defines the j_y for the vertical boundary and can be substituted into the Eq. (2.58) and then the T–distribution along the vertical sides from the Eqs. (2.57) can be calculated.

Secondly, to solve the V–distribution at the vertical sides, a different mathematical method is applied. Once again taking the formulation of j_x, j_y from the Eqs. (2.54) and separating only the $V_{i,j}$ term:

$$j_{i,j}^x = \frac{\rho\, V_{i,j}}{\Delta x\, (\rho^2 + R^2 B_z^2)} + I\ ; \qquad\qquad j_{i,j}^y = \frac{\rho\, V_{i,j}}{\Delta y\, (\rho^2 + R^2 B_z^2)} + I \tag{2.61}$$

where I represents terms independent of $V_{i,j}$, and both fluxes are drawn in the Figure 2.17.

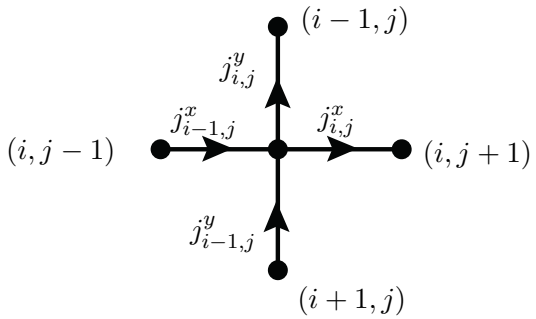

Figure 2.17: Representation of the electric flux for x and y directions according to finite-difference-method.

As seen in the figure, if the sum of in-going and out-going fluxes at $u_{i,j}$ is calculated, an expression for $V_{i,j}$ can be obtained:

$$j_{i,j}^{out} = j_{i,j}^{x} + j_{i,j}^{y} - j_{i-1,j}^{x} - j_{i,j-1}^{y} = \frac{4\,\rho\,V_{i,j}}{\Delta x\ (\rho^2 + R^2 B^2)}\ ; \qquad (2.62)$$

$$V_{i,j} \quad \rightarrow \quad V_{i,j} \ - \ j_{i,j}^{out}\,\frac{\Delta x\,(\rho^2 + R^2 B_z^2)}{4\rho}$$

In the last expression the I–terms from the Eqs. (2.61) vanish, and then $V_{i,j}$ is improved through iterations (from initial zero values).

Finally, when all 17×17 values for T and V are obtained, as well as electric and thermal fluxes. The same procedure as that of the previous cases is followed: the derivatives from Eqs. (2.46) and Eqs. (2.47) are substituted into the flux definitions from the Eqs. (2.54).

The *FEAP* mesh is discretized into the same number of elements as that of the FDM. As can be seen from the graphics, both fluxes have similar evolutions along the x–direction, but their magnitudes are slightly different.

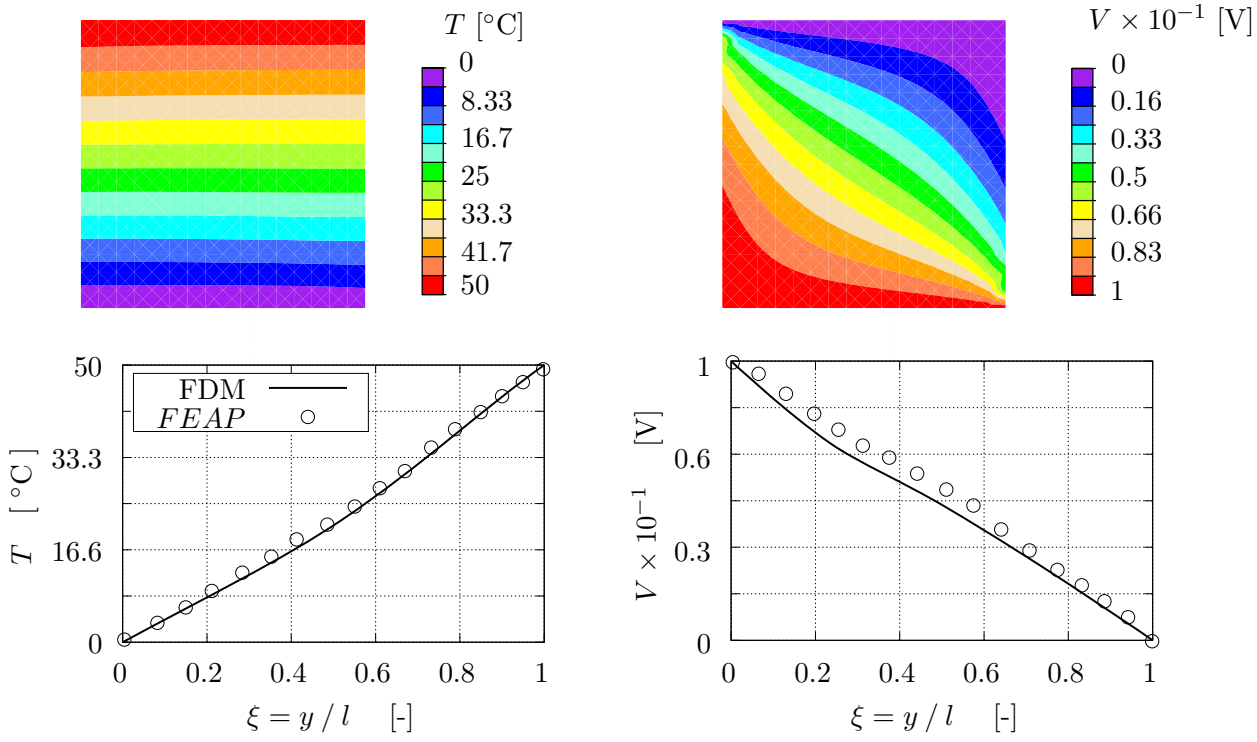

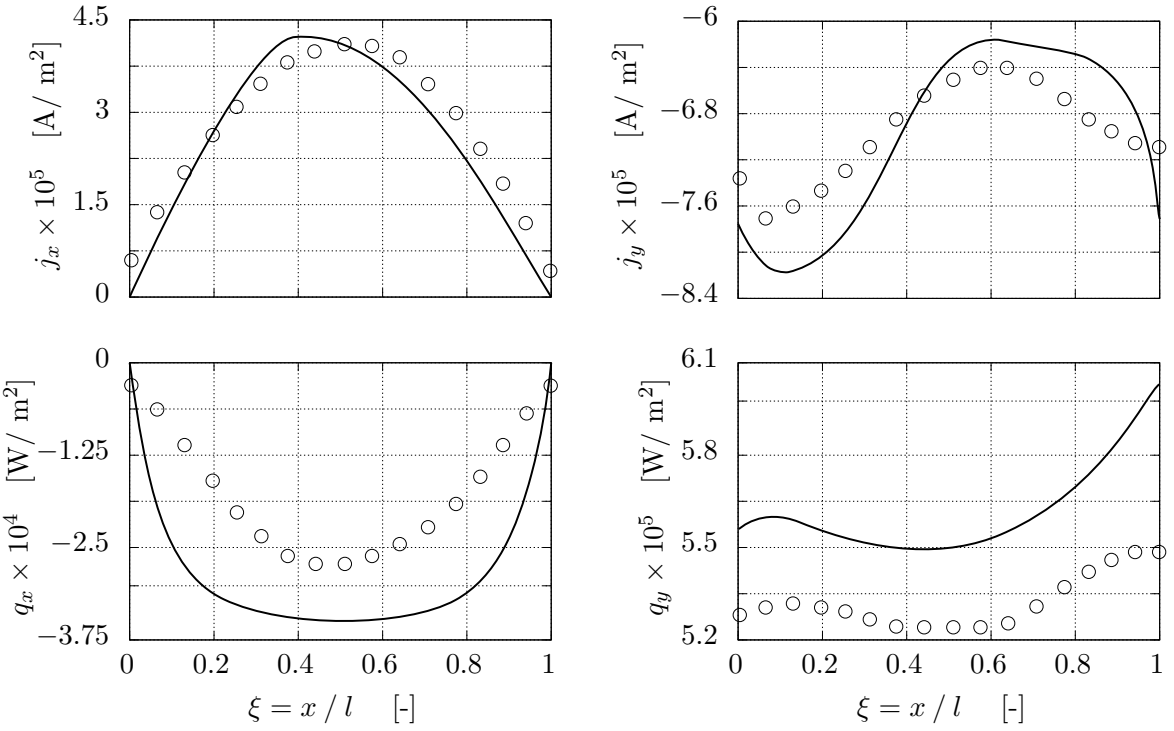

Figure 2.18: Analytical, numerical results of temperature, voltage and their fluxes for square mesh under Ettinghausen-Nernst effect. Top figure along $x = l/2$, others along $y = l/2$.

In order to understand the influence of the magnetic field, the present *FEAP* results for Ettinghausen-Nernst are compared to results of a problem with the same BCs but with $B_z = 0$, case that corresponds to the Joule-Seebeck effect, of Eqs. (2.16). This formulation is simplified considering that the cross-section area A_c of the square is constant. Only the final results obtained with *Mathematica*® are written:

$$j_{x_{JS}} = -\frac{\alpha\,\gamma(T_h - T_c) + \gamma(V_h - V_c)}{l}\,; \qquad V_{_{JS}} = \alpha(T_c - T) + V_c + \frac{j_x\,x}{\gamma}$$

$$T_{_{JS}} = \frac{-\gamma\,[\alpha\,(T_c - T_h)\; + V_c - V_h]^2\,(l-x)x + 2\,\kappa\,l\,[T_c\,l + (T_h - T_c)x]}{2\,\kappa\,l^2} \tag{2.63}$$

$$q_{x_{JS}} = \frac{2\,\kappa^2 l^2(T_h - T_c) + \;\kappa\,l^2 j_x\;[\alpha\,l(T_c + T_h) - (V_c - V_h)(l - 2x)] - \alpha\,\gamma\,l j_x^3\;(l-x)\,x}{2\kappa l^3}$$

where the previous T, V, j_x, q_x have the JS subscript that corresponds to the Joule-Seebeck effect.

$\xi = x\ /\ l$	$\xi = 0$	$\xi = 0.25$	$\xi = 0.5$	$\xi = 0.75$	$\xi = 1$
$j_{x_{JS}}$	0	0	0	0	0
j_x	3.59 $\times 10^4$	2.63 $\times 10^5$	3.59 $\times 10^5$	2.17 $\times 10^5$	1.42 $\times 10^4$
$j_{y_{JS}}$	-2.45 $\times$ 10^6	-2.45 $\times$ 10^6	-2.45 $\times$ 10^6	-2.45 $\times$ 10^6	-2.45 $\times$ 10^6
j_y	-7.31 $\times 10^5$	-7.13 $\times 10^5$	-6.41 $\times 10^5$	-6.66 $\times 10^5$	-6.96 $\times 10^5$

Table 2.9: Numerical comparison between Joule-Seebeck and Ettinghausen-Nernst electric fluxes along $y = l/2$.

As seen from the Table 2.9, with the Joule-Sebeck effect the electric flux distribution is purely 1D, but the presence of B_z affects this flux converting it into 2D. The Ettinghausen-Nernst effect also reduces j_y one order of magnitude.

The same conclusions can be obtained for the thermal fluxes seen in the Table 2.10; this thermal flux for Ettinghausen-Nernst is once again 2D. The difference between the electric and the thermal flux is that $q_{y_{JS}}$, q_y maintain the same order of magnitude.

$\xi = x\ /\ L$	$\xi = 0$	$\xi = 0.25$	$\xi = 0.5$	$\xi = 0.75$	$\xi = 1$
$q_{x_{JS}}$	0	0	0	0	0
q_x	-2.1 $\times 10^3$	-1.55 $\times 10^4$	-2.79 $\times 10^4$	-1.32 $\times 10^4$	-1.2 $\times 10^3$
$q_{y_{JS}}$	5.79 $\times$ 10^5	5.08 $\times$ 10^5	4.59 $\times$ 10^5	3.84 $\times$ 10^5	3.34 $\times$ 10^5
q_y	5.28 $\times 10^5$	5.26 $\times 10^5$	5.25 $\times 10^5$	5.36 $\times 10^5$	5.39 $\times 10^5$

Table 2.10: Numerical comparison between Joule-Seebeck and Ettinghausen-Nernst thermal fluxes along $y = l/2$.

3

Measurement techniques of the Hall effect in thin-film semiconductors

In this chapter, a brief theory on the Hall effect and the methods of measurement of its coefficient for thin-film semiconductors are reviewed. The Hall coefficient is calculated from the measured Hall voltage V_{hl}: that is why it is important to estimate V_{hl} as accurately as possible.

V_{hl} measurements are carried out by depositing a semiconductor thin-film on a substrate. Commonly, two configurations are used: the Hall bar and circular or square Van der Pauw (VdP) geometries. Each has advantages and drawbacks that are discussed in this chapter.

Besides the configuration, three techniques can be applied to measure V_{hl}. In the first, V_{hl} is obtained with a single measurement, and the Hall coefficient R is calculated from the classical equation of this effect. This technique is no longer used in laboratories due to intrinsic and geometrical errors in V_{hl}. The other two techniques are the Direct Current (DC) and the Alternating Current (AC) field methods, and were developed to remove undesirable errors [28].

The main objective of this chapter is to simulate methods to obtain R from the V_{hl} results of the cases run with $FEAP$. This V_{hl} is estimated with the AC/DC methods in Hall bars and VdP geometries. The analyses of these cases seek to better understand the process of the measurement.

3.1 The simple theory of the Hall effect

Figure 3.1 presents a fundamental observation of the Hall effect. Considering a semiconductor sample characterized by length L, width w, thickness t, the charge carrier of charge e, and the number of density n.

If an electric field E_x is applied to a semiconductor in the x–direction, a current I_x is created, and charge carriers are moved under the influence of E_x at velocity v_x [27]. The created I_x can be expressed in terms of electric flux j_x or of velocity v_x:

$$I_x = j_x\, w\, t = n\, e\, v_x\, w\, t\ ; \qquad \rightarrow \qquad v_x = \frac{I_x}{n\, e\, w\, t} \tag{3.1}$$

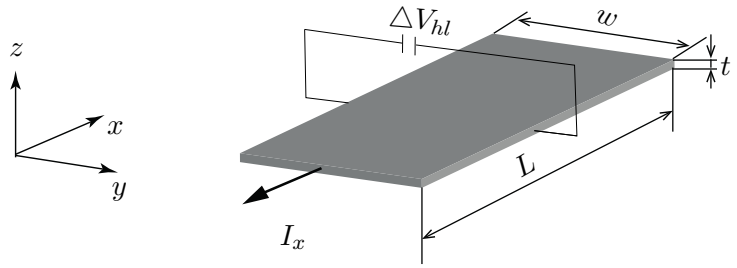

Figure 3.1: Representation of a simple Hall voltage sensor [27].

Now, if the semiconductor is placed under a magnetic field B_z, the charge carriers will experience a Lorentz force $f_{_L}$. This force deflects the charge carriers to one side of the semiconductor. The accumulation of these charges creates a transverse electric field, known as the Hall field E_y, that counteracts $f_{_L}$ and can be expressed as:

$$f_{_L} = e\, v_x \times B_z \; ; \qquad\qquad E_y = v_x B_z \tag{3.2}$$

In an experiment, the measured V_{hl} is related to the integral of E_y over the sample's width:

$$V_{hl} = \int_0^w E_y \mathrm{d}y = -E_y w = -\frac{1}{n\, e}\frac{I_x B_z}{t} \; ; \qquad\qquad R = \frac{1}{n\, e} \tag{3.3}$$

In that way, if V_{hl} is correctly measured and the values of applied B_z, I_x are known, R can easily be calculated from the Eq. (3.3).

3.2 Material and geometrical configuration

3.2.1 Material

The study in this chapter is carried out with an $InSb$ semiconductor as this material presents high R; therefore, a high V_{hl} is created and a distortion in the V–distribution due to the applied B_z is clearly visible. The properties of $InSb$ are summarized in Table 2.6. Commonly, the measurements are done prescribing $B_z = 1$ [T], as a higher value of B_z can affect to κ, α, γ and hinder the measurement of R.

All the cases are run for thin-films of thickness $t = 4\times10^{-4}$ [m], deposited on a Mica substrate of thickness $t_s = 1 \times 10^{-2}$ [m] as seen in Figure 3.2(b). Mica is used since it presents low κ and γ; thus, when the electric flux is applied through the $InSb$, only a little flow rate will go to the

substrate and the error introduced into the measurements of the semiconductor's properties is minimal.

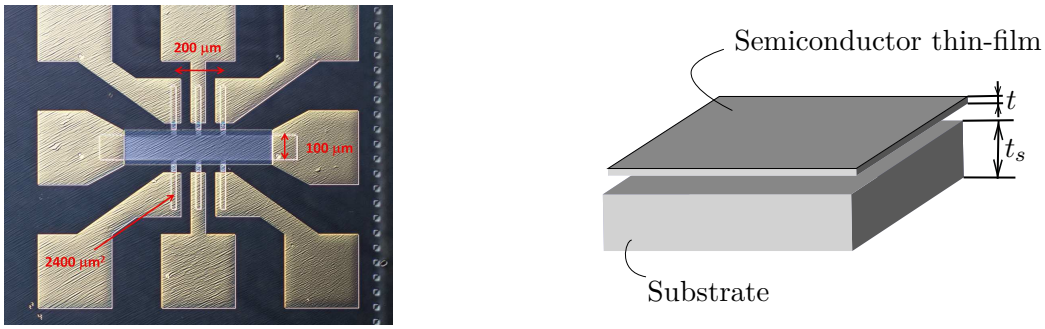

(a) (b)

Figure 3.2: Representation of: (a) laboratory sample of eight-contact Hall bar [53]; (b) configuration of Hall voltage measurement sensor

3.2.2 Elements and the mesh discretization

To determine the number of elements in which the mesh is discretized, an analytical mesh convergence study provided in [23] is taken into account. As this study concluded, the minimum number of elements that allow reaching a compromise between calculation time and errors made is between 1500 and 2000.

Through this approach, the semiconductor thin-film is discretized into $(0.025 \times 10^{-3})(0.025 \times 10^{-3})$ rectangular 2D elements of $elmt12.f$ with coupled GM properties; although the $elmt12.f$ is 2D, the semiconductor thickness t is introduced as the material property. Whereas, the substrate is discretized into $(0.025 \times 10^{-3})(0.025 \times 10^{-3})(0.025 \times 10^{-3})$ rectangular 3D elements of $elmt11.f$ with uncoupled thermal and electrical conduction properties.

3.2.3 Hall bars geometries

The Hall bar (see Figure 3.2(a)) is commonly used for measuring electric resistance $\rho(B_z)$ as a function of the magnetic field (also called magneto-resistance) and Hall mobility μ on low resistance semiconductors, since about half of the voltage applied through the sample is measured between the contacts.

The Hall bar geometry includes a minimum of six and a maximum of eight contacts, as seen in Figure 3.3. The extended lateral arms increase the accuracy of the measurements. The main disadvantage is that such a pattern is difficult to fabricate with fragile materials. It is

also strenuous to measure the real width and distance between contacts, both necessary for the $\rho(B_z)$ calculations.

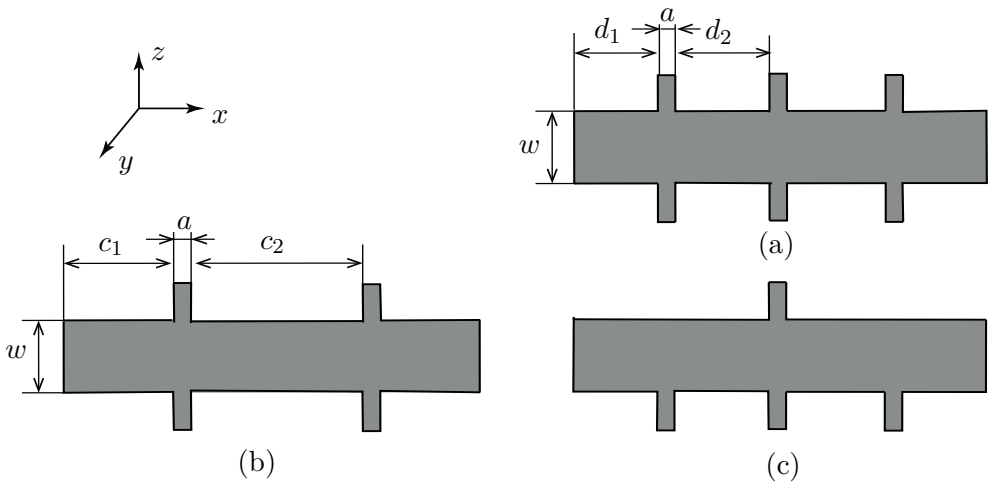

Figure 3.3: Representation of (a) regular eight-contact; (b) regular six-contact; (c) irregular six-contact Hall bar geometries.

The dimensions and shape of regular bars illustrated in Figure 3.3(a), (b) are taken from standard test methods for measuring $\rho(B_z)$ and R of the American Society for Testing and Materials (ASTM) F76, which was re-approved in 2016 [29]. The irregular bar, see Figure 3.3(c), was proposed by the advanced scientific research company Lake Shore Cryotronics® [28]. The dimensions of these bars are summarized in the Table 3.1.

Parameter	**Value**	**Units**
w	0.2×10^{-2}	[m]
a	0.05×10^{-2}	[m]
c_1	0.4×10^{-2}	[m]

Parameter	**Value**	**Units**
c_2	0.6×10^{-2}	[m]
d_1	0.3×10^{-2}	[m]
d_2	0.375×10^{-2}	[m]

Table 3.1: Dimensions for Hall bars represented in Figure 3.3.

Two geometrical aspects need to be taken into account when V_{hl} measurements are done. The first one is the symmetry along the x–direction: if symmetry is maintained $\rho(B_z)$ can be calculated and an additional study on the isotropy of the thin-film can be done (Figure 3.3(a), (b)). The second one is the arms location: if measurements are taken from two symmetrical arms positioned in the center of the sample as in Figure 3.3(a), (c), the R estimation is accurate. Otherwise, the close proximity of the contact arms to the sample ends as in the Figure 3.3(b) causes an underestimation of R.

3.2.4 Van der Pauw geometries

Any arbitrary shape can be considered a VdP geometry if it meets four of the following requirements [30]:

- All the contacts are located on the periphery of the sample.
- All the contacts are sufficiently small.
- The thin-film of the semiconductor is of uniform thickness.
- The sample does not contain holes.

With a VdP geometry, resistivity, carrier concentration, and mobility can be calculated. Although any shape can be used, large errors in measurements arise from contact size and placement. Another drawback is that two voltage measurements are required to calculate $\rho(B_z)$ and R, thus the estimation of VdP takes twice as long as that of the Hall bar approach, in which only one measurement is taken. In this subsection, two shapes are considered: a circle of radius $r = 0.3 \times 10^{-2}$ [m] and a square with a side length $l = 0.3 \times 10^{-2}$ [m].

3.3 Methods of measurement and errors in the Hall coefficient estimation

The V_{hl} cannot be measured with a single reading V_{ME} as it contains spurious voltages [28]:

$$V_{ME} = V_s + V_e + V_n + V_m + V_r + V_{hl} \tag{3.4}$$

The sources of these intrinsic errors are:

- **Thermoelectric voltage** V_s: this term is independent of I_x and B_z and it is the consequence of a small T–gradient along the sample which generates the Seebeck effect.
- **Ettinghausen voltage** V_e: this voltage is proportional to I_x and B_z. It is caused by an internally generated Seebeck effect even if a non T–gradient exists.
- **Nernst voltage** V_n: this voltage is proportional to B_z but not to I_x. V_n is created by electrons diffusing from the hot end of the sample to the cold one, when a longitudinal T–gradient exists. It is the only error that can not be eliminated from the measurement with I_x or B_z reversals.
- **Misalignment voltage** V_m: it appears when voltage contacts V^+, V^- are misaligned

with a distance $\triangle y$ and therefore a longitudinal V–gradient $\triangle V_y$ is created as seen in Figure 3.4; misalignment of the contacts is one of the largest errors in V_{ME}.

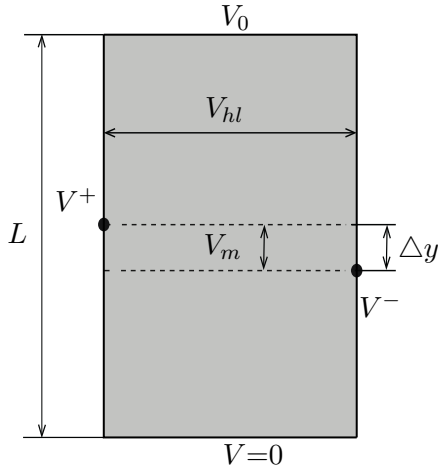

Figure 3.4: Representation of misalignment voltage V_m [33].

It should be noted that V_m varies with I_x but not with B_z [33]. If one measurement is taken and only V_{hl} and V_m are considered, the V_{ME} can be defined as:

$$V_{ME} = V^+ - V^- = V_{hl} + V_m \; ; \qquad V_m = \frac{V_0}{L} \triangle y \tag{3.5}$$

- **Righi-Leduc voltage** V_r: it is proportional to I_x but not to B_z. It is created by a different range of velocities at which electrons move generates again a T–gradient and as a consequence, transverse Seebeck voltage.

To sum up, the described voltages can be classified as:

1. V_e independent of I_x, B_z.
2. V_n, V_r that depends on B_z.
3. V_m that depends on I_x.
4. V_{hl}, V_e that depend on $I_x \times B_z$.

The main idea of AC/DC field methods is to eliminate the errors discussed above. This suppression can be reached by changing the applied I_x and B_z directions, more exact explanation is provided in the Subsection 3.3.1. It is important to emphasize that with I_x and B_z reversals all the errors except V_e are eliminated [28].

3.3.1 Direct Current (DC) field method

The theoretical approach of this method is related to the fact that real measurements always present offset voltages and can be expressed as [28]:

$$V_{ME} = V_s + V_e + V_n + \underbrace{f_d\,\rho\,I_x}_{V_m} + V_r + \underbrace{R\,I_x B_z}_{V_{hl}} = V^+ - V^- \tag{3.6}$$

where f_d is a dimensional factor that depends on the geometry of the sample, V^+, V^- are voltage measurements in contacts represented in the Figure 3.4.

Four measurements are required to separate V_{hl} from V_m and V_e. In each of them I_x can be applied in positive I_x^+ or negative I_x^- x–direction corresponding to electrical current reversal technique. In the same way for magnetic field reversal, positive B_z^+ and negative B_z^- z–directions are considered:

	I_x	B_z	V_s	V_e	V_n	V_m	V_r	V_{hl}
V_{ME_1}	I_x^+	B_z^+	+	+	+	+	+	+
V_{ME_2}	I_x^-	B_z^+	+	−	+	−	+	−
V_{ME_3}	I_x^+	B_z^-	+	−	−	+	−	−
V_{ME_4}	I_x^-	B_z^-	+	+	−	−	−	+

Table 3.2: Elimination of intrinsic errors from the measured Hall voltage by combining readings with different directions of a prescribed current and magnetic field [28].

After some mathematical operations, V_{hl} can be obtained:

$$\left.\begin{aligned} V_{ME_1} - V_{ME_2} &= 2\,(R\,I_x B_z + f_d\,\rho\,I_x) \\ V_{ME_4} - V_{ME_3} &= 2\,(R\,I_x B_z - f_d\,\rho\,I_x) \end{aligned}\right\} \quad \rightarrow \quad V_{hl} = R\,I_x B_z = \frac{V_{ME_1} - V_{ME_2} + V_{ME_4} - V_{ME_3}}{4} \tag{3.7}$$

- **The general formulations for the Hall bars**

The general formulations to measure R and $\rho(B_z)$ with the Hall bar and DC method is also provided by the ASTM standart F-76 [30]:

$$\left.\begin{aligned}\rho_a(B_z) &= \frac{V^+_{2,3}(B_z) - V^-_{2,3}(B_z) + V^+_{2,3}(-B_z) - V^-_{2,3}(-B_z)}{I^+_x(B_z) - I^-_x(B_z) + I^+_x(-B_z) - I^-_x(-B_z)}\frac{wt}{a}\\ \rho_b(B_z) &= \frac{V^+_{1,4}(B_z) - V^-_{1,4}(B_z) + V^+_{1,4}(-B_z) - V^-_{1,4}(-B_z)}{I^+_x(B_z) - I^-_x(B_z) + I^+_x(-B_z) - I^-_x(-B_z)}\frac{wt}{a}\end{aligned}\right\} \quad \rightarrow \quad \rho(B_z) = \frac{\rho_a + \rho_b}{2}$$

$$\left.\begin{aligned}R_a &= \frac{V^+_{3,4}(B_z) - V^-_{3,4}(B_z) + V^+_{3,4}(-B_z) - V^-_{3,4}(-B_z)}{I^+_x(B_z) - I^-_x(B_z) + I^+_x(-B_z) - I^-_x(-B_z)}\frac{t}{B_z}\\ R_b &= \frac{V^+_{2,1}(B_z) - V^-_{2,1}(B_z) + V^+_{2,1}(-B_z) - V^-_{2,1}(-B_z)}{I^+_x(B_z) - I^-_x(B_z) + I^+_x(-B_z) - I^-_x(-B_z)}\frac{t}{B_z}\end{aligned}\right\} \quad \rightarrow \quad R = \frac{R_a + R_b}{2} \tag{3.8}$$

where the sub-indices of V are the contacts' numbers for bars represented in the next subsections. As seen from the previous expressions, to calculate $\rho(B_z)$ and R, two equivalent measurements, sub-indices a, b are done; in that way isotropy of the sample for these two properties can be checked. If $\rho_a(B_z)$ and $\rho_b(B_z)$ are within 10%, $\rho(B_z)$ is considered identical in all directions of the sample; the same conclusion can be carried out with R. Nevertheless, an isotropy check can be done only on symmetrical samples, such as a regular four-contact and six-contact bars.

The following cases are studied applying $B_z = 1$ [T]. The I_x is created prescribing $V = 0$ [V] at 5 and $V = 1$ [V] at 6 for bars in the next subsections; with *FEAP* the value of I_x is taken from the reaction output on side 6. The meshes are descretized into a total of 4817 nodes for regular six-contact, 4959 nodes for eight-contact and 4783 nodes for irregular six-contact bars.

- **Six-contact Hall bar**

The V–distributions of cases with/without B_z can be observed in Figure 3.5.

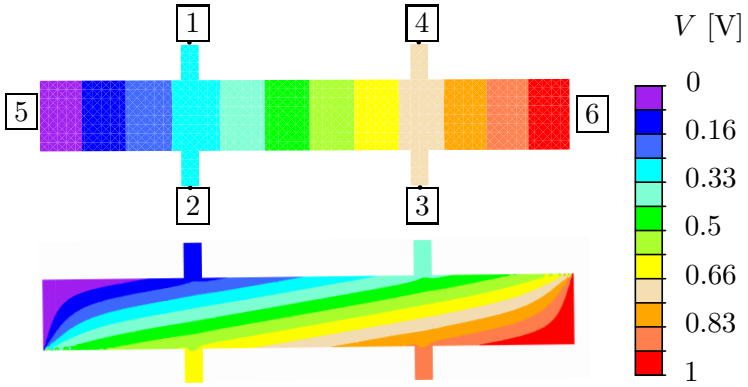

Figure 3.5: *FEAP* results of voltage distribution in a six-contact bar without (top) and with a prescribed magnetic field (bottom).

The small disturbance in the distributions at the right top and left bottom corners of the bottom figure is caused by the spin Hall effect; this phenomena consists on the spin accumulation of electrical current at the lateral sides due to B_z [34].

As stated before, the main disadvantage of this shape is the underestimation of R due to the close location of contacts to the end of the sample [30]. To verify this statement, $\triangle V_{3,4}$ outputs with B_z and I_x reversal are summarized in Table 3.3.

	I_x^+, B_z^+	I_x^-, B_z^+	I_x^-, B_z^-	I_x^+, B_z^-	I_x^+, B_z^+- I_x^-, B_z^+
$\triangle V_{3,4}$	-0.4736	0.4562	-0.4562	0.4736	0.0174
$\triangle V_{2,1}$	-0.4710	0.4585	-0.4585	0.4710	0.0125
I_x	0.7735	-0.7515	-0.7515	0.7735	

Table 3.3: Voltage difference between contacts and applied electric current in a six-contact Hall bar.

Since all the contacts are considered perfectly aligned mathematical points, it is verified $|\triangle V_{3,4}\ (I_x^+, B_z^+)| = |\triangle V_{3,4}\ (I_x^+, B_z^-)|$ and then $V_m = 0$ [V]. But, with the electrical current reversal at $\triangle V_{3,4}\ (I_x^+, B_z^+) \neq \triangle V_{3,4}\ (I_x^-, B_z^+)$ as a result of the error due to the proximity of the arms to the ends of the sample; the 0.0174 [V] and 0.0125 [V] errors are purely geometric.

In order to verify if misalignment errors can be observed with the B_z reversal, contact 4 was misaligned $m = a/2$ and $m = a$ with contact 3. As can be seen in Table 3.4:
$\triangle V_{3,4}\ (I_x^+, B_z^+) \neq \triangle V_{3,4}\ (I_x^+, B_z^-)$, difference that corresponds to the V_m contribution.

Misalignment	I_x^+, B_z^+	I_x^-, B_z^+	I_x^-, B_z^-	I_x^+, B_z^-	I_x^-, B_z^+ - I_x^-, B_z^-
$a/2$	-0.4773	0.4597	-0.4616	0.4793	0.0019
a	-0.4742	0.4567	-0.4551	0.4725	0.0016

Table 3.4: Voltage difference and applied electric current in a six-contact bar with misalignments $m = a/2$, $m = a$.

The final results are displayed in the Table 3.5. The errors of 1% in R and 3.65% in $\gamma(B_z)$ verify that the contact placement near the end reduces both absolute values.

	Data	Calculated	Error
R	-2.465×10^{-4}	-2.4381×10^{-4}	1%
$\gamma(B_z)$	2.45×10^4	2.4135×10^4	3.65%

Table 3.5: Results of the Hall coefficient and the magneto-resistance in a six-contact bar.

- **Eight-contact Hall bar**

This bar is considered a perfect shape for measurements and it is used to predict R with minimum error. Contacts 3 and 4 are located in the middle of the bar, sufficiently far-off the bar ends.

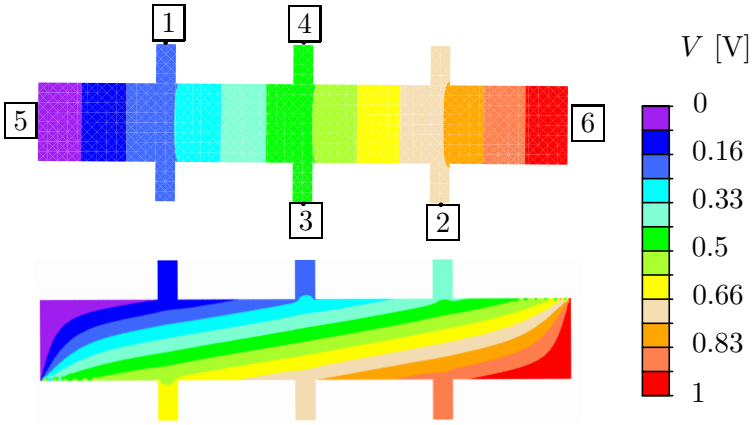

Figure 3.6: *FEAP* results of voltage distribution in an eight-contact bar without (top) and with an applied magnetic field (bottom).

As indicated in the table below $|\triangle V_{3,4}\ (I_x^+, B_z^+)| = |\triangle V_{3,4}\ (I_x^+, B_z^-)|$, then $V_m = 0$ [V]. Since contacts 3, 4 are placed exactly in the middle of the bar, it is also verified $|\triangle V_{3,4}\ (I_x^+, B_z^+)| = |\triangle V_{3,4}\ (I_x^-, B_z^+)|$.

	I_x^+, B_z^+	I_x^-, B_z^+	I_x^-, B_z^-	I_x^+, B_z^-
$\triangle V_{3,4}$	0.4958	-0.4958	0.4958	-0.4958
I_x	0.8103	-0.8103	-0.8103	0.8103

Table 3.6: Voltage difference between contacts and applied electric current in an eight-contact Hall bar.

In this shape, the R and $\gamma(B_z)$ estimations are done with one measurement and only the R_a and $\gamma_a(B_z)$ definitions from the Eqs. (3.8) are considered.

	Data	Calculated	Error
R_a	-2.465×10^{-4}	-2.4473×10^{-4}	0.71%
$\gamma_a(B_z)$	2.45×10^4	2.3841×10^4	2.68%

Table 3.7: Results of the Hall coefficient and the magneto-resistance in an eight-contact bar.

The eight-contact bar provides a perfect measurement of R_a with an error of 0.71%, while the error in $\gamma_a(B_z)$ is also reduced compared to the previous bar.

- **Irregular six-contact Hall bar**

This shape was proposed to take advantage of the middle placement of contacts 3 and 4 and at the same time permit an easier fabrication. The only drawback is that $\rho(B_z)$ cannot be estimated with an irregular bar, since a symmetrical sample is required.

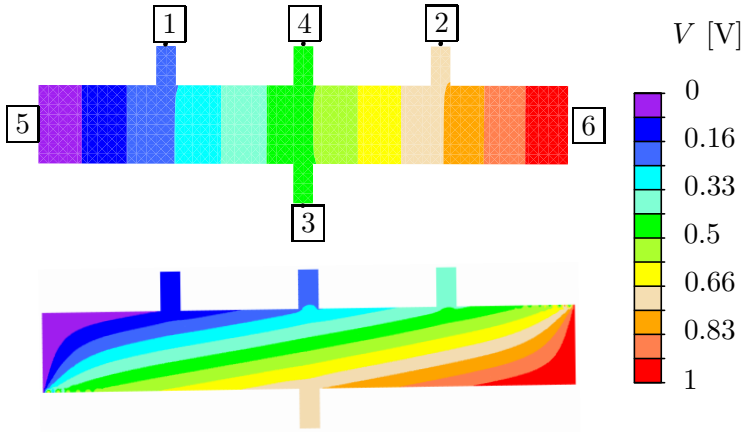

Figure 3.7: *FEAP* results of voltage distribution in an irregular six-contact bar without (top) and with an applied magnetic field (bottom).

The measurements are taken from perfectly aligned 3 and 4 contacts and as a result $V_m = 0$ [V] is observed during the electric current reversal:

	I_x^+, B_z^+	I_x^-, B_z^+	I_x^-, B_z^-	I_x^+, B_z^-
$\triangle V_{3,4}$	0.4946	−0.4949	0.4947	−0.4949
I_x	0.8089	−0.8089	−0.8089	0.8089

Table 3.8: Voltage difference between contacts and applied electric current in an irregular six-contact Hall bar.

As in the previous case, the parameters' estimation is done with only one measurement and considering the definitions of R_a and $\gamma_b(B_z)$ from the Eqs. (3.8). The R_a result reflected in the Table 3.9 reveals an error reduction compared to that of the regular six-contact bar, but it is still not as accurate as that of the eight-contact bar. The error in the $\gamma_b(B_z)$ estimation is about 38.8%, an improper result due to the sample's asymmetry.

	Data	Calculated	Error
R_a	-2.465×10^{-4}	-2.4472×10^{-4}	0.89%
$\gamma_b(B_z)$	2.45×10^4	4.76×10^4	38.3%

Table 3.9: Results of the Hall coefficient and the magneto-resistance in an irregular six-contact bar.

- **The general formulation for the Van der Pauw**

With this method, R can be calculated again with two equivalent a, b measurements and additional the isotropy of the sample can be checked [30]:

$$\left.\begin{aligned} R_a &= \frac{V^+_{4,2}(B_z) - V^-_{4,2}(B_z) + V^+_{4,2}(-B_z) - V^-_{4,2}(-B_z)}{I^+_{x_{3,1}}(B_z) - I^-_{x_{3,1}}(B_z) + I^+_{x_{3,1}}(-B_z) - I^-_{x_{3,1}}(-B_z)} \frac{t}{B_z} \\ R_b &= \frac{V^+_{1,3}(B_z) - V^-_{1,3}(B_z) + V^+_{1,3}(-B_z) - V^-_{1,3}(-B_z)}{I^+_{x_{4,2}}(B_z) - I^-_{x_{4,2}}(B_z) + I^+_{x_{4,2}}(-B_z) - I^-_{x_{4,2}}(-B_z)} \frac{t}{B_z} \end{aligned}\right\} \quad \rightarrow \quad R = \frac{R_a + R_b}{2} \tag{3.9}$$

where the sub-indices of V and I_x are the contacts' numbers for VdP shapes represented below. The following cases are studied applying the magnetic field $B_z = 1$ [T]. The $I_{x_{3,1}}$ is created prescribing $V = 0$ [V] at the point 1 and $V = 1$ [V] at the point 3. With $FEAP$ the value of $I_{x_{3,1}}$ is taken from the reaction output at 1 and the voltage difference $V_{4,2}$ is directly taken from the output of the second degree of freedom. The square shape is discretized into a total of 51105 nodes and the circular one into 14228 nodes. The main idea is to compare the influence in the R estimation of contact placement at the corners or along the periphery of the shape [30]. Theoretically, it is considered that R can be accurately measured only if contacts are placed at the corners.

The V–distribution for both geometries with $B_z = 0$ [T] and $B_z = 1$ [T] are displayed. As can be observed in the square shape, four contacts are placed at the corners while in the circle one they are at the vertical and horizontal axes of symmetry on the periphery.

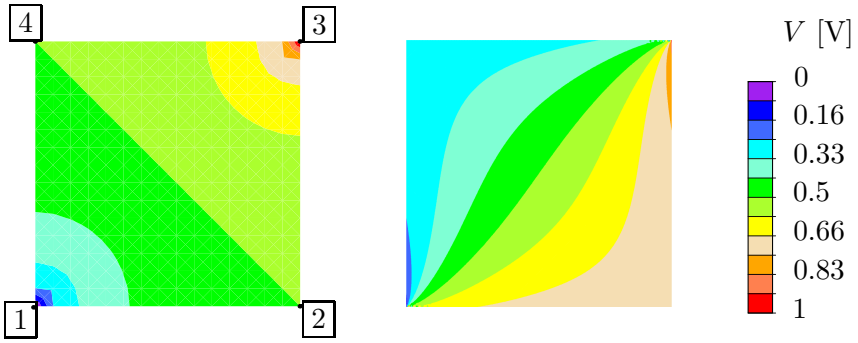

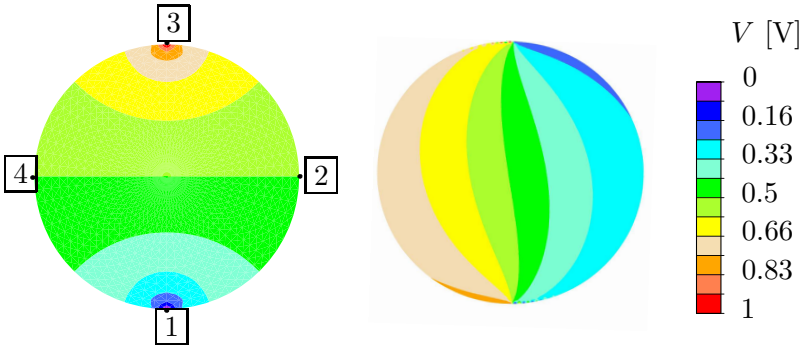

Figure 3.8: *FEAP* results of voltage distribution in square and circular shapes without (left) and with an applied magnetic field (right).

No misalignment was introduced to provide results focused on the influence in R of the contact placement. Since exactly equal V and I outputs from the a, b experiments were obtained for each shape, only $\triangle V_{4,2}$ and $I_{x_{3,1}}$ values are summarized:

		I_x^+, B_z^+	I_x^-, B_z^+	I_x^-, B_z^-	I_x^+, B_z^-
Circular	$\triangle V_{4,2}$	0.6441	-0.644	0.6441	-0.644
shape	$I_{x_{3,1}}$	1.112	-1.112	-1.112	1.112
Square	$\triangle V_{4,2}$	0.477	-0.477	0.477	-0.477
shape	$I_{x_{3,1}}$	0.7753	-0.7753	-0.7753	0.7753

Table 3.10: Voltage difference between contacts and applied electric current in square and circular shapes.

As reflected in the Table 3.11, the contact placement at the corners of a symmetrical sample provides an error of 0.08%. This result is the most precise compared to all the measurements done before. The circular shape error for R is about of 6%, which is six times greater than in the Hall's bars and 75 times greater than in the square shape. The conclusion that can be carried out is that at the corners the spin Hall effect is suppressed. But, if the contacts are placed along the circular periphery, this effect and the error in the measurements are enlarged.

		Data	Calculated	Error
Circular shape	R	-2.465×10^4	-2.316×10^4	6%
Square shape	R	-2.465×10^4	-2.463×10^4	0.08%

Table 3.11: Results of the Hall coefficient in square and circular shapes.

3.3.2 Alternate Current (AC) field method

This technique is commonly used to eliminate V_m, the source of the largest intrinsic error in R. In a real measurement $V_m = 0$ [V] only if the voltage contacts are mathematical points placed at the corners and the geometry is a perfect square. Any change in shape or contact placement results in non-zero V_m.

The AC method consists in prescribing a sinusoidal B_z signal, and as a consequence V_{hl} becomes time-dependent. Considering only large voltage contributions from the definition of V_{ME} from the Eq. (3.6):

$$V_{ME} = \underbrace{RI_xB_z\cos(\omega\tau) - \beta B_z\,\omega\sin(\omega\tau)}_{AC\ voltage} + \underbrace{\alpha\rho I_x + V_s}_{DC\ voltage} \tag{3.10}$$

where β is the inductance of the sample and ω is the angular velocity and τ is time.

As seen from the Eq. (3.10), V_{ME} is subdivided into AC and DC voltage. The DC contribution can be easily removed using in the experiment a lock-in amplifier (LIA), that separates both voltages and maintains only the desired AC signal [30]:

$$V_{ME} = \underbrace{RI_xB_z\cos(\omega\tau)}_{Hall\ voltage} - \underbrace{\beta B_z\,\omega\sin(\omega\tau)}_{Inductive\ pickup} \tag{3.11}$$

The final AC voltage is decomposed into V_{hl} and an inductive pickup. The V_{hl} is in phase with the B_z signal, while the inductive pickup is 90° out of phase and can be removed using the electric current reversal:

$$\begin{aligned} V_{ME}(I_x^+) &= RI_xB_z\cos(\omega\tau) - \beta B_z\,\omega\sin(\omega\tau) \\ V_{ME}(I_x^-) &= -RI_xB_z\cos(\omega\tau) - \beta B_z\,\omega\sin(\omega\tau) \end{aligned} \tag{3.12}$$

The $FEAP$ cases are simulated with the regular six-contact bar and the circular VdP shape with prescribed sinusoidal B_z. Typically, the frequency of B_z is from 0.1 [Hz] to 0.2 [Hz] and then $\omega = 1$ [rad/s] was chosen [30]. To separate the AC and DC signals from the $FEAP$ V_{ME} output, a block DC component offset from an input signal *dsp.DCBlocker* System from $MathWorks^{®}$ was used [42]. The same result can be obtained by applying the discrete Fourier transform [43], [44]:

$$F_k = \sum_{j=0}^{N-1} x_j w_t^{k,j}\ ; \qquad F_0 = \sum_{j=0}^{N-1} x_j \tag{3.13}$$

where w_t is the twiddle factor (any of the trigonometric coefficients that are multiplied by the data in the discrete Fourier transform), x_j is the V_{ME} signal and F_0 is a zero frequency signal.

An amplitude without frequency F_0 corresponds to the DC signal, and as a consequence subtracting F_0 from the V_{ME} output, V_{hl} can be obtained.

- **The six-contact Hall bar**

As stated before, the Hall bar is considered an ideal shape for the R measurement. The accuracy is reached by the extended arms that minimize misalignment errors, as the contacts placement is restricted to the arms ends of width a. In that way, contact misalignments can vary a small range [0, a]. To verify this statement, measurements of R with the six-contact bar, characterized by the same number of nodes and dimensions as in the previous case, are performed with misalignments of $m = 0$, $m = a/2$, $m = a$.

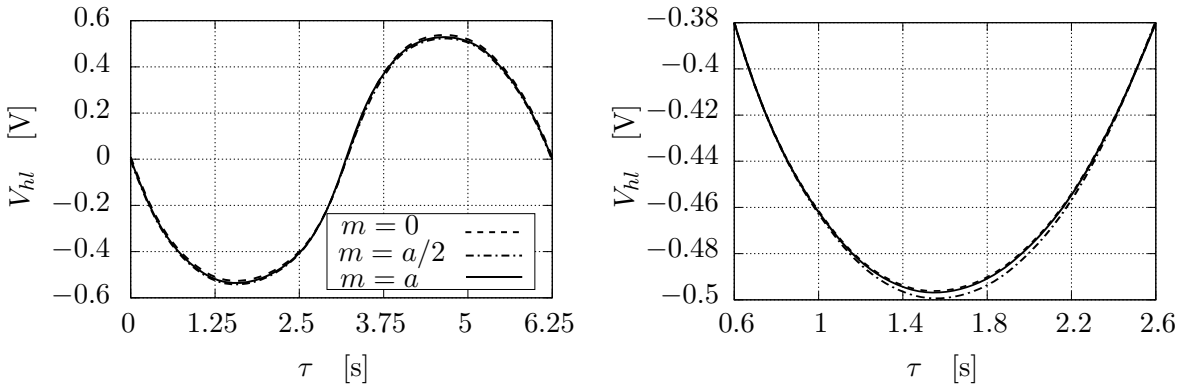

Figure 3.9: *FEAP* results of Hall voltage in a regular six-contact bar after applying an alternate current magnetic field. Measurements done with contact misalignments $m = 0$, $m = a/2$, $m = a$.

In the Figure 3.9 the V_{hl} sinusoidal outputs for three different misalignments are displayed. The amplitude of the sinusoidal signal corresponds to the V_{hl} value. Even on a zoom of the left figure, Figure 3.9 right, the difference in the amplitude for the three cases is minimal.

Misalignment [m]	Amplitude [V]	V_m [V]	V_m/ V_{hl} [%]
$m = 0$	-0.4958	0	0
$m = a/2$	-0.4997	0.0002	0.78
$m = a$	-0.4964	0.0005	0.12

Table 3.12: Comparison of Hall's voltage amplitude, misalignment voltage and error in the six-contact bar with several contact misalignments.

As summarized in the Table 3.12 the maximum error introduced by contact misalignment is

0.8%, verifying that a small range of a contact placement leads to a minimal undesired V_m.

- **The circular Van der Pauw geometry**

In the Hall bars, the contact placement is restricted to a small width of the extended arms, while in the VdP geometry contacts can be placed at any point along the contour of the shape. Misalignment is the most common error in VdP measurements. To get an idea of the error percentage that the produced V_m can create, three measurements are performed with the circular shape with contact misalignments of $m = 0$, $m = b/2$, $m = b$, where $b = 9.5 \times 10^{-3}$ [m]. The number of nodes and dimensions are as in the Figure 3.8.

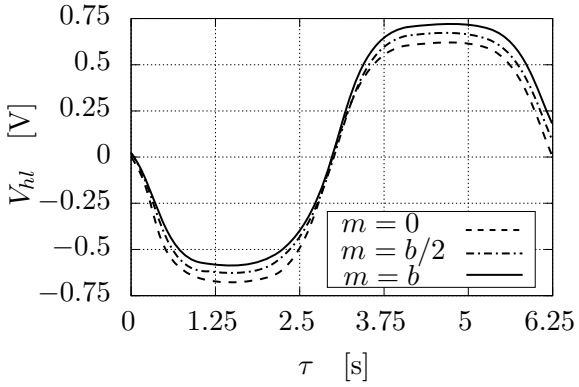

Figure 3.10: *FEAP* results of Hall's voltage in a circular shape after applying alternate current magnetic field. Measurements done with contact misalignments $m = 0$, $m = b/2$, $m = b$.

As seen in the Figure 3.10, at $\tau = 0$ [s] and $\tau = 6.25$ [s] (the start and the end of a signal's cycle) the V_{hl} change in value drastically, variation that corresponds to the V_m contribution. Taking into account the results summarized in Table 3.13, it can be concluded that incorrect alignment can produce a maximum of 19% error into the V_{hl} amplitude.

Misalignment [m]	V_{hl} [V]	V_m [V]	$V_m/\ V_{hl}$ [%]
$m = 0$	-0.6441	0	0
$m = b/2$	-0.6088	0.021	5.48
$m = b$	-0.5194	0.0716	19

Table 3.13: Comparison of Hall's voltage amplitude V_{hl}, misalignment voltage and error in the circular shape with contact misalignments $m = 0$, $m = b/2$, $m = b$.

3.4 Parametric studies

3.4.1 Influence of magnetic field on thermoelectric properties

Commonly, the Hall effect measurements are done prescribing a low B_z, as in a such condition the TE properties ρ, κ of a semiconductor are similar to the case without magnetic field. The idea of the impact of high B_z on the TE properties was developed in [32], and to determine the threshold B_z value, the VdP technique is going to be used with the square shape for the range [0, 5] [T].

For the κ estimation using the VdP technique, a heat flow $Q_{1,2}$ is prescribed to node 1 and 2, and a T–gradient $T_{4,3}$ is measured at the other two contacts see Figure 3.8; for the ρ estimation, a similar approach is carried out applying $I_{1,2}$ and measuring $V_{4,3}$. Once these two tests are done, identical BCs are prescribed to nodes 2 and 3, obtaining $T_{1,4}$ or $V_{1,4}$. The VdP formulations for all these tests from [30] is:

$$
\begin{aligned}
&RE_1 = \frac{V^+_{4,3} - V^-_{4,3}}{I^+_{1,2} - I^-_{1,2}} = \frac{T^+_{4,3} - T^-_{4,3}}{Q^+_{1,2} - Q^-_{1,2}} \; ; \qquad RE_2 = \frac{V^+_{1,4} - V^-_{1,4}}{I^+_{2,3} - I^-_{2,3}} = \frac{T^+_{1,4} - T^-_{1,4}}{Q^+_{2,3} - Q^-_{2,3}} \; ; \\
&g = \frac{RE_1}{RE_2} \; ; \qquad \cosh\left[\left(\frac{g-1}{g+1}\right)\frac{\ln(2)}{f_a}\right] = \frac{1}{2}\exp\left(\frac{\ln(2)}{f_a}\right) \; ; \\
&\rho = \frac{\pi f_a t}{\ln(2)}\frac{RE_1 + RE_2}{2} \; ; \qquad \kappa = \frac{\pi f_a t}{\ln(2)}\frac{RE_1 + RE_2}{2}
\end{aligned}
\tag{3.14}
$$

where RE_1, RE_2 are the measured resistances, g is the resistance ratio and f_a a geometrical factor to be numerically obtained from the fourth equation. For the ρ estimation, RE_1, RE_2 are calculated with V and I values, while for κ with T and Q values.

In $FEAP$ and for the electric field, instead of applying I directly to the node, $V = 0$ [V] at the contact 1 and $V = 1$ [V] at the contact 2 are prescribed; the value of $I_{1,2}$ is taken from the reaction output in the contact 2. The same approach is followed for the thermal field.

As seen in the Figure 3.11 right, in a range from 0 [T] to 2 [T] the difference between $\rho(B_z)$, $\kappa(B_z)$ and their values when $B_z = 0$ [T] is below 1%. The largest percentage difference for $\rho(B_z)$ is reached at 5 [T] with a maximum of 60%, while for $\kappa(B_z)$ the applied B_z affects slightly. It can be concluded that for $B_z > 2$ [T], $\rho(B_z)$, $\kappa(B_z)$ should be considered as B_z functions.

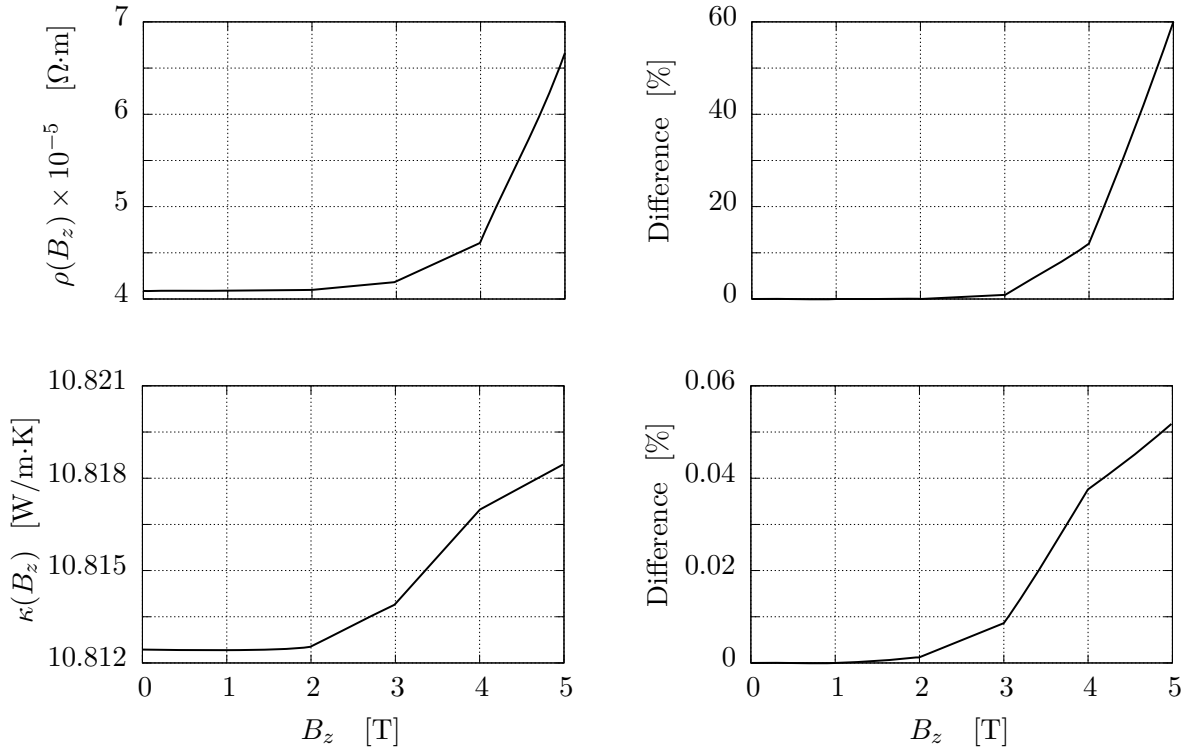

Figure 3.11: *FEAP* results of electrical resistivity and thermal conductivity obtained with the Van der Pauw method in a square applying magnetic field from 0 to 5 [T].

3.4.2 Effects of the thin-film thickness on resistivity measurements

Most of the past investigations are focused in shape, contact size or placement effects on the accuracy of the VdP measurements. The effect of sample thickness was recently investigated in [31]. The requirement of a thin-film sample comes from the VdP formulation, which was developed for a completely 2D electrical/heat current distributions. An experimental study developed in [31] on graphite concluded that the accuracy of this method is highly improved by making the films sufficiently thin. The experimental results showing the constant value only for $t < 2 \times 10^{-3}$ [m] can be observed in the Figure 3.12.

As stated before, for the *FEAP* simulations a semiconductor film is simulated with $elmt12.f$ witch incorporates 2D galvanomagnetic formulation; the film thickness is introduced as a material property. The main idea is to verify if the ρ evolution seen in the Figure 3.12 is only due to 3D interactions or if any anomalous 2D effect can be observed. For this purpose the VdP method was applied to the square shape, varying the sample's thickness.

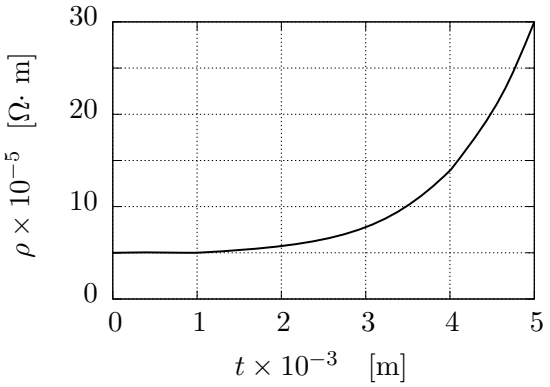

Figure 3.12: Measurements of resistivity by Van der Pauw method on graphite material with different thikness [31].

From the results contained in the Table 3.14, it is observed that ρ does not change with thickness in a sample. The conclusion that can be carried out is that if 2D symmetry in the electrical/heat current distribution is maintained across the sample, the VdP method calculations are highly precise.

Thickness [m]	1×10^{-4}	1×10^{-3}	1×10^{-2}
$\rho \times 10^{-5}$ [Ω· m]	4.18	4.18	4.18

Table 3.14: Measurement of resistivity with Van der Pauw method on square of different thickness.

4

Simulation of Lithography-free resistance thermometry

In this chapter, a new technique for measuring the Seebeck $\alpha(T)$ and the Hall $R(T)$ coefficients as function of temperature, developed by the Institute of Materials Research and Engineering of Singapore [20] is reviewed. This technique can be applied to thin films of large dimension and provide more accurate $\alpha(T)$ estimation than common 2-probe and 4-probe techniques only useful for miniature films. This new method has a strong potential and it is expected to be widely adopted for the TE materials' characterization; for that reason it was selected for the study.

In the following sections a brief research motivation is presented and results of $\alpha(T)$ and $R(T)$ from the outputs of $FEAP$ are provided. The main idea is to test the method and perform an analysis of the obtained results.

4.1 Motivation

Currently, two dominant setups are used to measure α: 2-probe and 4-probe methods, both susceptible to errors. As represented in the Figure 4.1 left, in the 2-probe configuration, a TE material is placed between two metal block, one acting as a heater and the other as a sink. The T–measurements are taken from thermocouples, embedded in the metal blocks. This T–measurements can be overestimated as one of the thermocouples is in direct contact with the heater, called hot finger effect. The other drawback is the thermal contact resistance between the sample and the heat source/sink: a poor contact connection between both can cause a large offset in the T–measurements [38].

This thermal contact resistance can be avoided with the 4-probe configuration, see Figure 4.1 right, as thermocouples are placed along the side of the sample. However, some new issues such as the cold-finger effect and the point contact resistance appear at high temperatures. The former effect, is the result of heat transfer from the sample to the thermocouples, leading to an underestimation of the T–measurements. The latter effect is related to the contacts: to ensure a good connection between the thermocouple and the sample's surface, a pressed union between both is required. In soft organic TE materials this loading is the cause of sample's breakage or plastic deformation. To settle the loading problem, low forces can be used, however, this leads

to a high thermal resistance between the thermocouple and the sample.

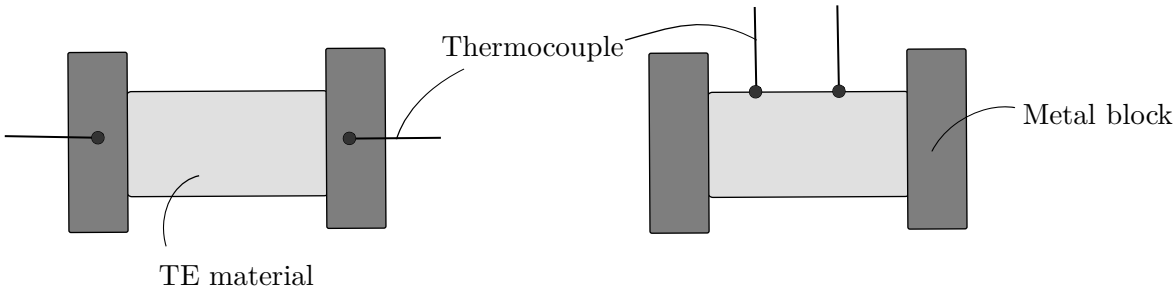

Figure 4.1: Representation of 2-probe (left) and 4-probe (right) methods for Seebeck coefficient measurements [38].

4.2 Method's configuration

4.2.1 Measurement device configuration

The new lithography-free resistance technique, which is thermometry based provides the $\alpha(T)$ and $\gamma(T)$ estimations for large area films. The thermal resistance issue mentioned is solved by pre-pattering the electrodes to the sample using a low-cost shadow mask. Shadow masks represented in the Figure 4.2(a) are an important tool to make metal thin films with hole pattern cut on them; the pattern determines the areas of the substrate that will be coated with metal [41]. This is a one-step process to fabricate high-quality electrodes, sensors and heating wires in microelectronic devices.

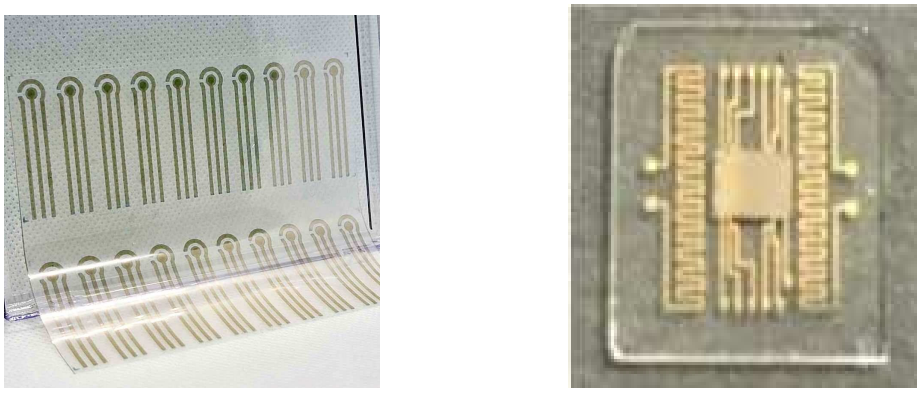

(a) (b)

Figure 4.2: Representation of (a) Gold flexible shadow mask [41]; (b) a real laboratory device for the Seebeck effect measurements [20].

These masks are deposited on the material to be studied with thickness $t = 7 \times 10^{-8}$ [m]; then this material is deposited on a substrate of thickness $t_s = 1 \times 10^{-2}$ [m] as represented in the Figure 3.2(b). The measurement device is seen in the Figures 4.2(b), 4.3 and contains a shadow mask with patterned heater, two thermometers and two electrodes for electrical resistivity measurements. All elements are gold lines that provide a large contact area with the material. There are some geometrical requirements for the placement of these lines: the distance of 2×10^{-3} [m] between thermometers and electrodes, the 1×10^{-3} [m] between two thermometers to achieve a large T–gradient, and the 2×10^{-3} [m] between the heater and the first electrode are required.

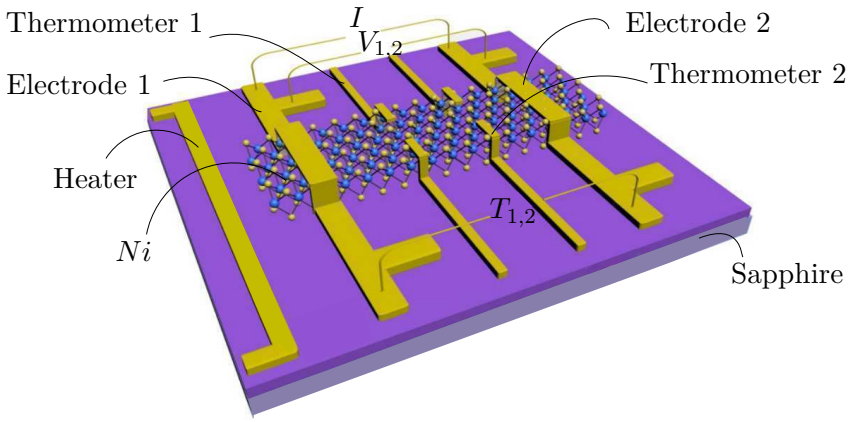

Figure 4.3: Schematic representation of the setup for the Seebeck coefficient measurements [38].

4.2.2 Material

The material to be studied in this chapter is Niquel Ni, the properties of which are are expressed in the Eqs. (4.1) [20]; their graphical evolution compared with the $FEAP$ results can be found in the following subsections.

$$\begin{aligned} \kappa(T) &= 10 - 3.33 \times 10^{-2}\ T \\ \gamma(T) &= 8.99 \times 10^{6} - 1.51 \times 10^{4}\ T \\ \alpha(T) &= 8.35 \times 10^{-4} - 5 \times 10^{-4}\ T \end{aligned} \tag{4.1}$$

The properties of Sapphire (Eqs. (4.2)) are assumed constant and evaluated at $T_m = 300$ [K], [36]. As mentioned before the heater, electrodes and thermometers are made of Gold Au, also with very high κ and γ.

- Saphire:

$$\kappa(T_m) = 53; \qquad \gamma(T_m) = 2 \times 10^{-15}; \tag{4.2}$$

- Gold:

$$\kappa(T) = 332 - 4.52 \times 10^{-2}\ T$$

$$\gamma(T) = 2.33 \times 10^{8} - 9.98 \times 10^{5}\ T + 1073\ T^2 \tag{4.3}$$

$$R(T) = 6.16 + 2.43 \times 10^{-2}\ T$$

The graphical representations of $\kappa(T), \gamma(T), R(T)$ from Eqs. (4.3) are [37]:

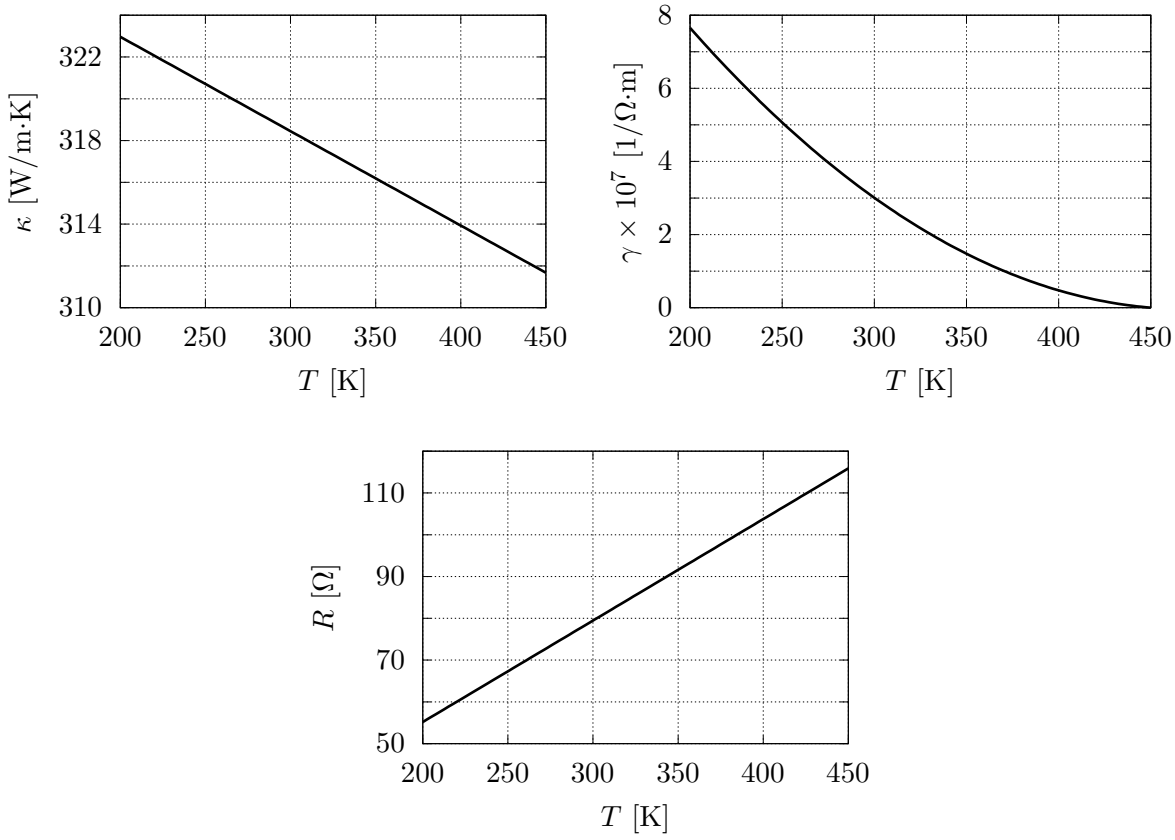

Figure 4.4: Evolution of the resistance, thermal and electrical conductivities with temperature for Gold material [37].

4.2.3 Elements and the mesh discretization

For the *FEAP* cases, Gold and Niquel materials along with rectangular 2D elements of *elmt*12.*f* with coupled GM properties are used. In turn, for Sapphire rectangular 3D elements

of $elmt11.f$ with uncoupled thermal and electrical conduction formulation are used.

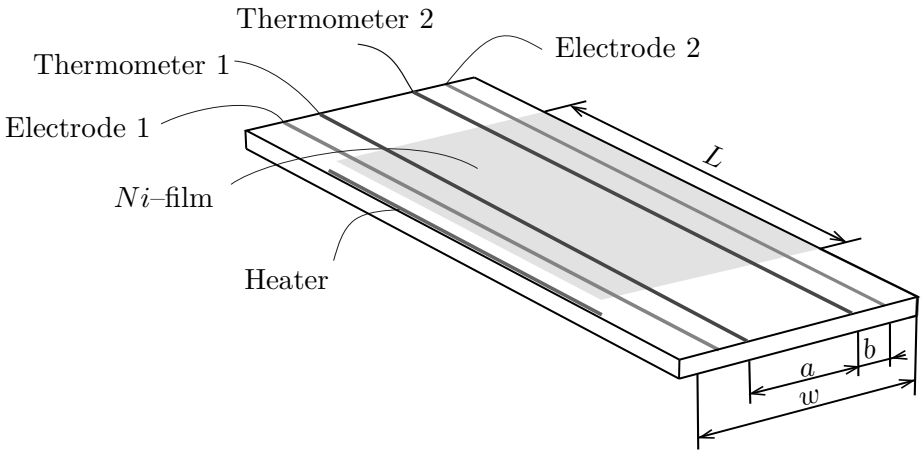

Figure 4.5: Representation of the $FEAP$ mesh for the Seebeck coefficient measurements.

The $FEAP$ mesh, which configuration is pictured in the Figure 4.5, is discretized into a total of 14241 nodes. The device's dimensions are similar to those listed in [20] and are summarized in the Table 4.2:

Parameter	Value	Units
a	1×10^{-3}	[m]
b	0.3×10^{-3}	[m]

Parameter	Value	Units
w	0.6×10^{-2}	[m]
L	0.3×10^{-2}	[m]

Table 4.1: Dimensions for the Seebeck measurement setup represented in Figure 4.5, [20].

4.3 Results

4.3.1 Electrical conductivity estimation

To perform the $\rho(T)$ measurements, an electric current I is prescribed through the sample's width and the resistivity voltage is read between the electrodes 1 and 2. With $FEAP$, to prescribe I the right side of Ni is maintained at V_{right} and the left side at V=0 [V]; then the value is taken from the reaction output. The base of the substrate is maintained at constant T, then $\rho(T)$ at this temperature is estimated. From [20] the expression of $\rho(T)$ is:

$$\rho(T) = \frac{\mathrm{d}V}{\mathrm{d}I}\frac{A}{L} = \frac{\mathrm{d}V}{\mathrm{d}I}\frac{w\,t}{L} \tag{4.4}$$

where A is the cross-section area of the film.

As seen from the Eq. (4.4), $\rho(T)$ is a $\mathrm{d}V/\mathrm{d}I$ function; to calculate this slope, several measurements varying the value of I are done. The prescribed V_{right} of $FEAP$ were: 0.06, 0.02, 0.001 [V], values that created 4.46 $\times 10^{-4}$, 5.6 $\times 10^{-5}$, 1.7 $\times 10^{-5}$ [A] respectively.

Another aspect that needs to be controlled is the temperature of the film. A uniform T along the electrodes width needs to be maintained to assure precise V–measurements. As seen from the Figure 4.6, when the smallest V–gradient is prescribed (I =1.7 $\times 10^{-5}$ [A]), the T along the electrodes is almost constant.

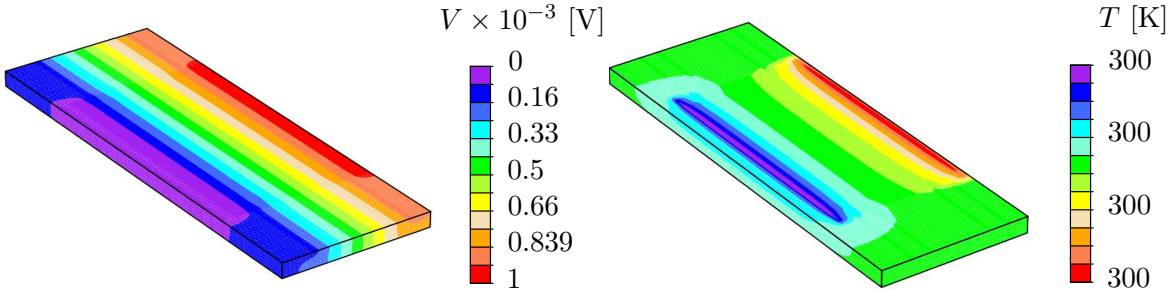

Figure 4.6: $FEAP$ results of voltage (left) and temperature (right) under prescribed electric current of 1.7 $\times 10^{-5}$ [A].

The measurements are repeated for increased V–gradients. As seen from the Figure 4.7 left, under I=5.6 $\times 10^{-5}$ [A] the T–distribution becomes irregular, although the T–variations in the film are still negligible. Nevertheless, under I=4.46 $\times 10^{-4}$ [A] of the Figure 4.7 right, a Joule heating is observed: the 5 [K] increment in the T–distribution will lead to spurious measurements. It can be concluded that for an accurate $\rho(T)$ estimation, values below 1 $\times 10^{-4}$ [A] need to be considered.

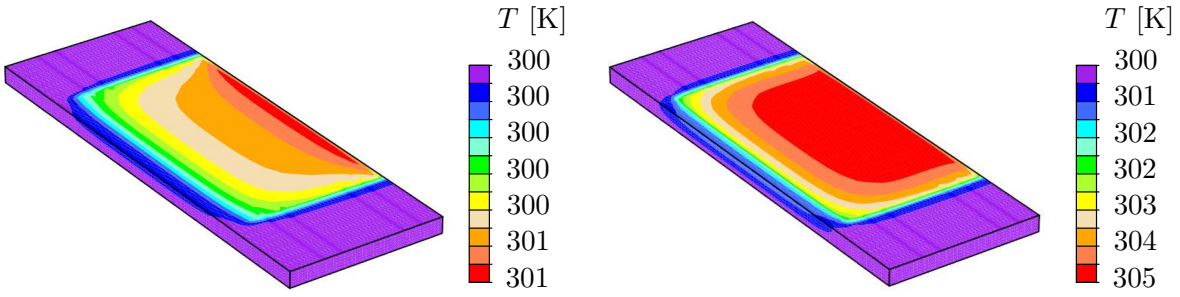

Figure 4.7: $FEAP$ results of temperature distributions with prescribed electric current of 5.6 $\times 10^{-5}$ [A] (left) and 4.46 $\times 10^{-4}$ [A] (right).

In the Figure 4.8, $\gamma(T)$ results from $FEAP$, from laboratory measurements of [20] and

from others of [39] are compared. In the first two results, a thickness of 7×10^{-8} [m] has been considered while for the third 4×10^{-8} [m] has been estimated. The results of the three studies fit almost perfectly. The small difference can be caused by the non-consideration of the convection factor in the estimation or the instruments' calibration. In addition, it can be seen that the γ value for 4×10^{-8} [m] is greater than for 7×10^{-8} [m]. The same conclusion as in the Subsection 1.4.2 can be carried out: the quantum confinement effect such as the reduction of the film's thickness increases γ and therefore enhances ZT.

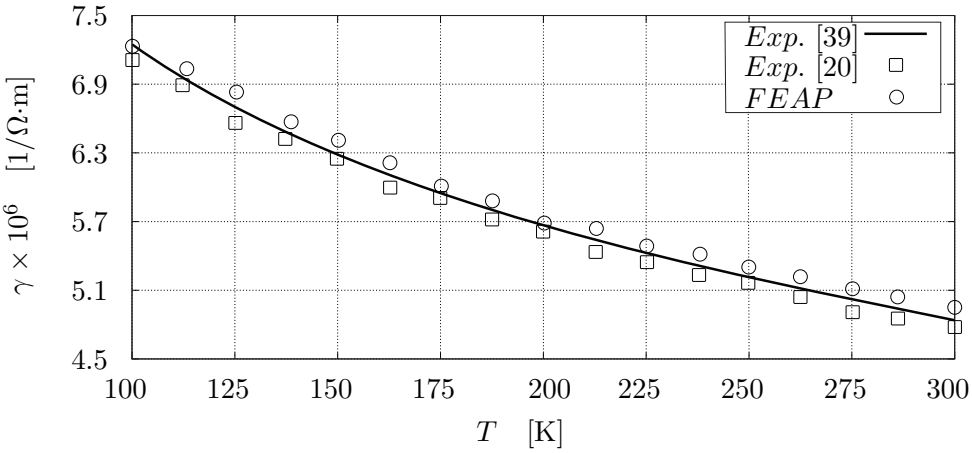

Figure 4.8: Results of electrical conductivity under different temperatures from $FEAP$ and experimental results from [20] and [39].

4.3.2 Seebeck coefficient estimation

In this test, during the measurements the base of the substrate and the heater are maintained at different temperatures. The heater creates a small T–gradient across the film, necessary to measure $\alpha(T)$. In that way, experiments are preformed changing the substrate's T to make a reconstruction of $\alpha(T)$, always maintaining the difference between the substrate and the heater of 15 [K]. The $\triangle V_{1,2}$ and $\triangle T_{1,2}$ values are read between the thermometers 1 and 2. The formulation for $\alpha(T)$ from [20] is:

$$\alpha(T) = \frac{\triangle V_{1,2}}{\triangle T_{1,2}} \tag{4.5}$$

Additionally, the heater is covered with a Kapton tape. This tape is necessary to avoid an electrical shorting between the heater and the film, and to evade spurious voltage measurements caused by conduction between both. With $FEAP$, $V = 0$ [V] was prescribed in the heater, to simulate this tape.

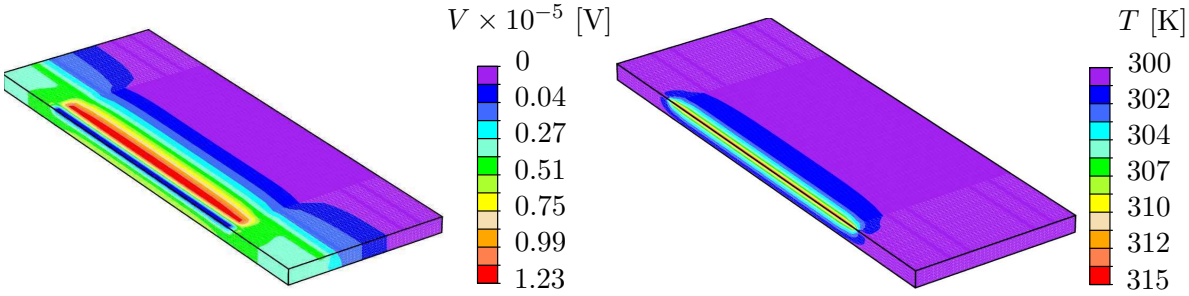

Figure 4.9: *FEAP* results of voltage (left) and temperature (right) distribution with prescribed flux in the heater.

The V and T distributions are represented in the Figure 4.9. It should be noted that the V–values are very low, making difficult to achieve precise measurements. In a real experiment sophisticated nanovoltmeters should be used to capture this small V–difference across the sample.

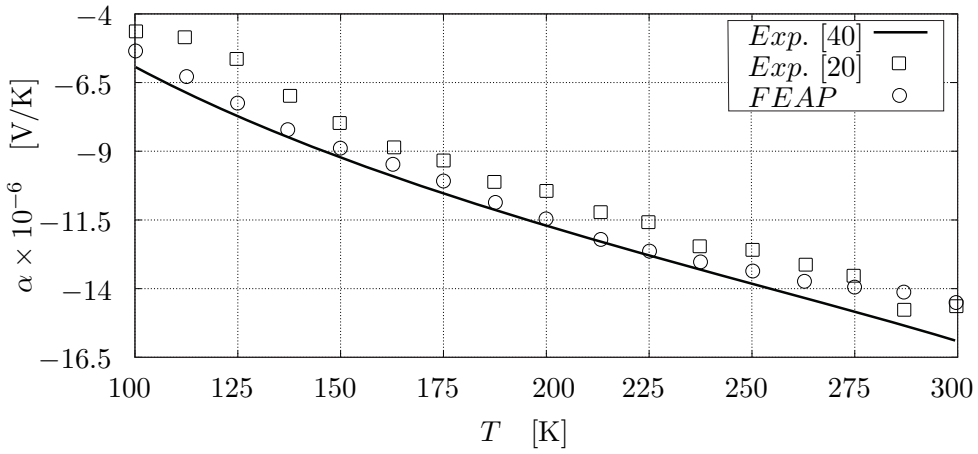

Figure 4.10: Results of the Seebeck coefficient under different temperatures from *FEAP* and experimental results from [20] and [40].

In the Figure 4.10, $\alpha(T)$ results from *FEAP*, from laboratory measurements of [20] and from [40] are compared. In the first two, experiments are performed with thin-films while in the third with a nanowire. With these results, comparison between the properties of both quantum films and quantum wires can be done. As reviewed in the Subsection 1.4.2 the objective of both techniques is to enhance ZT, increase that can be done by α increment or κ reduction. Although the $\alpha(T)$ results are similar, it should be noted that in wires this property is greater than in films. However no conclusions can be carried out on ZT, because additional studies on κ should

be considered.

4.3.3 Hall coefficient estimation

The Hall and the Seebeck coefficients are both functions of the carrier concentration n of the studied material. By finding n from the Mott formulation of α for transition metals (Eqs. (4.6) left), and substituting it into the Eqs. (4.6) right, the $R(T)$ can be calculated varying the substrate's T.

$$\alpha = \frac{2\pi^2\, m_i\, k_b^2\, T}{3\, h_p^2\, e} \sqrt[3]{\left(\frac{8\pi}{3n}\right)^2}\,; \qquad R = \frac{1}{n\, e} \tag{4.6}$$

where m_i is the free electron mass, k_b the Boltzmann's constant, h_p the Planck's constant and e is the electron's charge. The values of all the coefficients necessary are:

Parameter	**Value**	**Units**
m_i	9.11×10^{-31}	[kg]
k_b	1.38×10^{-23}	[J/K]

Parameter	**Value**	**Units**
h_p	1.054×10^{-34}	[J ·m]
e	1.6×10^{-19}	[C]

Table 4.2: Values of coefficients for estimation of the sample's carrier concentration.

In the Table 4.3, n results obtained from $\alpha(T)$ taken from the $FEAP$ simulation and n results from R measurements [20] are presented. Some difference between results is observed, but the decreasing evolution of n with T is maintained in both. Although a significant maximum of 19% of error is obtained, the calculation of n from the Mott's formulation can reduce the amount of measurements and devices' configurations for material characterization, since from α measurements n and therefore R can be calculated.

n [m^{-3}]	100 [K]	150 [K]	200 [K]	250 [K]	300 [K]
R	2.54×10^{29}	2.48×10^{29}	2.34×10^{29}	2.31×10^{29}	2.21×10^{29}
$FEAP$	2.035×10^{29}	2.019×10^{29}	2.012×10^{29}	2.0078×10^{29}	2.0048×10^{29}
Difference	19 %	18 %	14 %	13 %	9 %

Table 4.3: $FEAP$ and experimental results of the sample's carrier concentration.

In the Figure 4.11 three different distributions of R are compared. In the first, the R measurement is done with one of the techniques described in the Chapter 3 while in the last two

R is obtained calculating n with Mott's formulation from the α results of Figure 4.10. The distributions of the last two studies fit almost perfectly since their α values from the Figure 4.10 are similar. The difference of R comes from that of n from the Table 4.3.

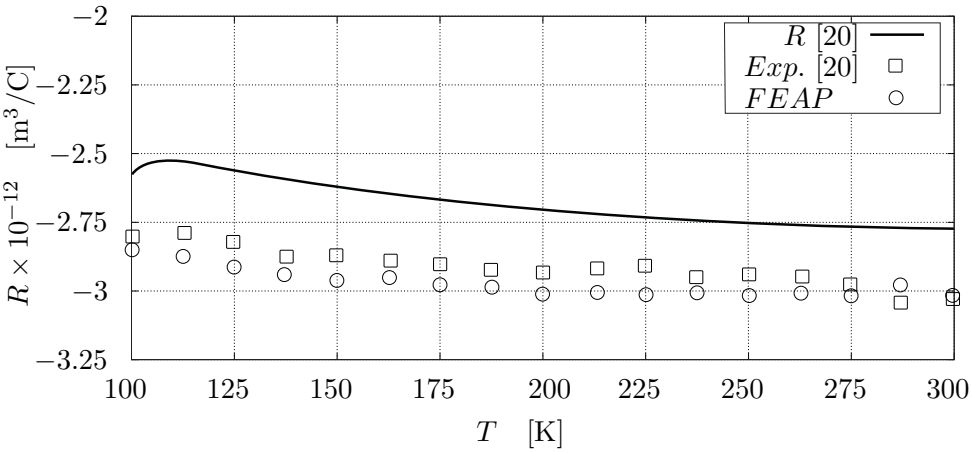

Figure 4.11: Results of the Hall coefficient under different temperatures with $FEAP$ and [20] calculations with Mott's formulation, and with experimental results from [20].

5

Conclusions

In this work, methods of characterization of thermoelectric thin films are reviewed. The necessity of measuring properties on thin films deposited on a substrate is essential to capture the effect of the quantum confinement. Another important aspect is that the reduced thickness suppresses the 3D interactions making possible the calculation of the parameters with a 2D formulation.

Prior to the study of the material characterization, validation of the galvanomagnetic effect is carried out by comparing the FDM and the FEM results from the $FEAP$ program. Once the validity of the $FEAP$ results was completed the usual methods for Hall coefficient and electrical resistivity estimation were simulated. The AC/DC methods described from ASTM protocol were applied to the Hall bars and VdP geometries. This study was completed with an innovating Hall bar shape from the Lake Shore's Laboratory. A comparison of results obtained with these geometries is provided along with the analysis of the pros/cons of the proposed Lake Shore's shape. Finally, an experiment from recent research technique for Seebeck and Hall coefficients estimation was repeated with $FEAP$ simulation. The experimental laboratory results were compared with those of $FEAP$, showing that FEM is an accurate tool to make experimental predictions.

The conclusions that can be carried out from the study are:

- The prescription of the magnetic field can improve the performance of thermoelectric materials. The applied 1D current/heat flux, under magnetic field becomes 2D.
- It is very important to develop simple methods for measuring thermoelectric properties, where the measured properties are not affected by the device configuration.
- The special elements of $FEAP$ allow to simulate any phenomenon with known mathematical model. For that reason, a prior validation of $FEAP$ results with analytical solution is required.
- The cases simulated with $FEAP$ allow to analyze the factors that affect the measurements and create a configuration that minimizes errors.
- The material selection for elements such as substrate, electrode or thermometers of the measurement device is important as they can affect the measurements.

- It is important to maintain the device at fixed temperature as far as possible as thermoelectric properties are temperature functions.
- In the Hall's coefficient measurement, a large error can be introduced by the spin Hall effect. This effect is minimized in the square shapes and maximized in the circular shapes.
- Misalignment of the voltage contacts can create a spurious voltage contribution in the Hall's measurement. The AC technique can provide an estimation of this contribution from the signal offset.
- The value of prescribed magnetic field also affects γ and ρ. From B_z= 2 [T] these properties become both magnetic and temperature functions.
- As verified with the last study, $FEAP$ simulations can predict laboratory experiments accurately. Although the results do not fit perfectly, the same evolution is observed. The perfect fit can not be as the experiment are affected by the environmental conditions and the devices' calibration of the room.

5.1 Future works

During the completion of this final degree project, new avenues of research on the characterization of the thermoelectric material were developed. Among all the ideas, the following stand out:

- Analysis of the stresses experienced by the material under magnetic field and the influence of these stresses on the measured properties.
- Analysis of 3D thermoelectric materials and reformulation of the existing methods of properties' characterization.
- Study of the radiation or convection influences on the thermoelectric properties.
- Study of the thermoelectric performance in multilayer thin films.
- Study of the techniques of measurement for Righi-Leduc and Ettinghausen-Nernst coefficients and their dependence on temperature and on magnetic field.
- Study of enhanced thermoelectric properties of nanocomposite materials (bulk material embedded with nanoparticles).
- Research and simulation of techniques for properties' measurement in nanowires.

5.2 Budget

The following breakdown details the total cost for carrying out this work:

Amount	Task	Cost/unit	Total cost
360	Total Engineer Hours	40.00 €	14400.00 €
60	Theoretical training		
30	*FEAP* Training		
30	FEM Models in *FEAP*		
20	Analytical models in *Matlab*©		
20	Analytical models in *Mathematica*©		
20	Post-processing results in *Illustrator*©		
40	Results analysis		
60	Validations and errors analysis		
80	Report reduction		
200	Total Server hours	5.00 €	1000.00 €
100	*FEAP* results		
100	Analytical results		
1	*FEAP* License		1500.00 €
1	*Matlab*© Annual Academic License		35.00 €
1	*Mathematica*© Annual Academic License		199.00 €
1	*Illustrator*© Annual Academic License		290.00 €
	Total budget (excluding VAT)		17334.00 €
	VAT (21%)		3640.14 €
	Total budget		**20974.14** €

The budget amounted to TWENTY THOUSAND NINE HUNDRER SEVENTY-FOUR €.

Bibliography

[1] G. Neeli, D. K. Behara, M. K. Kumar, *State of the Art Review on Thermoelectric Materials*, Department of Chemical Engineering, Anantapuramu, India, International Journal of Science and Research, 2013.

[2] D. Gorinevsky, *Design of Integrated SHM System for Commercial Aircraft Applications*, Honeywell Laboratories Stanford University, 5th International Workshop on Structural Health Monitoring, Stanford, CA, 2005.

[3] R. R. Furlong, E. J. Wahlquist, *U. S Space Missions Using Radioisotope Power Systems*, USA Nuclear News, 1999, pp. 26-34.

[4] J. W. Fairbanks, *Automotive Thermoelectric Generators and Air Conditioner/Heaters*, Turin Polytechnic University in Tashkent, Uzbekistan, ENVIRONMENTAL SCIENCES, 2012

[5] C. Gould, N. Shammas, *A Review of Thermoelectric MEMS Devices for Micro-power Generation, Heating and Cooling Applications, Micro Electronic and Mechanical Systems*, Kenichi Takahata, Micro Electronic and Mechanical Systems, 2009, Chapter 2, pp. 15-23.

[6] D. Samson, T. Otterpohl, M. Kluge, U. Schmid, T. Becker, *Aircraft-Specific Thermoelectric Generator Module*, Journal of ELECTRONIC MATERIALS 39, 2010, pp. 2092–2095.

[7] F. Stabler, *Automotive applications of high efficiency thermoelectrics*, DARPA/ONR Program Review and DOE High Efficiency Thermoelectric Workshop, San Diego, CA, USA, 2002.

[8] J. Vázquez, M. A. Sanz-Bobi, R. Palacios, A. Arenas, *A State of the art of thermoelectric generators based on heat recovered from the exhaust gases of automobiles*, 7th European Workshop on Thermoelectrics, Pamplona, Spain, 2002.

[9] R. Cataldo, G. Bennett, *U. S. Space Radioisotope Power Systems and Applications: Past, Present and Future*, NASA Glenn Research Center, Metaspace Enterprises, USA Nuclear News, 2011, Chapter 4, pp. 473-494.

[10] J. M. Dilhac, R. Monthéard, M. Bafleur, V. Boitier, N. Nolhier, P. Durand-Estèbe, P. Tounsi, *Implementation of Thermoelectric Generators in Airliners for Powering, Battery-free Wireless Sensor Networks*, Institute of Electrical and Electronics Engineers, Journal of Electronic Materials, 2014.

[11] T. Liu, *Recent Progress in Nanostructured Thermoelectric Materials*, Zernike Institute for Advanced Materials, University of Groningen, The Netherlands.

[12] I. M. Abdel-Motaleb, S. M. Qadri, *Thermoelectric Devices: Principles and Future Trends*, Department of Electrical Engineering, Northern Illinois University, DeKalb, US, arXiv preprint arXiv:1704.07742, 2017.

[13] F. Fitriani, R. Ovik, L. Bui, M. Barma, M. Riaz, M. Sabri, S. M. Said, R. Saidur, *A review on nanostructures of high-temperature thermoelectric materials for waste heat recovery*, Department of Mechanical Engineering, University of Malaya, Malaysia, Renewable and Sustainable Energy Reviews Vol. 64, 2016, pp. 635-659.

[14] J. Mao, Z. Liu, Z. Ren, *Size effect in thermoelectric materials*, Department of Physics and Texas Center for Superconductivity, University of Houston, Houston, TX, USA, npj Quantum Materials Vol. 1, 2016.

[15] C. Zhiwei, Z. Xinyue, P. Yanzhong, *Manipulation of Phonon Transport in Thermoelectrics*, Interdisciplinary Materials Research Center School of Materials Science and Engineering, Tongji University, Shanghai, China, Advanced Materials Vol. 30, 2018.

[16] R. L. Taylor, *FEAP - - A Finite Element Analysis Program, Version 8.4 User Manual*, Department of Civil and Environmental Engineering, University of California at Berkeley, California.

[17] Y. Feng, A. Elquist, Y. Zhang, K. Gao, I. Ferguson, A. Tzempelikos, N. Lu, *Temperature dependent thermoelectric properties of cuprous delafossite oxides*, Composites Part B: Engineering Vol. 156, 2018.

[18] D. M. Rowe, *CRC handbook of thermoelectrics*, CRC Press, UK, 2018.

[19] M. J. Latif, *Heat conduction*, Third Edition, New York, Springer, 2000, pp. 24-118.

[20] P. Kumar, D. V. Maheswar Repaka, K. Hippalgaonkar, *Lithography-free resistance thermometry based technique to accurately measure Seebeck coefficient and electrical conductivity for organic and inorganic thin films*, Institute of Materials Research and Engineering, Agency for Science Technology and Research, Singapore, Review of Scientific Instruments 88, 125112 (2017).

[21] C. Ruttanapun, A. Wichainchai, W. Prachamon, A. Yangthaisong, A. Charoenphakdee, T. Seetawan, *Thermoelectric properties of $Cu_{1x}Pt_xFeO_2$ delafossite-type transition oxide*, Journal of Alloys and Compounds, Vol. 509, 2011.

[22] J. L. Pérez-Aparicio, R. Palma, R. L. Taylor, *Multiphysics and Thermodynamic Formulations for Equilibrium and Non-equilibrium Interactions: Non-linear Finite Elements Applied to Multi-coupled Active Materials*, Archives of Computational Methods in Engineering Vol. 23, 2016, pp. 535–583.

[23] L. Palomo Ramón, *Estudio mediante elementos finitos de materiales termoeléctricos construidos por sublimación inversa*, Universitat Politècnica de València, Escola Tècnica Superior d'Enginyeria del Disseny, 2020.

[24] S. Romero, F. J. Moreno, I. M. Rodríguez, *Introducción a las ecuaciones diferenciales en derivadas parciales*, Universidad de Huelva, Escuela Politécnica Superior de La Rábida, Second Edition, CONSULCOM, June 2019.

[25] H. Okumura, S. Yamaguchi, H. Nakamura, K. Ikeda, K. Sawada, *Numerical Computation of Thermoelectric and Thermomagnetic Effects*, Proceedings ICT 98. XVII International Conference Thermoelectrics, 1998, pp. 89-92.

[26] B. I. Bleaney, B. Bleaney, *Electricity and magnetism*, Oxford University Press, Second Edition, 1965, pp. 126-151.

[27] D. B. Pengra, J. Stoltenberg, R. van Dyck, O. Vilches, *Hall effect*, Journal of Modern Physics, Vol. 8 No. 4, March 15, 2017.

[28] J. Lindemuth, *Hall effect measurement handbook. A fundamental tool for semiconductor material characterization*, Lake Shore CRYOTRONICS Wasterville, 2020.

[29] *F76-08. Standard test methods for measuring resistivity and Hall coefficient and determining Hall mobility in single-crystal semiconductors*, ASTM INTERNACIONAL, Annual Book of ASTM Standards, Am. Soc. Test. Mat., Philadelphia, 1991.

[30] *Lake Shore 7500/9500 Series Hall system user's manual. Appendix A Hall effect measurements*, Lake Shore CRYOTRONICS.

[31] C. Kasl, M. J. R. Hoch, *Effects of sample thickness on the Van der Pauw technique for resistivity measurements*, University of the Witwatersrand, South Africa, Review of Scientific Instruments 76, 2005.

[32] R. Daou, R. Fresard, S. Hebert, A. Maignau, *Impact of short-range order on transport properties of the two-dimensional metal* $PdCrO_2$, Laboratoire CRISMAT, American Physical Society, Phys. Rev. B Vol. 92, 2015.

[33] S. Countryman, *Voltage offset due to transverse misalignment of probes in sample*, Columbia University Physics Lecture Demonstrations.

[34] M. I. Dyakonov, *Spin Hall Effect* Université Montpellier II, CNRS, 34095 Montpellier, France, Proceedings of SPIE - The International Society for Optical Engineering Vol. 7036, 2012.

[35] S. Iwanaga, E. S. Toberer, A. LaaLonde, G. F. Snyder, *A high temperature apparatus for measurement of the Seebeck coefficient* Materials Science, California Institute of Technology, Review of Scientific Instruments 82, 2011.

[36] E. Dobrovinskaya, L. Lytvynov, V. Pishchik, *Properties of Sapphire*, Springer Science and Business Media, 1970, pp. 55-176.

[37] G. Cook , M. P. Van der Meer, *The thermal conductivity and electrical resistivity of gold from 80 to 340 K*, Division of Physics, Natiorzal Research Council of Canada, Ottawa, Canada, Canadian Journal of Physics, 1970, pp. 254-263.

[38] K. Hippalgaonkar, Y. Wing, Y. Ye, D. Y. Qiu, H. Zhu, Y. Wang, J. Moore, S. G. Louie, X. Zhang, *High thermoelectric power factor in two-dimensional crystals of* MoS_2, Phys. Rev. B 95, 2017.

[39] A. D. Avery, S. J. Mason, D. Bassett, D. Wesenberg, B. L. Zink, *Phys. Rev. B 92*, 2015.

[40] F. J. Blatt, P. A. Schroeder, C. L. Foiles, D. Greig, *Thermoelectric Power of Metals* Plenium Press, New York, Materials Science, 1976.

[41] PatterningMetalSurfacesUsingShadowMasks(platypustech.com)

[42] https://es.mathworks.com/help/dsp/ref/dsp.dcblocker-system-object.html

[43] https://www.allaboutcircuits.com/technical-articles/an-introduction-to-the-discrete-fourier-transform/

[44] https://dsp.stackexchange.com/questions/12972/discrete-fourier-transform-what-is-the-dc-term-really

[45] https://voyager.jpl.nasa.gov/mission/spacecraft/instruments/rtg/

[46] https://www.nationalgeographic.com.es/mundo-ng/empresas-europeas-mas-contaminantes-2018_14110

[47] https://space.skyrocket.de/doc_sdat/transit-4.htm

[48] https://ianwhittakeronline.com/wp-content/uploads/2016/11/mems-hysitron-inc.jpg

[49] https://mars.nasa.gov/mars2020/

[50] https://inl.gov/wp-content/uploads/2014/10/ AtomicPowerInSpaceII-AHistory_2015_chapters1-2.pdf

[51] https://reference.wolfram.com/language/tutorial/DSolveOverview.html

[52] https://www.researchgate.net/post/What_is_the_difference_in_Finite_difference_method_Finite_volume_method_and_Finite_element_method

[53] https://www.nist.gov/image/bighallbar970png